Engineering Photocatalysts towards High-Performance Solar Hydrogen Production

Jingrun Ran

A thesis submitted for the degree of Doctor of Philosophy

School of Chemical Engineering
Faculty of Engineering, Computer and Mathematic Sciences
The University of Adelaide

September 2016

Table of Contents

Declaration

This work contains no material which has been accepted for the award of any other degree or diploma in any university or other tertiary institution to Jingrun Ran and, to the best of my knowledge and belief, contains no material previously published or written by another person, except where due reference has been made in the text. In addition, I certify that no part of this work will, in the future, be used in a submission in my name for any other degree or diploma in any university or other tertiary institution without the prior approval of the university of Adelaide and where applicable, any partner institution responsible for the joint award of this degree.

I give consent to this copy of my thesis, when deposited in the University Library, being made available for loan and photocopying, subject to the provisions of the Copyright Act 1968.

The author acknowledges that copyright of published works contained within this thesis resides with the copyright holders of those works.

I also give permission for the digital version of my thesis to be made available on the web, via the University's digital research repository, the Library Search and also through we search engines, unless permission has been granted by the University to restrict access for a period of time.

Name of Candidate: Jingrun Ran

Signature:

Date: 14/09/2016

Acknowledgments

First and foremost, I would like to express my sincere gratitude to my principle supervisor, Prof. Shi Zhang Qiao, for his invaluable guidance, strong support and encouragement during my PhD study. His suggestions not only motivate me in scientific research, but also enlighten me in life. Also, I am grateful to my co-supervisor Dr. Philip Kwong who instructs me in research.

Special thanks to Dr. Jun Zhang in Wuhan University of Technology for helping with various advanced characterization techniques. I am grateful to my colleague Dr. Tian-Yi Ma who discussed with me about my research. I also appreciate the help from Mr. Guoping Gao for conducting theoretical simulations to support my research.

I want to extend my appreciation to all the group members from Prof. Qiao's group in the University of Adelaide for their technological assistance and helpful discussion. They are Dr. Yao Zheng, Dr. Ruifeng Zhou, Dr. Sheng Chen, Dr. Lei Zhang, Dr. Xin Du, Dr. Yan Jiao, Dr. Ping Chen, Mr. Dongdong Zhu, Mr. Jinlong Liu, Miss Bita Bayatsarmadi and Miss Lei Liu.

Many thanks to all the staff members from the school of Chemical Engineering and Adelaide microscopy for their individual help and support.

I would also like to acknowledge the China Scholarship Council (CSC) and the University of Adelaide, which offered me the scholarship to pursue my PhD degree and live in Adelaide. Also, many thanks to the Australian Research Council Discovery project, which has financially supported my PhD research.

Finally, I want to express my great gratitude to my parents and wife, for their endless love and encouragement in my life.

Abstract

The production of chemical fuels by solar energy conversion is regarded as one of the major strategies to address the aggravating energy and environmental problems. Particularly, photocatalytic water splitting has attracted tremendous attention since it represents a clean, cost-effective and environmental-benign technique for solar hydrogen (H_2) production. The core challenge of this promising technology lies in the development of low-cost and environmentally-friendly photocatalyst/co-catalyst systems with high activity and stability. However, to date most of the photocatalysts and co-catalysts are based on transitional metals and noble metals (*e.g.* Pt), respectively, which are neither economic nor environmental-benign. Therefore, the development of metal-free photocatalysts and noble-metal-free co-catalysts are highly desirable. This thesis aims to design and fabricate different highly-active and stable metal-free photocatalyst and noble-metal-free co-catalyst to achieve high-efficient solar H_2 production.

The first part of this thesis focuses on developing high-performance and low-priced metal-free graphitic carbon nitride (g-C_3N_4) photocatalysts as an alternative to current metal-based photocatalysts. Porous P-doped g-C_3N_4 nanosheets (PCN-S) were firstly synthesized by combining P doping and thermal exfoliation strategies. The P-doped conjugated system and novel macroporous nanosheet morphology synergistically contribute to the outstanding photocatalytic H_2-production activity of PCN-S under visible-light irradiation. Furthermore, the P doping was found to create empty midgap states in PCN-S, which greatly extend the light-responsive region; whilst the novel macroporous structure benefits the mass-transfer process and enhances light harvesting. This work not only demonstrates an easy, eco-friendly and scalable strategy to synthesize highly efficient porous g-C_3N_4 nanosheet photocatalysts, but also paves a new avenue for the rational design and synthesis of advanced photocatalysts by harnessing the strong synergistic effects through simultaneously tuning and optimizing the electronic, crystallographic, surface and textural structures.

The second part of this thesis is to design and synthesize a series of earth-abundant co-catalysts for replacing rare and expensive Pt. Ni-based co-catalysts, *e.g.* NiS, metallic Ni and $Ni(OH)_2$, were deposited on $Zn_xCd_{1-x}S$ nano-particles (NPs) to greatly enhance their visible-light photocatalytic H_2-production activity. Particularly, $Ni(OH)_2$ loaded $Zn_xCd_{1-x}S$ shows superior photocatalytic performance to Pt-loaded $Zn_xCd_{1-x}S$ under the identical conditions. This outstanding performance originates from the notable synergetic effect between $Ni(OH)_2$ and metallic Ni formed *in situ* during the photocatalytic reaction. We also for the first time designed and fabricated a novel MXene material, Ti_3C_2 NPs, as a highly-efficient co-catalysts. Ti_3C_2 NPs were rationally incorporated with

CdS by a hydrothermal technique to achieve a super high visible-light photocatalytic H_2-production performance. This remarkable performance results from the optimized Fermi level, efficient hydrogen evolution capacity and novel active sites on Ti_3C_2 NPs. Our work demonstrates the huge potential of earth-abundant MXene family materials to fabricate numerous high-performance and low-cost photocatalysts/photoelectrodes.

The third part of this thesis aims to reveal the superior electron extracting capacity of Ti_3C_2 NPs on $Zn_xCd_{1-x}S$ towards visible-light induced H_2 production. Through combining the experimental techniques and theoretical computations, we have explored the critical role of Ti_3C_2 NPs loaded on the surface of $Zn_xCd_{1-x}S$, which greatly promotes the vectorial electron transfer from $Zn_xCd_{1-x}S$ to Ti_3C_2 NPs. The as-synthesized Ti_3C_2 modified $Zn_xCd_{1-x}S$ composite exhibits the highest photocatalytic H_2-production activity of 7196 μmol h^{-1} g^{-1} at the optimal loading content of 4 wt%. This work demonstrates the possibility of using Ti_3C_2 to replace expensive Pt in photocatalytic H_2 production.

Chapter 1: Introduction

1.1 Significance of the project

Semiconductor photocatalysis has attracted tremendous attention as a potential solution to the global energy shortage and for counteracting environmental degradation.[1-3] The production of H_2 via photocatalytic water splitting is even considered as the "holy grail" in modern science.[4] In the past 40 years, numerous transitional-metal based photocatalysts (*e.g.* oxides, (oxy)sulphides and (oxy)nitrides) and noble-metal co-catalysts (*e.g.* Pt, Ru and Pd) have been developed for photocatalytic H_2 production.[3,5,6] Unfortunately, none of these photocatalysts/co-catalyst systems can achieve H_2 production with sufficiently high activity and stability; whilst most of these systems are expensive and harmful to the environment. For these reasons, it is significant but challenging to develop high-efficiency and robust photocatalysts and co-catalysts, based on meta-free and noble-metal-free elements, respectively.

1.2 Research objectives

The major goals of this thesis are to gain insights into the reaction mechanism of the photocatalyst/co-catalyst systems towards H_2 production from water splitting, and thus synthesize inexpensive, efficient and durable metal-free photocatalysts and noble-metal-free co-catalysts. Specifically, the targets of this thesis are:

- **Exploring** the heteroatom-doping effect of g-C_3N_4 on photocatalytic H_2-production performance, and developing simple and effective strategy to fabricate heteroatom-doped g-C_3N_4 with homogeneous dopant distribution.
- **Revealing** the mechanism of photocatalytic H_2 production enhanced by simultaneously tuning and optimizing the electronic, crystallographic, surface and textural structures of g-C_3N_4, through combining P doping and thermal exfoliation strategies.
- **Understanding** the species dependence of H_2 production activity over Ni-based co-catalysts loaded photocatalyst systems, and thus selecting the most efficient Ni-based co-catalyst for a specific photocatalyst system.
- **Developing** a brand new family of highly-active and inexpensive MXene co-catalysts towards improving the photocatalytic activity on a series of metal sulphides photocatalysts, guided by density function theory (DFT) calculations.

- **Combining** advanced characterization techniques and modern calculations tools to gain underlying mechanism of novel Ti_3C_2 MXene co-catalysts loaded on CdS sub-microspheres towards solar H_2 production.
- **Investigating** the strong electronic coupling between Ti_3C_2 MXene and $Zn_xCd_{1-x}S$ to explain the pronounced performance enhancement over Ti_3C_2 MXene loaded $Zn_xCd_{1-x}S$.

1.3 Thesis outline

This thesis is the outcomes of my PhD research presented in the form of journal publications. The chapters in this thesis are presented in the following sequence:

- ***Chapter 1*** introduces the significance of the thesis and outlines the objectives and key contributions to the area of research.
- ***Chapter 2*** reviews the literatures covering all the developed earth-abundant co-catalyst applied in photocatalytic water splitting to date.
- ***Chapter 3*** develops metal-free porous P-doped graphitic C_3N_4 nanosheets for high-efficiency and long-term photocatalytic H_2 production under visible-light illumination.
- ***Chapter 4*** investigates the insightful photocatalytic mechanism of $Zn_xCd_{1-x}S$ loaded with different Ni-based co-catalysts.
- ***Chapter 5*** designs and synthesizes a novel MXene material, Ti_3C_2 NPs, as a highly-efficient earth-abundant co-catalyst to tremendously boost the photocatalytic performance of metal sulphides photo-absorbers.
- ***Chapter 6*** devotes to revealing the superior electron-extracting capacity of Ti_3C_2 NPs on $Zn_xCd_{1-x}S$ for highly-active photocatalytic H_2 production.
- ***Chapter 7*** presents conclusion and perspectives for future work on preparation of metal-free photocatalysts and earth-abundant co-catalysts, their applications and mechanism of photocatalytic H_2 production.

1.4 References

1 H. Tong, S. Ouyang, Y. Bi, N. Umezawa, M. Oshikiri, J. Ye, ***Adv. Mater.*** 2012, **24**, 229-251.

2 X. Li, J. Yu, M. Jaroniec, ***Chem. Soc. Rev.*** 2016, **45**, 2603-2636.

3 X. Chen, S. Shen, L. Guo, S. S. Mao, ***Chem. Rev.*** 2010, **110**, 6503-6570.

4 M. Bowker, ***Green Chem.*** 2011, **13**, 2235-2246.

5 J. Ran, J. Zhang, J. Yu, M. Jaroniec, S. Z. Qiao, ***Chem. Soc. Rev.*** 2014, **43**, 7787-7812.

6 A. Kudo, Y. Misekia, ***Chem. Soc. Rev.*** 2009, **38**, 253-278.

Chapter 2: Literature review

2.1 Introduction

This chapter gives a comprehensive appraisal of all the co-catalysts based on earth-abundant elements towards photocatalytic H_2/O_2 production and overall photocatalytic water splitting. Particularly, the detailed photocatalytic mechanism of co-catalyst/semiconductor photocatalyst is summarized. Furthermore, this chapter also provides remarks on some challenges and perspectives in this emerging area of research.

2.2 Earth-abundant Cocatalysts for Semiconductor-based Photocatalytic Water Splitting

This section is included as it appears as a journal paper published by **Jingrun Ran**, Jun Zhang, Jiaguo Yu, Mietek Jaroniec and Shi Zhang Qiao, Earth-abundant Cocatalysts for Semiconductor-based Photocatalytic Water Splitting, ***Chemical Society Reviews***, 2014, 43, 7787-7812.

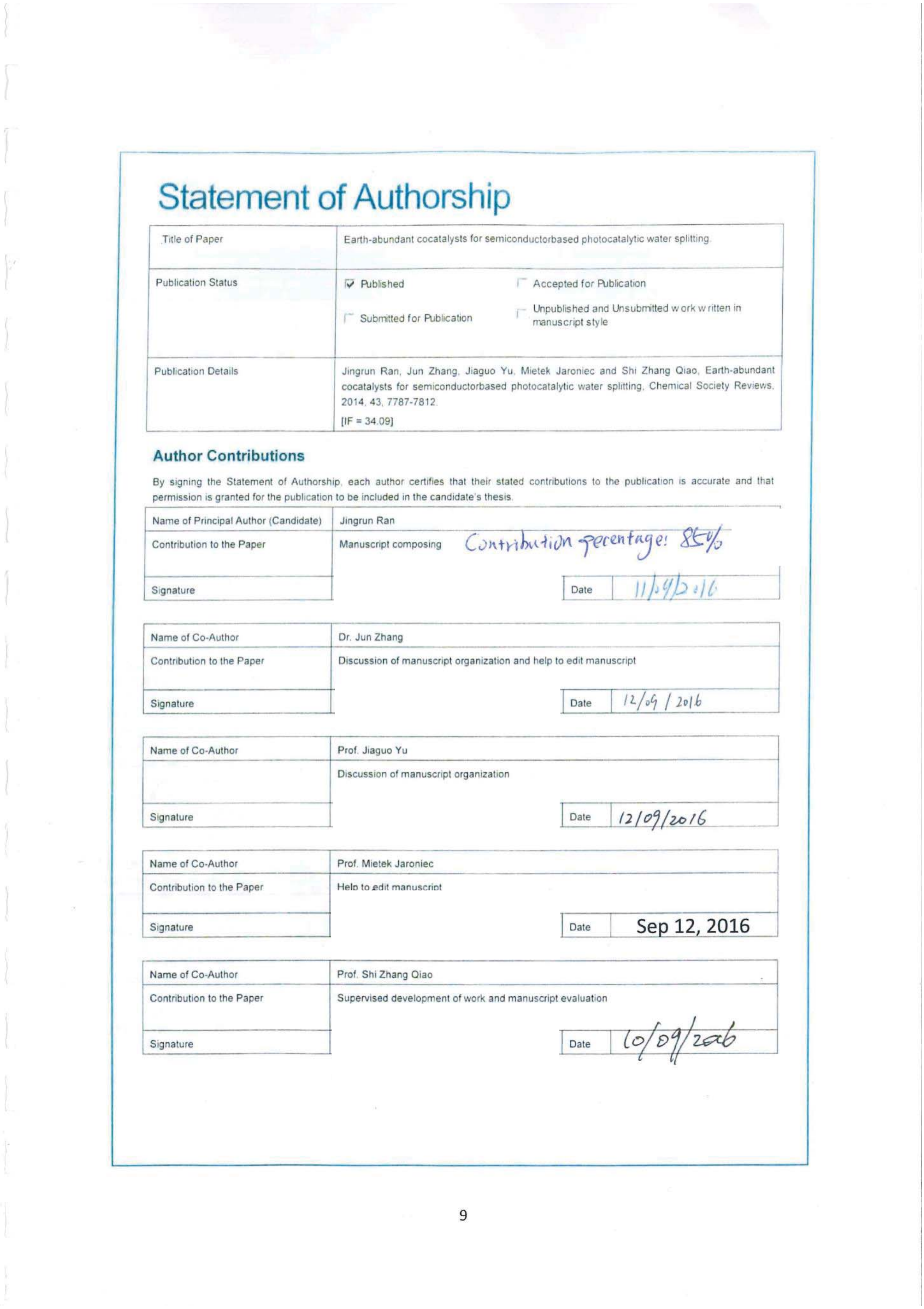

Statement of Authorship

Title of Paper	Earth-abundant cocatalysts for semiconductorbased photocatalytic water splitting.
Publication Status	☑ Published ☐ Accepted for Publication ☐ Submitted for Publication ☐ Unpublished and Unsubmitted work written in manuscript style
Publication Details	Jingrun Ran, Jun Zhang, Jiaguo Yu, Mietek Jaroniec and Shi Zhang Qiao, Earth-abundant cocatalysts for semiconductorbased photocatalytic water splitting, Chemical Society Reviews, 2014, 43, 7787-7812. [IF = 34.09]

Author Contributions

By signing the Statement of Authorship, each author certifies that their stated contributions to the publication is accurate and that permission is granted for the publication to be included in the candidate's thesis.

Name of Principal Author (Candidate)	Jingrun Ran
Contribution to the Paper	Manuscript composing Contribution percentage: 85%
Signature	Date 11/09/2016

Name of Co-Author	Dr. Jun Zhang
Contribution to the Paper	Discussion of manuscript organization and help to edit manuscript
Signature	Date 12/09/2016

Name of Co-Author	Prof. Jiaguo Yu
	Discussion of manuscript organization
Signature	Date 12/09/2016

Name of Co-Author	Prof. Mietek Jaroniec
Contribution to the Paper	Help to edit manuscript
Signature	Date Sep 12, 2016

Name of Co-Author	Prof. Shi Zhang Qiao
Contribution to the Paper	Supervised development of work and manuscript evaluation
Signature	Date 10/09/2016

9

Ran, J., Zhang, J., Yu, J., Jaroniec, M. & Qiao, S.Z. (2014). Earth-abundant cocatalysts for semiconductor-based photocatalytic water splitting, *Chemical Society Reviews, 43*(22), 7787-7812.

NOTE:
This publication is included on pages 10 - 35 in the print copy of the thesis held in the University of Adelaide Library.

It is also available online to authorised users at:

http://dx.doi.org/10.1039/c3cs60425j

Chapter 3: Porous P-doped Graphitic Carbon Nitride Nanosheets for Synergistically Enhanced Visible-Light Photocatalytic H_2 Production

3.1 Introduction and Significance

The production of clean and carbon-free hydrogen energy from inexhaustible solar energy through photocatalytic water splitting is a 'dream technology' to address the worldwide energy shortage, environmental contamination and the greenhouse effect. The core challenge of this advanced technology lies in the development of low-cost and environmentally benign photocatalysts with sufficiently high activity and stability to produce hydrogen at a cost comparable to the conventional fossil fuels. In this chapter, we have synthesized a novel porous P-doped graphitic carbon nitride (g-C_3N_4) nanosheets (PCN-S) photocatalyst by a combination of P doping and thermal exfoliation strategy. The P doping and macroporous nansheets morphology synergistically contribute to the visible-light photocatalytic H_2-production activity. The highlights of this work include:

- The PCN-S photocatalyst was for the first time fabricated by a novel P doping and thermal exfoliation strategy, which is a facile, eco-friendly and scalable method for acquiring porous and ultrathin nanosheets structures, without using any templates or organic/acid chemicals.
- We firstly reports a unique macroporous nanosheets architecture of PCN-S, different from the previously reported bulk P-doped g-C_3N_4 or non-porous g-C_3N_4 nanosheets. A uniform and substantial dispersion of P element in g-C_3N_4 nanosheets was firstly achieved by using a new P precurosr, 2-aminoethylphosphonic acid, to form a homogeneous and strong coupling with melamine.
- The P-doped g-C_3N_4 nanosheets exhibit the high visible-light photocatalytic H_2-production activity of 1596 μmol h^{-1} g^{-1} and apparent quantum efficiency (QE) of 3.56% at 420 nm, representing one of the most highly-active g-C_3N_4 nanosheets photocatalysts.
- The macroporous nanosheets structure renders PCN-S a large surface area (122.6 m^2 g^{-1}), short charge-to-surface diffusion distance (5-8 nm), efficient mass transfer and enhanced light harvesting.
- P doping induces the formation of midgap states at -0.16 V *vs.* SHE, as firstly confirmed by density functional theory (DFT**)** and experimental studies, which extends the light absorption region to 557 nm and greatly contributes to photocatalytic H_2 production. Besides, the midgaps states increase charge mobility and serve as separation centers for photo-generated electron-hole pairs.

3.2 Porous P-doped Graphitic Carbon Nitride Nanosheets for Synergistically Enhanced Visible-Light Photocatalytic H_2 Production

This chapter is included as it appears as a journal paper published by **Jingrun Ran**, Tian Yi Ma, Guoping Gao, Xi-Wen Du and Shi Zhang Qiao, Porous P-doped graphitic carbon nitride nanosheets for synergistically enhanced visible-light photocatalytic H_2 production, ***Energy and Environmental Science***, 2015, 8, 3708-3717.

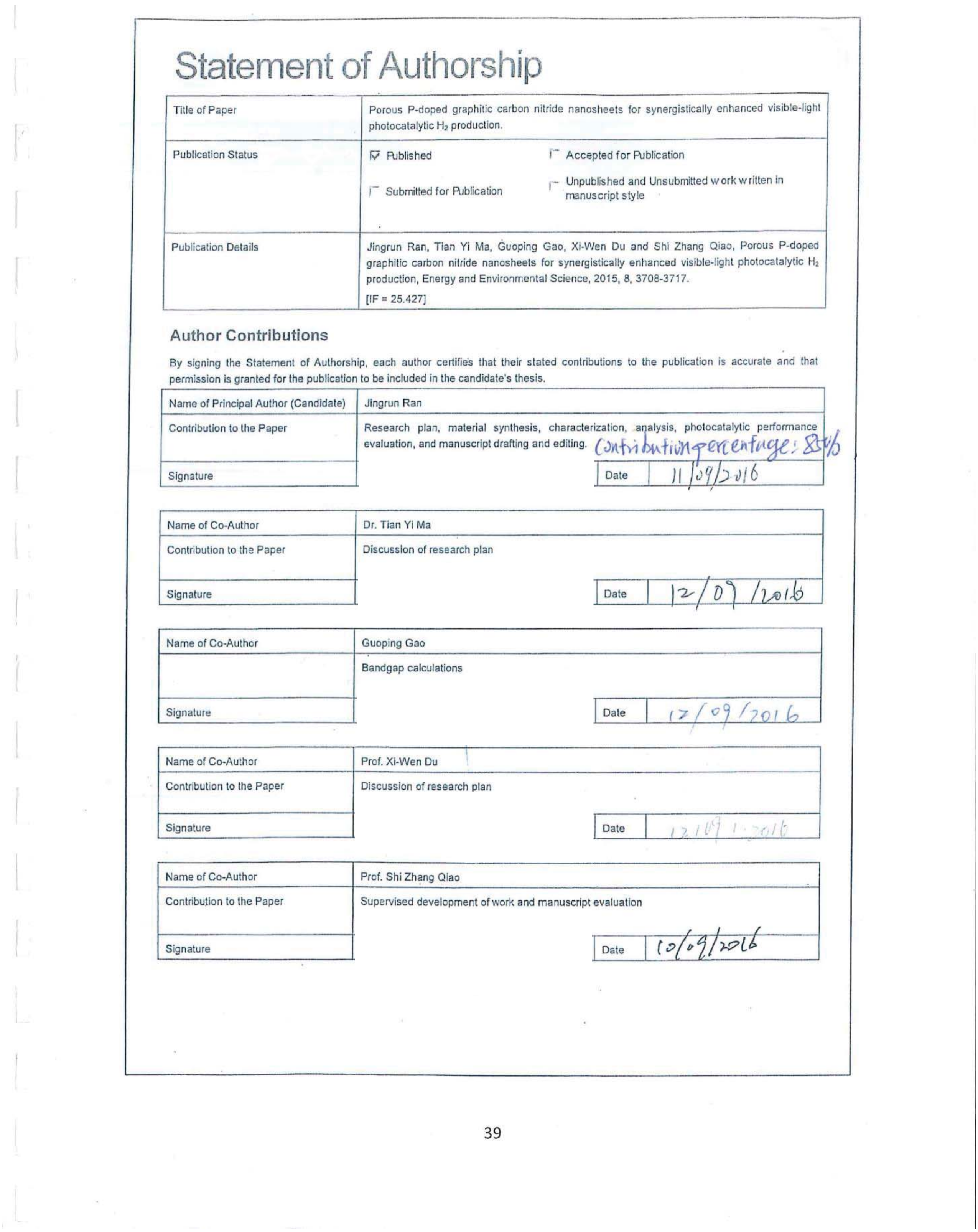

Statement of Authorship

Title of Paper	Porous P-doped graphitic carbon nitride nanosheets for synergistically enhanced visible-light photocatalytic H_2 production.
Publication Status	☑ Published ☐ Accepted for Publication ☐ Submitted for Publication ☐ Unpublished and Unsubmitted work written in manuscript style
Publication Details	Jingrun Ran, Tian Yi Ma, Guoping Gao, Xi-Wen Du and Shi Zhang Qiao, Porous P-doped graphitic carbon nitride nanosheets for synergistically enhanced visible-light photocatalytic H_2 production, Energy and Environmental Science, 2015, 8, 3708-3717. [IF = 25.427]

Author Contributions

By signing the Statement of Authorship, each author certifies that their stated contributions to the publication is accurate and that permission is granted for the publication to be included in the candidate's thesis.

Name of Principal Author (Candidate)	Jingrun Ran		
Contribution to the Paper	Research plan, material synthesis, characterization, analysis, photocatalytic performance evaluation, and manuscript drafting and editing. Contribution percentage: 85%		
Signature		Date	11/09/2016

Name of Co-Author	Dr. Tian Yi Ma		
Contribution to the Paper	Discussion of research plan		
Signature		Date	12/09/2016

Name of Co-Author	Guoping Gao		
	Bandgap calculations		
Signature		Date	12/09/2016

Name of Co-Author	Prof. Xi-Wen Du		
Contribution to the Paper	Discussion of research plan		
Signature		Date	12/09/2016

Name of Co-Author	Prof. Shi Zhang Qiao		
Contribution to the Paper	Supervised development of work and manuscript evaluation		
Signature		Date	10/09/2016

Ran, J., Ma, T.M., Gao, G., Du, X. & Qiao, S.Z. (2015). Porous P-doped graphitic carbon nitride nanosheets for synergistically enhanced visible-light photocatalytic H_2 production.
Energy and Environmental Science, 8(12), 3708-3717 & Supporting Information

NOTE:
This publication is included on pages 40 - 67 in the print copy of the thesis held in the University of Adelaide Library.

It is also available online to authorised users at:

http://dx.doi.org/10.1039/c5ee02650d

Chapter 4: Enhanced Visible-Light Photocatalytic H_2 Production by $Zn_xCd_{1-x}S$ Modified with Earth-Abundant Nickel-Based Cocatalysts

4.1 Introduction and Significance

The design and synthesis of highly-active, inexpensive and robust photocatalysts for solar H_2 production is of great importance. In this chapter, we report the fabrication of highly-efficient and stable $Zn_{0.8}Cd_{0.2}S$-based photocatalysts by constructing hetero-junctions between $Zn_{0.8}Cd_{0.2}S$ and earth-abundant Ni species. Our work shows that the intrinsic electronic properties of NiS, Ni or NiO, which dictates the electron separation and transfer efficiency at the hetero-junction interface, determines their photocatalytic activity; while the highest photocatalytic activity of $Ni(OH)_2$ loaded $Zn_{0.8}Cd_{0.2}S$ results from the positive synergetic effect of the *in situ* formed $Ni/Ni(OH)_2$ composite. The highlights of this work include:

- We for the first time investigated the loading of various Ni species (NiS, Ni, or $Ni(OH)_2$) on the surface of $Zn_{0.8}Cd_{0.2}S$ to form hetero-junctions for photocatalytic H_2 production, which can act as a substitute for noble-metal Pt cocatalysts.
- Both high activity and stability could be achieved by loading Ni, NiS or $Ni(OH)_2$ cocatalyst on $Zn_{0.8}Cd_{0.2}S$, in which $Ni(OH)_2$ leads to a remarkable photocatalytic H_2-production rate of 7160 $\mu mol\ h^{-1}\ g^{-1}$, with a quantum efficiency of 29.5% at 420 nm, representing one of the most active metal sulfides photocatalyts reported to date.
- We found that the charge separation and transfer efficiency at the hetero-junction interface between $Zn_{0.8}Cd_{0.2}S$ and NiS, Ni or NiO, which is greatly influenced by the intrinsic electronic properties of loaded Ni species, plays the key role in determining the photocatalytic activity.
- The outstanding photocatalytic activity of $Ni(OH)_2$ loaded $Zn_{0.8}Cd_{0.2}S$ is induced by the strong synergetic effect between $Ni(OH)_2$ and *in situ* formed metallic Ni during the photocatalytic reaction. $Ni(OH)_2$ could promote the dissociation of H_2O molecules and the production of protons, which are adsorbed on metallic Ni and reduced to form H_2 molecules.

4.2 Enhanced Visible-Light Photocatalytic H_2 Production by $Zn_xCd_{1-x}S$ Modified with Earth-Abundant Nickel-Based Cocatalysts

This chapter is included as it appears as a journal paper published by **Jingrun Ran**, Jun Zhang, Jiaguo Yu and Shi Zhang Qiao, Enhanced Visible-Light Photocatalytic H_2 Production by $Zn_xCd_{1-x}S$ Modified with Earth-Abundant Nickel-Based Cocatalysts, ***ChemSusChem***, 2014, 7, 3426-3434.

Statement of Authorship

Title of Paper	Enhanced visible-light photocatalytic H_2 production by $Zn_xCd_{1-x}S$ modified with earth-abundant nickel-based cocatalysts.
Publication Status	☑ Published ☐ Accepted for Publication ☐ Submitted for Publication ☐ Unpublished and Unsubmitted work written in manuscript style
Publication Details	Jingrun Ran, Jun Zhang, Jiaguo Yu and Shi Zhang Qiao, Enhanced visible-light photocatalytic H_2 production by $Zn_xCd_{1-x}S$ modified with earth-abundant nickel-based cocatalysts, ChemSusChem, 2014, 7, 3426-3434. [IF = 7.116]

Author Contributions

By signing the Statement of Authorship, each author certifies that their stated contributions to the publication is accurate and that permission is granted for the publication to be included in the candidate's thesis.

Name of Principal Author (Candidate)	Jingrun Ran		
Contribution to the Paper	Research plan, material synthesis, characterization, analysis, photocatalytic performance evaluation, and manuscript drafting and editing. Contribution Percentage: 85%		
Signature		Date	11/09/2016

Name of Co-Author	Dr. Jun Zhang		
Contribution to the Paper	Discussion of research plan		
Signature		Date	12/09/2016

Name of Co-Author	Prof. Jiaguo Yu		
	Discussion of research plan		
Signature		Date	12/09/2016

Name of Co-Author	Prof. Shi Zhang Qiao		
Contribution to the Paper	Supervised development of work and manuscript evaluation		
Signature		Date	10/09/2016

Ran, J., Zhang, J., Yu, J. & Qiao, S.Z. (2014). Enhanced visible-light photocatalytic H_2 production by $Zn_xCd_{1-x}S$ modified with earth-abundant nickel-based cocatalysts. *ChemSusChem*, *7*(12), 3426-3434 & Supporting Information

NOTE:
This publication is included on pages 71 - 91 in the print copy of the thesis held in the University of Adelaide Library.

It is also available online to authorised users at:

http://dx.doi.org/10.1002/cssc.201402574

Chapter 5: Ti_3C_2 MXene Co-catalyst on Metal Sulfide Photo-Absorbers for Enhanced Visible-Light Photocatalytic Hydrogen Production

5.1 Introduction and Significance

Currently, the large-scale solar hydrogen production via photocatalytic water splitting demands highly-efficient, robust and low-cost co-catalysts as a substitute for expensive and scarce noble-metal Pt. In this chapter, we have developed a brand-new area of applying MXene materials (over 60 members) as co-catalysts with high-efficiency and low-cost to replace rare and expensive Pt in photocatalysis. The highlights in this work include:

- We for the first time employed DFT calculations to explore the possibility of an emerging MXene material, Ti_3C_2, as a highly-efficient co-catalyst. The comprehensive evaluation of Gibbs free energy for hydrogen adsorption, electronic band structure and Fermi level position indicates that Ti_3C_2 with -O terminations is a highly-promising co-catalyst promoting photocatalytic H_2 production.
- Guided by theoretical prediction, we utilized ultra-sonication cutting and hydrothermal integration strategies to acquire Ti_3C_2 NPs decorated with abundant -O terminations and couple them with CdS to synthesize a novel CdS/Ti_3C_2 cauliflower-structured sub-microspheres (SMS). The highly-fused CdS/Ti_3C_2 architecture ensures the efficient interfacial charge transfer between photocatalyst CdS and co-catalyst Ti_3C_2.
- The CdS/Ti_3C_2 cauliflower-structured SMS exhibits a super high visible-light photocatalytic H_2-production activity of 14342 μmol h^{-1} g^{-1} and a remarkable apparent quantum efficiency (QE) of 40.1% at 420 nm, representing one of the most highly-active noble-metal-free metal sulphides photocatalysts to date. Besides, the photocatalytic activity can be further enhanced to 18560 μmol h^{-1} g^{-1} by co-loading Ti_3C_2 and NiS on CdS, suggesting the huge potential of this novel Ti_3C_2 co-catalyst.
- Both experimental observations and theoretical calculations reveal that the outstanding photocatalytic activity is aroused by the distinguished properties of Ti_3C_2 NPs with massive -O terminations: i) very positive Fermi level (EF = 1.88 V vs. SHE at pH = 0); ii) excellent metallic conductivity; iii) near-zero Gibbs free energy for hydrogen adsorption (ΔG_{H*} = -0.00283 eV). Hence, Ti_3C_2 NPs can efficiently extract the photo-induced electrons from CdS, shuttle them to

the surface active sites, and catalyse hydrogen evolution. Therefore, a synergistically enhanced photocatalytic activity is achieved in CdS/Ti_3C_2 system.

- The newly-developed Ti_3C_2 NPs are proven to be a versatile and efficient co-catalyst on other photocatalysts, *e.g.* $Zn_xCd_{1-x}S$ and ZnS. These results imply the enormous potential developing the large family of MXene materials to fabricate numerous highly-active, low-cost and stable photocatalysts/photoelectrodes for solar fuel production.

5.2 Ti_3C_2 MXene Co-catalyst on Metal Sulfide Photo-Absorbers for Enhanced Visible-Light Photocatalytic Hydrogen Production

This chapter is included in this thesis as it appears as a journal paper authored by **Jingrun Ran**, Guoping Gao, Fa-Tang Li, Tian-Yi Ma, Aijun Du, and Shi-Zhang Qiao, Ti_3C_2 MXene Co-catalyst on Metal Sulfide Photo-Absorbers for Enhanced Visible-Light Photocatalytic Hydrogen Production, and accepted by ***Nature Communications*** on 11 November 2016.

Statement of Authorship

Title of Paper	Ti_3C_2 MXene co-catalyst on metal sulfide photo-absorbers for enhanced visible-light photocatalytic hydrogen production.
Publication Status	☐ Published [✓ Accepted for Publication] ☑ Submitted for Publication ☐ Unpublished and Unsubmitted work written in manuscript style
Publication Details	Jingrun Ran, Guoping Gao, Fa-Tang Li, Tian-Yi Ma, Aijun Du and Shi-Zhang Qiao, Ti_3C_2 MXene co-catalyst on metal sulfide photo-absorbers for enhanced visible-light photocatalytic hydrogen production. Nature Communications.

Author Contributions

By signing the Statement of Authorship, each author certifies that their stated contributions to the publication is accurate and that permission is granted for the publication to be included in the candidate's thesis.

Name of Principal Author (Candidate)	Jingrun Ran		
Contribution to the Paper	Research plan, material synthesis, characterization, analysis, photocatalytic performance evaluation, and manuscript drafting and editing. Contribution percentage 85%		
Signature		Date	11/09/2016

Name of Principal Author (Candidate)	Guoping Gao		
Contribution to the Paper	Theoretical calculation.		
Signature		Date	12/09/2016

Name of Co-Author	Prof. Fa-Tang Li		
Contribution to the Paper	Discussion of research plan		
Signature		Date	11/09/2016

Name of Co-Author	Dr. Tian-Yi Ma		
	Discussion of research plan		
Signature		Date	14/09/2016

Name of Co-Author	Prof. Aijun Du		
Contribution to the Paper	Discussion of research plan		
Signature		Date	13/09/2016

Name of Co-Author	Prof. Shi-Zhang Qiao

Contribution to the Paper	Supervised development of work, manuscript evaluation and editing.		
Signature		Date	10/09/16

Ti_3C_2 MXene co-catalyst on metal sulfide photo-absorbers for enhanced visible-light photocatalytic hydrogen production

Jingrun Ran[1†], Guoping Gao[2†], Fa-Tang Li[1,3], Tian-Yi Ma[1], Aijun Du[2], Shi-Zhang Qiao[1]*

[1] School of Chemical Engineering, The University of Adelaide, Adelaide, South Australia 5005, Australia

[2] School of Chemistry, Physics and Mechanical Engineering Faculty, Queensland University of Technology, Garden Point Campus, Brisbane, QLD 4001, Australia

[3] College of Science, Hebei University of Science and Technology, Shijiazhuang 050018, China

* Correspondence to: s.qiao@adelaide.edu.au

† These authors contributed equally to this work.

ABSTRACT:

Scalable and sustainable solar hydrogen production through photocatalytic water splitting requires highly-active and stable earth-abundant co-catalysts to replace expensive and rare Pt. Here we employ density functional theory calculations to direct atomic-level exploration, design and fabrication of a MXene material, Ti_3C_2 nanoparticles, as a highly-efficient co-catalyst. Ti_3C_2 nanoparticles are rationally integrated with cadmium sulfide via a hydrothermal strategy to induce a super high visible-light photocatalytic hydrogen production activity of 14342 μmol h^{-1} g^{-1} and an apparent quantum efficiency of 40.1% at 420 nm. This high performance arises from the favorable Fermi level position, electrical conductivity and hydrogen evolution capacity of Ti_3C_2 nanoparticles. Furthermore, Ti_3C_2 nanoparticles also serve as an efficient co-catalyst on ZnS or $Zn_xCd_{1-x}S$. This work demonstrates the potential of earth-abundant MXene family materials to construct numerous high-performance and low-cost photocatalysts/photoelectrodes.

The generation of hydrogen (H_2) from water using solar energy is regarded as a promising strategy for solving global energy problems[1,2,3]. Particularly, photocatalytic water splitting by utilizing semiconductor photocatalysts has demonstrated huge potential as a clean, low-cost and sustainable approach for solar H_2 production. However, despite tremendous achievement in this area during the past decades[1,4,5], it is still a great challenge to develop highly-efficient, cost-effective and robust photocatalysts driven by sunlight. In recent years, co-catalysts have shown great success in boosting both the activity and stability of photocatalysts[6-9]. Unfortunately, the high price and extreme scarcity of the most active H_2-evolution co-catalyst, Pt, restricts the commercialization of current photocatalysts. Therefore, seeking an inexpensive and highly-active co-catalyst to replace Pt is of paramount significance for achieving large-scale solar H_2 production in the future.

To date, although enormous progress has been made in developing earth-abundant co-catalysts, several major problems, arising from the intrinsic properties of current co-catalysts, still exist: i) lack of abundant surface functionalities to establish strong connection with photocatalysts, for fast interfacial charge transfer and long-term stability; ii) inefficient electron shuttling within co-catalysts due to their poor semiconducting/insulating conductivity[10] or destruction of π-conjugated system (*e.g.* graphene oxide)[11]; iii) undesirable Gibbs free energy for H_2 evolution; iv) insufficient contact with water molecules due to lack of hydrophilic functionalities; and v) instability and/or requirement of non-aqueous environment (*e.g.* hydrogenases and their mimics)[12,13]. Therefore, it is highly desirable to seek a brand-new family of materials as the next generation co-catalysts that can overcome these drawbacks.

MXene, a new family of over 60 two-dimensional (2D) metal carbides, nitrides or carbonitrides[14,15], has shown great potential as electrodes in (Li)-ion batteries[16] and supercapacitors[17]. Notably, their distinguished characteristics render them highly-promising for solving the above problems as: i) MXene possesses numerous hydrophilic functionalities (-OH and -O) on its surface, enabling it to easily construct strong connection with various semiconductors; ii) the excellent metallic conductivity of MXene assures efficient charge-carrier transfer; iii) the exposed terminal metal sites (*e.g.* Ti, Nb or V) on MXene might lead to much stronger redox reactivity than that of the carbon materials[18]; iv) the presence of numerous hydrophilic functionalities on MXene promotes its strong interaction with water molecules; and v) MXene can stably function in aqueous solutions. Considering the above outstanding properties of the MXene family, it is anticipated that MXene will be a promising material to be employed in photocatalysis. However, to the best of our knowledge, there is no report on exploring MXene as a co-catalyst for photocatalysis.

Herein, we utilize density functional theory (DFT) calculations to explore the potential of Ti_3C_2 MXene as a H_2 evolution co-catalyst. Based on theoretical studies, we report a rational design and synthesis of Ti_3C_2 nanoparticles (NPs) and merge them with a chosen photocatalyst, CdS, to successfully achieve a super high visible-light photocatalytic H_2-production activity. The origin of this high activity is studied by both experimental techniques and theoretical investigations. Moreover, the general function of Ti_3C_2 NPs as an active co-catalyst for other photocatalysts is also confirmed, illustrating the considerable potential of MXene family materials to replace rare and costly Pt in photocatalysis/photoelectrocatalysis.

Results

Theoretical exploration of Ti_3C_2 MXene as a co-catalyst. To explore the possibility of using Ti_3C_2 MXene as a highly-efficient and low-priced co-catalyst to promote H_2 production, we have conducted a series of theoretical investigations based on DFT calculations. A highly-active co-catalyst can not only rapidly extract photo-induced electrons from a photocatalyst to its surface, but also efficiently catalyze the H_2 evolution on its surface, by using those electrons[6]. Herein, we firstly focus on the H_2 evolution activity to evaluate whether Ti_3C_2 is an excellent candidate. Usually, the overall H_2 evolution reaction (HER) pathway can be summarized by a three-state diagram, composed of an initial state $H^+ + e^-$, an intermediate adsorbed H*, and a final product $\frac{1}{2}H_2$[19,20]. The Gibbs free energy of the intermediate state, $|\Delta G_{H*}|$, is regarded as a major indicator of the HER activity for various catalysts. The most desirable value for $|\Delta G_{H*}|$ should be zero[20]. For example, the highly-active and well-known HER catalyst, Pt, shows a near-zero value of $\Delta G_{H*} \approx -0.09$ eV[21,22]. Thus, we performed DFT studies to calculate ΔG_{H*} for atomic H adsorption on the surface of pure Ti_3C_2, F-terminated Ti_3C_2 and O-terminated Ti_3C_2, respectively. Their structural models are displayed in Supplementary Fig. 1, Supplementary Fig. 2 and Fig. 1a, respectively. Pure Ti_3C_2 exhibits a largely negative $\Delta G_{H*} = -0.927$ eV (Supplementary Fig. 3a), suggesting too strong chemical adsorption of H* on its surface. Meanwhile, a largely positive $\Delta G_{H*} = 1.995$ eV is observed for F-terminated Ti_3C_2 (Supplementary Fig. 3b), indicating very weak H* adsorption and easy product desorption. Unfortunately, both conditions are unfavorable for HER. Surprisingly, O-terminated Ti_3C_2 shows a near-zero value of $|\Delta G_{H*}| = 0.00283$ eV at its optimal H* coverage ($\theta = 1/2$) (Fig. 1b and Supplementary Table 1). This value is even much lower than that of Pt or highly-active earth-abundant HER catalysts (Fig. 1c), *e.g.* MoS_2 ($\Delta G_{H*} = 0.08$ eV)[23] or WS_2 ($\Delta G_{H*} = 0.22$ eV)[23], clearly indicating the remarkable HER activity of O-terminated Ti_3C_2 from the viewpoint of thermodynamics.

Apart from extraordinary HER activity, a highly-active co-catalyst must efficiently extract the photo-induced electrons from photocatalysts and deliver them to its surface, which requires appropriate electronic band structure and excellent conductivity. Hence, we employ DFT calculations to determine the band structures of Ti_3C_2, F-terminated Ti_3C_2 and O-terminated Ti_3C_2, respectively. As shown in Supplementary Fig. 4a and b, pure Ti_3C_2 exhibits metallic characteristics with substantial electronic states crossing the Fermi level. In comparison, F-terminated Ti_3C_2 (Supplementary Fig. 4c and d) and O-terminated Ti_3C_2 (Fig. 1d and e) exhibit decreased numbers of states at the Fermi level, indicating their lower conductivities. Nevertheless, the continuous electronic states crossing Fermi level for F-terminated Ti_3C_2 and O-terminated Ti_3C_2 indicate that their conductivities are still good. Hence, Ti_3C_2 retains its outstanding electrical conductivity, even after decoration with numerous functionalities, implying its exceptional capability to transport electrons. We believe this unique merit of MXene renders it a superior co-catalyst outperforming its counterparts, such as graphene and carbon nanotubes, which suffer obvious conductivity loss after their termination with -O, -OH and -COO-[11]. Furthermore, the Fermi levels (E_F) of Ti_3C_2, O-terminated Ti_3C_2 and F-terminated Ti_3C_2 are calculated to be -0.05 V, 1.88 V and 0.15 V *vs.* SHE, respectively. Among them, O-terminated Ti_3C_2 displays the most positive value of E_F, implying its strongest capacity to accept photo-induced electrons from semiconductor photocatalysts.

Based on the above theoretical explorations, it can be concluded that both pure Ti_3C_2 and F-terminated Ti_3C_2 are not eligible candidates due to their inefficient HER activity and unfavorable E_F. In contrast, O-terminated Ti_3C_2 is predicted to be a highly-promising co-catalyst, given its outstanding HER activity, excellent metallic conductivity and desirable E_F.

Design and synthesis of Ti_3C_2-incorporated CdS. The above theoretical investigations provide clear guidance to synthesize Ti_3C_2 co-catalyst and couple it with photocatalysts. Firstly, we need to obtain Ti_3C_2 terminated with abundant functionalities instead of pure Ti_3C_2. Then, we should minimize and maximize the number of -F and -O terminations on Ti_3C_2, respectively. To achieve this goal, as presented in Supplementary Fig. 5, Ti_3AlC_2 (MAX phase) powders were firstly etched by HF to remove Al species, producing exfoliated Ti_3C_2 (Ti_3C_2-E) with an accordion-like architecture (Supplementary Fig. 6a). During the etching process, Ti_3C_2-E was spontaneously decorated with substantial functionalities (-OH, -F and -O) on its surface, giving rise to its exceptional hydrophilicity. The transformation from Ti_3AlC_2 to Ti_3C_2 is firmly evidenced by the obvious shift of the (002) and (004) X-ray diffraction (XRD) peaks to lower degrees, and the disappearance of the strongest diffraction peak of Ti_3AlC_2 at 39° (Supplementary Fig. 7)[24]. To further increase the surface area and functionalities of Ti_3C_2, Ti_3C_2-E was added to de-ionized water and subjected to strong ultra-sonication, during which many large Ti_3C_2-E sheets were cut into small pieces of Ti_3C_2 NPs. The resulting suspension was centrifuged at 10000 RPM to remove the large Ti_3C_2 sheets and particles, leaving the small Ti_3C_2 NPs in the supernatant (Supplementary Fig. 8a). The successful formation of Ti_3C_2 NPs is supported by the XRD pattern (Supplementary Fig. 7 and Supplementary Note 1), high-angle annular dark-field (HAADF) image (Supplementary Fig. 8b), energy-dispersive X-ray spectra (EDX) elemental mapping images (Supplementary Fig. 8c-f), X-ray photoelectron spectroscopy (XPS) survey spectrum (Supplementary Fig. 9a), and high-resolution XPS spectra of Ti 2p, O 1s and F 1s (Supplementary Fig. 9b, c and d). The presence of abundant hydrophilic functionalities (-O, -OH and -F) on Ti_3C_2 NPs is supported by the high-resolution XPS spectrum of O 1s and F 1s (Supplementary Fig. 9c and d). Meanwhile, the “black” colloid dispersion of Ti_3C_2 exhibits a typical Tyndall effect (Supplementary Fig. 8a inset), reasonably suggesting the formation of a homogeneous dispersion of Ti_3C_2 NPs. The engineering of three-dimensional (3D) Ti_3C_2-E into zero-dimensional (0D) Ti_3C_2 NPs dramatically increased their surface area and functionalities, thus greatly favoring their intimate coupling with photocatalysts.

Then, CdS was selected as the photocatalyst to couple with Ti_3C_2, since its reported conduction band (CB) potential (-0.7 V *vs.* SHE)[25] is much more negative than the E_F of O-terminated Ti_3C_2 (1.88 V *vs.* SHE). Besides, to obtain the desired functionalities on Ti_3C_2, a hydrothermal strategy is applied to integrate CdS with Ti_3C_2 NPs. So the -F terminations can be replaced by -O or -OH in the aqueous environment during hydrothermal treatment. The synthesis process is shown in Supplementary Fig. 10. Ti_3C_2 NPs were firstly introduced into $Cd(Ac)_2$ aqueous solution, in which Cd^{2+} cations were easily adsorbed on numerous -O terminations. Then, an organic sulphur source, thiourea, was added into the above suspension and coordinated with Cd^{2+}. Finally, the resulting suspension was subjected to hydrothermal treatment. During this process, most of the -F terminations on Ti_3C_2 NPs were replaced by -O/-OH terminations, and thiourea molecules decomposed to gradually release S^{2-} anions into the solution. These S^{2-} anions were combined with the Cd^{2+} cations adsorbed on the surface of Ti_3C_2 NPs, leading to the heterogeneous nucleation and growth of CdS NPs on Ti_3C_2 NPs. Meanwhile, the excessive Cd^{2+} cations were also combined with these S^{2-} anions, resulting in the homogeneous nucleation and growth of pure CdS NPs. Then both CdS/Ti_3C_2 nanocomposites and CdS NPs self-assembled to form a large cauliflower-structured CdS/Ti_3C_2 sub-microsphere (SMS), with Ti_3C_2 NPs intimately coupled. The nominal mass ratios of Ti_3C_2 to CdS were 0, 0.05, 0.1, 2.5, 5 and 7.5 wt.%, and the resulting samples were labeled as CT0, CT0.05, CT0.1, CT2.5, CT5 and CT7.5, respectively. The actual mass ratios of the synthesized samples were determined by inductively coupled plasma atomic emission spectrometry (ICP-AES) (Supplementary Table 2).

Chemical composition and morphology. The chemical composition and morphology of the as-prepared samples were thoroughly investigated. Firstly, their crystal structures were characterized by XRD. The XRD patterns (Supplementary Fig. 11a) confirm that all the samples are composed of hexagonal wurtzite-structured phase CdS (JCPDS No. 77-2306). A combination of Ti_3C_2 NPs with CdS did not affect the crystal structure of CdS, suggesting that the remarkable increase in photocatalytic activity is not caused by any crystal structure alteration in CdS. Instead, it should be attributed to the Ti_3C_2 NPs deposited on its surface. However, no diffraction peaks for Ti_3C_2 are observed in Supplementary Fig. 11a, probably due to the low loading and high dispersion of Ti_3C_2 NPs on the surface of CdS.

The morphology and composition of the as-synthesized CT2.5 were further investigated by HAADF, EDX, high-resolution (HR)TEM, SEM and XPS techniques. The HAADF image of CT2.5 in Fig. 2a show that several NPs are deposited on the surface of CdS SMS, which is quite different from the smooth surface of pure CdS SMS (CT0) displayed in Supplementary Fig. 12a and b. The composition of these NPs was *in-situ* studied by EDX and HRTEM. Firstly, three points of O_2, O_3 and O_4 at these NPs were selected for EDX analysis, respectively. The results in Supplementary Fig. 13b, Fig. 2b and Supplementary Fig. 13c exhibit that Ti peaks were found, while no Cd or S peaks were observed at O_2, O_3 and O_4, suggesting that these NPs are not CdS but Ti-containing material. The HRTEM image at the O_3 point (Fig. 2c) shows a hetero-interface with lattice spacings of 1.0 nm and 0.36 nm, which are assigned to the (002) plane of Ti_3C_2[24] and (100) plane of CdS[26], respectively. This result confirms the formation of CdS/Ti_3C_2 hetero-junction. Furthermore, the SEM image of CT2.5 in Fig. 2d shows a uniform SMS structure of CdS/Ti_3C_2 with sizes of *ca.* 400-500 nm. A detailed observation in Fig. 2d suggests that CdS/Ti_3C_2 SMS has a cauliflower-structured morphology created by the self-assembly of many

NPs[27]. The corresponding EDX spectrum in Fig. 2e indicates that CT2.5 contains Cd, S, Ti and C, which is consistent with the HRTEM image and EDX spectra. The above results support the establishment of intimate coupling between Ti_3C_2 and CdS, implying the efficient interfacial photo-induced charge diffusion upon visible-light irradiation[7,28]. Moreover, the high-resolution XPS spectrum of Ti 2p exhibits four deconvoluted peaks in Fig. 2f, corresponding to Ti-O 2p and Ti-C 2p[24], in agreement with the above HRTEM and EDX results. It should be noted that numerous -O terminations are present in CT2.5 (Fig. 2g), while the F content is negligible for CT2.5 (Fig. 2h), suggesting the successful replacement of -F by -O/-OH on Ti_3C_2 NPs after hydrothermal treatment. Thus, the ratio of F to O in CT2.5 is zero.

Super high photocatalytic H_2-produciton performance. The photocatalytic H_2-production activity of all the as-prepared samples was examined in 18 vol.% lactic acid aqueous solution under visible-light irradiation ($\lambda \geq 420$ nm). Excitingly, the coupling of Ti_3C_2 NPs with CdS indeed leads to a remarkable enhancement in the photocatalytic activity. As displayed in Fig. 3a, pristine CdS (CT0) shows a very low photocatalytic activity of 105 μmol h^{-1} g^{-1}. In contrast, the loading of a small amount of Ti_3C_2 NPs (0.05 wt.%) obviously improves the photocatalytic activity of CT0.05 to 993 μmol h^{-1} g^{-1}. With increasing amount of Ti_3C_2 NPs, the photocatalytic activity of Ti_3C_2-loaded CdS is gradually enhanced. Surprisingly, a super high photocatalytic H_2-production activity of 14342 μmol h^{-1} g^{-1} is achieved on CT2.5, exceeding that of CT0 by an amazing factor of 136.6. In comparison, for the same loading (2.5 wt.%) and experimental conditions, NiS, Ni and MoS_2-loaded CdS SMS (NiS-CdS, Ni-CdS and MoS_2-CdS) exhibit lower photocatalytic activities of 12953, 8649 and 6183 μmol h^{-1} g^{-1}, respectively (Fig. 3a). Besides, CT2.5 also shows higher quantum efficiency (40.1% at 420 nm) than the other noble-metal-free CdS-based photocatalysts reported to date, such as: Ni/CdS, $Ni(OH)_2$/CdS, Ni_2P/CdS, CoP/CdS, graphene oxide/CdS and MoS_2/CdS (Supplementary Table 3). On the basis of the above experimental data and literature, Ti_3C_2 NPs have proven to be one of the most active earth-abundant co-catalysts. Furthermore, CT2.5 even displays higher activity than 2.5 wt.% Pt loaded CdS SMS (Pt-CdS, 10978 μmol h^{-1} g^{-1}), even though Pt is widely accepted as the most active co-catalyst promoting H_2 production. The HAADF image, EDX elemental mapping images, TEM and HRTEM images of Pt-CdS (Supplementary Fig. 14a-f) imply that Pt is homogeneously decorated on CdS in the form of clusters (Supplementary Note 2). The size of Pt in Pt-CdS is much smaller than that of Ti_3C_2 in CT2.5, suggesting more active sites exposed on Pt than those on Ti_3C_2 for the same loading. In this case, the superior activity of CT2.5 should be ascribed to the much stronger combination between CdS and Ti_3C_2 established during hydrothermal treatment, which greatly facilitates the rapid interfacial charge transfer[7,28]. This result also highlights the huge potential of Ti_3C_2 NPs as a high-performance and low-cost co-catalyst to replace Pt. However, further increase in the loading of Ti_3C_2 NPs leads to the drastic deterioration of photocatalytic activity as reported in previous works[6,7,28,29]. This is due to the excessive Ti_3C_2 NPs covering the surface active sites and impeding the light absorption of CdS. Nevertheless, CT7.5 still retains a photocatalytic activity of 2707 μmol h^{-1} g^{-1}, much higher than that of CT0. In addition, Ti_3C_2 NPs show no activity toward H_2 production under visible-light irradiation, further supporting its role as a co-catalyst rather than a photocatalyst.

The stability of the optimized CT2.5 was further evaluated by performing the photocatalytic experiments under the same reaction conditions for seven cycles. No significant deterioration of photocatalytic activity was observed for CT2.5 during seven successive cycling tests for H_2 production (Supplementary Fig. 15a). A comparison of the crystalline phase (Supplementary Fig. 11a), morphology and size (Fig. 2a and Supplementary Fig. 15b) between the original and used

CT2.5 (CT2.5-A) shows no apparent alterations in CT2.5-A, which is in accordance to its repeated high activity.

Light-harvesting capability. To investigate the origin of the remarkable activity of CT2.5, its properties governing the three major processes in photocatalytic reactions (*i.e.* light absorption, charge separation and transfer, and surface redox reactions[1,4-6]) were thoroughly characterized. Firstly, the light-harvesting capability of CT2.5 was measured by the UV-Vis diffuse reflectance spectra. As displayed in Fig. 3b, the light absorption of CT2.5 is obviously increased throughout the entire region of 350-800 nm, due to the black color of loaded Ti_3C_2 NPs (Fig. 3b inset). Similar phenomenon is also observed for CT0.05, CT0.1, CT5 and CT7.5 (Supplementary Fig. 11b). The UV-Vis absorbance spectrum of the Ti_3C_2 NPs aqueous solution shows no obvious absorption edge in the 250-800 nm region, implying the metallic nature of Ti_3C_2 NPs. Furthermore, no apparent shift in the absorption edge of CT2.5 is observed, indicating that Ti, C, F or O element is not doped into the crystal structure of CdS, which is in agreement with the above XRD data. To investigate whether the increased visible-light absorption originating from Ti_3C_2 NPs enhanced the photocatalytic activity of CT2.5, a 560 nm light filter was employed to cut off any irradiation light with wavelength shorter than 557 nm (the onset absorption edge of CdS in CT2.5), while other experimental conditions were kept identical. Under such conditions, CT2.5 shows no activity for H_2 production, indicating that the enhanced visible-light absorption arising from Ti_3C_2 NPs is unlikely to promote the activity enhancement observed for CT2.5.

Charge separation and transfer. To study the charge-carrier separation and transfer efficiency in CT2.5, a series of characterization techniques including time-resolved and steady-state photoluminescence (PL) spectra, electrochemical impedance spectra (EIS) and transient photocurrent (TPC) response were used. As shown in Fig. 3c, in comparison to CT0, CT2.5

shows an increased short (τ_1), long (τ_2) and intensity-average (τ) PL lifetimes, indicating that the deposition of Ti_3C_2 on CdS can effectively suppress the charge recombination and elongate the lifetime of charge carriers. The enhanced charge separation efficiency is further confirmed by the quenched emission peak around 560 nm for CT2.5 (Supplementary Fig. 16). Furthermore, the surface and bulk charge transfer efficiencies were investigated by the EIS and TPC density measurements, respectively. As indicated in Fig. 3d, CT2.5 shows a much smaller semicircle diameter and a much lower interfacial charge-transfer resistance than those of CT0 in potassium phosphate buffer solution (pH = 7) under visible-light irradiation, suggesting the apparent enhancement of interfacial charge-carrier transfer on the surface of CdS/Ti_3C_2. On the other hand, to study the bulk charge transfer in CT0 and CT2.5, the TPC density measurements were conducted. Na_2S and Na_2SO_3 were applied as electrolytes to rapidly capture the photo-induced holes on the surface of CT0 and CT2.5. Thus, these hole scavengers were supposed to eliminate the surface charge recombination on CT0 and CT2.5. In such a case, the observed enhancement in the TPC density upon loading of Ti_3C_2 (Fig. 3d inset) directly reflects an improved charge separation efficiency in the bulk of CdS/Ti_3C_2.

To gain further insights into the charge separation and transfer mechanism in CT2.5, the CB and valence band (VB) potentials of CdS in CT2.5 were determined to be -0.79 V and 1.54 V *vs.* SHE, respectively, by a combination of Mott-Schottky and Tauc plots (Supplementary Fig. 17a and b). Hence, upon light irradiation, the photo-induced electrons on the CB of CdS (E_{CB} = -0.79 V *vs.* SHE) in CT2.5 can promptly migrate to O-terminated Ti_3C_2 NPs, which rapidly shuttle these photo-induced electrons to their surface active sites, because of their low E_F position and excellent conductivity. Therefore, in the case of CT2.5, Ti_3C_2 can serve as an electron trapping and shuttling site not only to suppress the charge recombination on the surface of CdS, but also to promote the charge separation and transfer in the bulk of CdS, which is consistent with the above results.

Surface catalytic redox reactions. Following the charge separation and transfer, the last step in photocatalytic H_2 production includes the surface redox reactions catalyzed by the reactive sites on CT2.5. Therefore, to study the efficiency of the last step, we determined the specific surface area and pore volume of all the samples by N_2 sorption analysis (Supplementary Fig. 18a and b). As shown in Supplementary Table 2, an initial increase in the loading of Ti_3C_2 NPs up to 1.89 wt.% (CT0.05, CT0.1 and CT2.5) caused a gradual enlargement in the specific surface area of the CdS/Ti_3C_2 composites. However, further increase in the loading of Ti_3C_2 NPs resulted in a noticeable decrease in surface area to 3.8 m^2 g^{-1} and 3.7 m^2 g^{-1} for CT5 and CT7.5, respectively, despite that Ti_3C_2 NPs exhibit a large surface area of 120.1 m^2 g^{-1} (Supplementary Table 4). This decrease is observed at higher loadings of Ti_3C_2 NPs because of their tendency to aggregate on the surface of CdS SMS. Hence, the highest surface area of CT2.5 among all the CdS/Ti_3C_2 composites suggests the existence of abundant active sites on its surface, which greatly promote the surface redox catalytic reactions. Moreover, the polarization curves of CT0, CT2.5 and Ti_3C_2 NPs (Supplementary Fig. 19) indicate that the presence of Ti_3C_2 NPs on the surface of CdS can greatly improve the HER activity of CT2.5, and consequently, contribute to its enhanced photocatalytic H_2 production.

To further reveal the differences in HER mechanistic behavior between Ti_3C_2 and other state-of-the-art earth-abundant HER catalysts, *e.g.* MoS_2 and WS_2, DFT calculations were conducted to study the effect of H_2 coverage on ΔG_{H*} for O-terminated Ti_3C_2. Fig. 1b shows that one O-terminated Ti_3C_2 unit cell tends to allow for adsorption of four H* due to its smallest $|\Delta G_{H*}|$ (Supplementary Note 3), corresponding to the unsaturated H* coverage of $\theta = 1/2$. The $|\Delta G_{H*}|$

values for the adsorption of H* on O-terminated Ti_3C_2 at θ values below 1/2 (*i.e.*, θ = 1/8, 1/4 and 3/8) are relatively low (Supplementary Table 1). However, the further increase of H* coverage results in a rapid increase of $|\Delta G_{H*}|$ and deterioration of HER activity (Fig. 1b and Supplementary Table 1). Nevertheless, O-terminated Ti_3C_2 still possesses a relatively large number of HER active sites considering its large surface with numerous active sites. In comparison, the HER active sites of well-known MoS_2 and WS_2 are only located at the edge positions, while all the sites in the basal plane are inactive[30], suggesting the superiority of this newly-developed O-terminated Ti_3C_2.

Photocatalytic H_2-production mechanism and discussion. To gain an insight into the influence of intrinsic properties of Ti_3C_2 on the photocatalytic activity of the CdS/Ti_3C_2 composite, a series of experiments were designed and conducted. Firstly, the effect of co-catalyst's surface area on the activity was studied. Co-catalysts Ti_3C_2-E, Ti_3C_2-5000 and Ti_3C_2 NPs with different sizes (Supplementary Fig. 6a, 20 and 8a) and corresponding surface areas (Supplementary Table 4) were respectively coupled with CdS at the same loading (2.5 wt.%) under identical hydrothermal conditions. As shown in Fig. 4a, loading Ti_3C_2-E, Ti_3C_2-5000 and Ti_3C_2 NPs with increasing surface area leads to gradually enhanced photocatalytic activities. This is because the smaller size and larger number of exposed active sites of Ti_3C_2 not only result in stronger coupling with CdS, but also assure better access to reactants. Secondly, the influence of functionalities of co-catalyst on the activity of CdS/Ti_3C_2 was investigated. Ti_3C_2 NPs were subjected to a hydrothermal treatment to reduce the number of -F terminations. The surface atomic ratio of F to O, estimated by XPS analysis, for Ti_3C_2 NPs and hydrothermally treated Ti_3C_2 NPs (HT-Ti_3C_2 NPs) are 20.6 % and 8.0 %, respectively. This implies that a large number of the -F terminations were exchanged into -O/-OH terminations for HT-Ti_3C_2 NPs during hydrothermal treatment.

Then Ti_3C_2 NPs and HT-Ti_3C_2 NPs were mechanically mixed with CT0 at the same loading (2.5 wt.%), respectively. Fig. 4b displays that HT-Ti_3C_2 NPs induce a higher photocatalytic activity of 1527 μmol h^{-1} g^{-1} than Ti_3C_2 NPs (1105 μmol h^{-1} g^{-1}), even though the surface area of HT-Ti_3C_2 NPs (56.7 m^2 g^{-1}) is much lower than that of Ti_3C_2 NPs (120.1 m^2 g^{-1}) as shown in Supplementary Table 4. The reason for this is that the replacement of -F by -O/-OH on Ti_3C_2 NPs increases the density of effective active sites (-O terminations), despite the decreased surface area after hydrothermal treatment. This result coincides with the above DFT calculation data of ΔG_{H*} on O-terminated and F-terminated Ti_3C_2.

Based on the above experimental results and theoretical calculations, a photocatalytic mechanism illustrating the surprisingly high photocatalytic H_2-production activity of CT2.5 is proposed in Fig. 4c and d. Since the original E_F of n-type CdS (slightly lower than its CB position of -0.91 V *vs.* SHE) is much more negative than the original E_F of O-terminated Ti_3C_2 (1.88 V *vs.* SHE), the intimate contact between CdS and Ti_3C_2 in CT2.5 leads to the electron transfer from CdS to Ti_3C_2 (Supplementary Note 4), accompanied by the rise of E_F for Ti_3C_2 above the hydrogen evolution potential (0.00 V *vs.* SHE) and the equilibrium of E_F in CdS/Ti_3C_2 system. The similar phenomenon was reported by Jakob *et al*[31]. Moreover, the CB position of CdS in CT2.5 is also lowered to -0.79 V *vs.* SHE as confirmed in Supplementary Fig. 17a. Meanwhile, the immobilized positive charges remain in CdS near the CdS/Ti_3C_2 interface, where a space charge layer is formed, and the CB and VB of CdS are bent “upward”. Hence, a Schottky junction is formed between Ti_3C_2 and CdS. Upon visible-light ($\lambda \geq 420$ nm) irradiation, the electrons are excited from the VB to the CB of CdS. Due to the reduced space charge layer thickness in nano-sized CdS primary particles, the “upward” bending of the CB and VB for CdS is also limited (Fig. 4c)[32]. Hence, the photo-induced electrons in the CB can still migrate across the “upward” bent CB to the Fermi level of Ti_3C_2, leaving the photo-induced holes in the VB of CdS. As a result, the Schottky junction can serve as an electron trap to efficiently capture the photo-induced electrons, without impeding the electron transfer from CdS to Ti_3C_2, as reported in previous works[33-35]. After being transferred to Ti_3C_2, the photo-induced electrons are further rapidly shuttled to its surface, due to the excellent metallic conductivity. Finally, thanks to the outstanding HER capacity of Ti_3C_2, the protons in the aqueous solution are efficiently reduced by the photo-induced electrons at the abundant -O terminations on Ti_3C_2 to evolve H_2 gas. Therefore, through tuning the number and type of surface functionalities on Ti_3C_2, one can achieve the desirable E_F and optimize the HER activity for Ti_3C_2, which imposes a pronounced synergetic enhancement effect on the photocatalytic activity of the CdS/Ti_3C_2 system.

The potential of this newly-developed co-catalyst can be further exploited by a co-loading strategy. For instance, a p-type semiconductor NiS could be simultaneously loaded with Ti_3C_2 NPs on CdS SMS. Surprisingly, the photocatalytic activity of CdS/1 mol.% NiS/2.5 wt.% Ti_3C_2 (CNT2.5) was further increased to 18560 μmol h^{-1} g^{-1} as presented in Supplementary Fig. 21a. This is because the combination of p-type NiS with n-type CdS results in the formation of a p-n junction, which promotes the transfer of photo-induced holes from CdS to NiS. Meanwhile, the photo-induced electrons are rapidly extracted from CdS to Ti_3C_2 NPs for H_2 evolution. Therefore, the co-loading strategy imposes a strong synergistic effect on the charge separation and transfer in CNT2.5, which is confirmed by combined techniques of PL spectra (Supplementary Fig. 22a) and TPC response (Supplementary Fig. 22b). These results demonstrate the great potential of co-loading Ti_3C_2 with other co-catalysts to achieve synergetic enhancement of photocatalytic activity.

Ti_3C_2 as a versatile HER co-catalyst. To verify that the Ti_3C_2 NPs can act as a versatile HER co-catalyst on different photocatalysts, we mechanically mixed Ti_3C_2 NPs with $Zn_xCd_{1-x}S$ and ZnS respectively, and tested the photocatalytic H_2-production activity of the resultant mixtures. As shown in Supplementary Fig. 23a and 24a, a simple mechanical mixing of $Zn_{0.8}Cd_{0.2}S$ (ZCS) and ZnS with 1 wt.% Ti_3C_2 NPs increased the photocatalytic activities of the formed composites ZCS/Ti_3C_2 and ZnS/Ti_3C_2 by 386% and 217%, respectively, as compared to that of pristine ZCS and ZnS. This exciting finding clearly shows an enormous potential in coupling Ti_3C_2 NPs with a wide variety of semiconductor photocatalysts/photoelectrodes.

Discussion

This work demonstrates the great advantage of using modern theoretical tools for the design and synthesis of a novel MXene material, Ti_3C_2 NPs, as a highly-active co-catalyst. Based on theoretical predictions, we rationally employed the hydrothermal treatment to replace the -F terminations on Ti_3C_2 by -O/-OH terminations, and coupled the pretreated Ti_3C_2 with CdS to prepare a highly-fused CdS/Ti_3C_2 composite photocatalyst. Remarkably, this composite photocatalyst exhibited both super high visible-light photocatalytic activity (14342 μmol h^{-1} g^{-1}) and apparent quantum efficiency (40.1% at 420 nm), rendering it as one of the best noble-metal-free metal-sulfides photocatalysts. By combining the first-principle calculations and experimental methodology, we found that this unusual activity can be attributed to the synergetic effect of the highly-efficient charge separation and migration from CdS to Ti_3C_2 NPs and the rapid H_2 evolution on numerous -O terminations present on Ti_3C_2 NPs. Successful application of Ti_3C_2 NPs as an efficient co-catalyst on ZnS or ZCS excitingly confirms the versatile nature of this newly-developed co-catalyst. This study opens a new area of utilizing this new generation of co-catalytic materials, MXene, to achieve highly efficient, steady and cost-effective solar water splitting based on semiconductor photocatalysts/photoelectrodes.

Methods

Materials synthesis. Ti_3AlC_2 (MAX phase: $M_{n+1}AX_n$, where M indicates early transition metal, A indicates III A or IV A group element, and X indicates C or N) was synthesized following the approach reported by Peng *et al*[36]. Ti_3C_2-E was prepared by immersing Ti_3AlC_2 in HF solution. Ti_3C_2 NPs were fabricated by ultra-sonication of Ti_3C_2-E in de-ionized water. The detailed synthesis procedures of Ti_3AlC_2, Ti_3C_2-E and Ti_3C_2 NPs are described in Supplementary Methods. The CdS/Ti_3C_2 composites were fabricated by a one-step hydrothermal method summarized in Supplementary Methods. Pt-CdS was synthesized by *in situ* photo-deposition of 2.5 wt.% Pt on CT0 using H_2PtCl_6 aqueous solution. Pt NPs loaded CT0 (Pt-CdS-1) was synthesized by mixing 2.5 wt% Pt NPs with CT0 in ultra-sonication followed by washing with ethanol and dried at 60 °C. The morphology (Supplementary Fig. 25a) and photocatalytic activity (Supplementary Fig. 26) of Pt-CdS-1 are discussed in Supplementary Note 5. The above Pt NPs (Supplementary Fig. 27) was synthesized by a chemical-reduction method summarized in Supplementary Methods. NiS-CdS was synthesized following the previosuly reported method[37] using CT0 as the substrate with 2.5 wt% loading of NiS. Ni-CdS was synthesized by *in situ* photo-deposition of 2.5 wt% Ni on CT0 using $Ni(NO_3)_2$ aqueous solution. MoS_2-CdS was synthesized by the previously reported method[38] using CT0 as the substrate with 2.5 wt% loading of MoS_2. Ti_3C_2-5000 was synthesized following the preparation method of Ti_3C_2 NPs except that the final product was obtained by centrifugation at 5000 RPM. CT2.5-5000 was prepared following the preparation method of CT2.5 except that Ti_3C_2-5000 was used instead of Ti_3C_2 NPs. HT-Ti_3C_2 NPs were synthesized following the hydrothermal method for preparation of CT2.5 except that no $Cd(Ac)_2$ was added. CT2.5-A was acquired after the repeated photocatalytic reaction of CT2.5 for 28 h. 1 mol% NiS loaded CT0 (CN) was synthezised by following the previously reported method[39]. CNT2.5 was synthesized by a one-step hydrothermal method as summarized in Supplementary Methods. The phase structures (Supplementary Fig. 21b) and optical properties (Supplementary Fig. 21c) of CN and CNT2.5 are discussed in Supplementary Note 6. ZCS was synthesized by the previously reported method[39]. ZCS/Ti_3C_2 was synthesized by mechanical mixing of the as-synthesized ZCS with 1 wt.% Ti_3C_2 NPs. The phase structures (Supplementary Fig. 23b) and optical properties (Supplementary Fig. 23c) of ZCS and ZCS/Ti_3C_2 are discussed in Supplementary Note 7. ZnS was prepared by a hydrothermal approach as summarized in Supplementary Methods. ZnS/Ti_3C_2 was prepared by mechanical mixing of the as-synthesized ZnS with 1 wt.% Ti_3C_2 NPs. The phase structures (Supplementary Fig. 24b) and optical properties (Supplementary Fig. 24c) of ZCS and ZCS/Ti_3C_2 are discussed in Supplementary Note 8.

Physicochemical Characterization. XRD patterns were acquired on a powder X-ray diffractometer (Miniflex, Rigaku) using Cu-Kα radiation at 40 kV and 15 mA. SEM images and EDX spectra were collected on FEI Quanta 450 at an accelerating voltage of 10 kV. HAADF, TEM, HRTEM images and EDX were performed by utilizing a JEM-2100F electron microscope (JEOL, Japan). XPS measurements were conducted using an Axis Ultra (Kratos Analytical, UK) XPS spectrometer equipped with an Al Kα source (1486.6 eV). The F/O atomic ratios in all the CdS/Ti_3C_2 composites were examined by XPS technique (Supplementary Fig. 28) and discussed in Supplementary Note 9. The Brunauer-Emmett-Teller specific surface areas (S_{BET}) and pore volume (PV) of the samples were evaluated by N_2 adsorption on a Tristar II 3020 gas adsorption apparatus (Micromeritics, USA). UV-Vis diffuse reflectance spectra were collected for the dry-pressed disk samples with a UV-Vis spectrophotometer (UV2600, Shimadzu, Japan) using $BaSO_4$ as the reflectance standard. PL spectra were recorded on a RF-5301PC spectrofluorophotometer (Shimadzu, Japan) at room temperature. Time-resolved PL decay curves were obtained on a FLS920 fluorescence lifetime spectrophotometer (Edinburgh Instruments, UK) under the excitation of 365 nm and probed at 460 nm. The actual chemical compositions of the as-synthesized samples were measured by ICP-AES using an Optima 4300 DV spectrometer (PerkinElmer) (Supplementary Table 2).

Theoretical calculations. The DFT calculations were carried out by using the Vienna *ab initio* simulation package (VASP)[40,41]. The exchange-correlation interaction is described by generalized gradient approximation (GGA) with the Perdew-Burke-Ernzerhof (PBE) functional[42]. Van der Waals correction was applied in all calculations. The energy cut-off was set to 500 eV. The Brillouin zone was sampled by a Monkhorst-Pack 9×9×1 K-point grid. The fully relaxed lattice constants of Ti_3C_2, O-terminated Ti_3C_2 and F-terminated Ti_3C_2 monolayers are 3.08 Å, 3.01 Å and 3.02 Å respectively. The models of Ti_3C_2, O-terminated Ti_3C_2 or F-terminated Ti_3C_2 in 2×2×1 supercells with a k-point of 5×5×1 grid in reciprocal space are used to identify the HER activity sites. HSE06 calculations[43,44] employing VASP are performed to get the exact band structures. The band gap is zero. The further calculation details of the Gibbs free energy of the absorption of atomic H, the Fermi level positions and the surface Pourbaix diagrams can be found in Supplementary Methods. The surface Pourbaix diagram (Supplementary Fig. 29) of Ti_3C_2 is analyzed and discussed in Supplementary Note 10. The excellent conductivity of O-terminated Ti_3C_2 at different H coverages (Supplementary Fig. 30) is confirmed in Supplementary Note 11.

Photocatalytic H_2 production test. The experimental measurements of photocatalytic H_2 production were carried out in a 100 ml Pyrex flask (openings sealed with silicone rubber septum) at room temperature and atmospheric pressure. A 300 W Xenon arc lamp with an ultraviolet-cutoff filter ($\lambda \geq 420$ nm) was utilized as a visible light source to trigger the photocatalytic reaction. The focused intensity on the flask was *ca.* 80 mW cm^{-2}. Typically, 20 mg of the photocatalyst was suspended by constant stirring in 80 ml of mixed aqueous solution containing 20 ml of lactic acid (88 vol%) and 60 ml of water. Prior to irradiation, the suspension was purged with Argon for 0.5 h to remove any dissolved air and keep the reaction system under anaerobic conditions. Next, 0.2 ml gas was intermittently sampled through the septum, and H_2 content was analyzed by gas chromatograph (Clarus 480, PerkinElmer, USA, TCD, Ar as a carrier gas and 5 Å molecular sieve column). Before the experiment, all glassware was rinsed carefully with deionized water. The apparent quantum efficiency (QE) was measured under the identical photocatalytic reactions. Four low power 420-nm LEDs (3 W, Shenzhen LAMPLIC Science Co. Ltd. China) were employed as the light sources to trigger the photocatalytic reactions. The focused intensity for every 420-nm LED was *ca.* 6 mW cm^{-2}. The QE was calculated according to the following equation (1):

$$\mathrm{QE}[\%] = \frac{\text{number of reacted electrons}}{\text{number of incident photons}} \times 100$$

$$= \frac{\text{number of evolved } H_2 \text{ molecules} \times 2}{\text{number of incident photons}} \times 100 \qquad (1)$$

Electrochemical and photoelectrochemical measurements. EIS measurements were performed on an electrochemical analyzer (CHI650D instruments) in a standard three-electrode system utilizing the synthesized samples as the working electrodes, Ag/AgCl (saturated KCl) as a reference electrode, and a Pt wire as the counter electrode. The polarization curves were recorded in the above-mentioned three-electrode system and the bias sweep range was from -1.5 to -0.8 V *vs.* Ag/AgCl with a step size of 0.005 V. 0.5 M Na_2SO_4 aqueous solution was utilized as the electrolyte. The Mott-Schottky plots were also measured using the same three-electrode system over an alternating current (AC) frequency of 1200 Hz in 0.5 M Na_2SO_4 aqueous solution. The EIS were recorded over a range from 1 to 2×10^5 Hz with an AC amplitude of 0.02 V. 0.5 M potassium phosphate buffer solution was used as the electrolyte. Photocurrent was measured in the same three-electrode system. A 300 W Xenon light with an ultraviolet cut-off filter ($\lambda \geq 420$ nm) was applied as the light source. 0.2 M Na_2S and 0.04 M Na_2SO_3 mixed aqueous solution was used as the electrolyte. The working electrodes were synthesized as follows: 0.1 g sample and 0.03 g polyethylene glycol (PEG; Molecular weight: 20000) were ground with 0.5 mL of ethanol to make a slurry. Then the slurry was coated onto a 2 cm × 1.5 cm FTO glass electrode by the doctor blade approach. The obtained electrode was dried in an oven and heated at 623 K for 0.5 h under flowing N_2. All working electrodes studied were kept at a similar film thickness of about 10-11 μm.

Data availability. The data that support the findings of this study are available from the corresponding author on request.

References

1 Hisatomi, T., Kubota, J. & Domen, K. Recent advances in semiconductors for photocatalytic and photoelectrochemical water splitting. *Chem. Soc. Rev.* **43,** 7520-7535 (2014).

2 Ran, J. *et al.* Porous P-doped graphitic carbon nitride nanosheets for synergistically enhanced visible-light photocatalytic H_2 production. *Energy Environ. Sci.* **8,** 3708-3717 (2015).

3 Fujishima, A. & Honda, K. Electrochemical photolysis of water at a semiconductor electrode. *Nature* **238,** 37-38 (1972).

4 Chen, X., Shen, S., Guo, L. & Mao, S. S. Semiconductor-based photocatalytic hydrogen generation. *Chem. Rev.* **110,** 6503-6570 (2010).

5 Kudo, A. & Miseki, Y. Heterogeneous photocatalyst materials for water splitting. *Chem. Soc. Rev.* **38,** 253-278 (2009).

6 Ran, J. *et al.* Earth-abundant cocatalysts for semiconductor-based photocatalytic water splitting. *Chem. Soc. Rev.* **43,** 7787-7812 (2014).

7 Zong, X. *et al.* Enhancement of photocatalytic H_2 evolution on CdS by loading MoS_2 as cocatalyst under visible light irradiation. *J. Am. Chem. Soc.* **130,** 7176-7177 (2008).

8 Hou, Y. *et al.* Bioinspired molecular co-catalysts bonded to a silicon photocathode for solar hydrogen evolution. *Nat. Mater.* **10,** 434-438 (2011).

9 Bi, W. *et al.* Molecular co-catalyst accelerating hole transfer for enhanced photocatalytic H_2 evolution. *Nat. Commun.* **6,** 8647 (2015).

10 Mahler, B., Hoepfner, V., Liao, K. & Ozin, G. A. Colloidal synthesis of 1T-WS_2 and 2H-WS_2 nanosheets: applications for photocatalytic hydrogen evolution. *J. Am. Chem. Soc.* **136,** 14121-14127 (2014).

11 Hernandez, Y. *et al.* High-yield production of graphene by liquid-phase exfoliation of graphite. *Nat. Nanotech.* **3,** 563-568 (2008).

12 Brown, K. A. *et al.* Characterization of photochemical processes for H_2 production by CdS nanorod-[FeFe] hydrogenase complexes. *J. Am. Chem. Soc.* **134,** 5627-5636 (2012).

13 Wang, F. *et al.* A highly efficient photocatalytic system for hydrogen production by a robust hydrogenase mimic in an aqueous solution. *Angew. Chem. Int. Ed.* **50,** 3193-3197 (2011).

14 Khazaei, M. *et al.* Novel electronic and magnetic properties of two-dimensional transition metal carbides and nitrides. *Adv. Funct. Mater.* **23,** 2185-2192 (2013).

15 Gao, Y. *et al.* Hydrothermal synthesis of TiO_2/Ti_3C_2 nanocomposites with enhanced photocatalytic activity. *Mater. Lett.* **150,** 62-64 (2015).

16 Naguib, M. *et al.* New two-dimensional niobium and vanadium carbides as promising materials for Li-ion batteries. *J. Am. Chem. Soc.* **135,** 15966-15969 (2013).

17 Lukatskaya, M. R. *et al.* Cation intercalation and high volumetric capacitance of two-dimensional titanium carbide. *Science* **341,** 1502-1505 (2013).

18 Ghidiu, M. *et al.* Conductive two-dimensional titanium carbide 'clay' with high volumetric capacitance. *Nature* **516,** 78-81 (2014).

19 Nørskov, J. K., Bligaard, T., Rossmeisl, J. & Christensen, C. H. Towards the computational design of solid catalysts. *Nat. Chem.* **1,** 37-46 (2009).

20 Jiao, Y., Zheng, Y., Jaroniec, M. & Qiao, S. Z. Design of electrocatalysts for oxygen- and hydrogen-involving energy conversion reactions. *Chem. Soc. Rev.* **44,** 2060-2086 (2015).

21 Nørskov, J. K. *et al.* Trends in the exchange current for hydrogen evolution. *J. Electrochem. Soc.* **152,** J23-J26 (2005).

22 Hinnemann, B. *et al.* Biomimetic hydrogen evolution: MoS_2 nanoparticles as catalyst for hydrogen evolution. *J. Am. Chem. Soc.* **127,** 5308-5309 (2005).

23 Bonde, J. *et al.* Hydrogen evolution on nano-particulate transition metal sulfides. *Faraday Discuss.* **140,** 219-231 (2009).

24 Ma, T. Y., Cao, J. L., Jaroniec, M. & Qiao, S. Z. Interacting carbon nitride and titanium carbide nanosheets for high-performance oxygen evolution. *Angew. Chem. Int. Ed.* **55,** 1138-1142 (2016).

25 Ran, J., Yu, J. & Jaroniec, M. $Ni(OH)_2$ modified CdS nanorods for highly efficient visible-light-driven photocatalytic H_2 generation. *Green Chem.* **13,** 2708-2713 (2011).

26 Chauhan, H. *et al.* Photoinduced ultrafast charge separation in colloidal 2-dimensional CdSe/CdS-Au hybrid nanoplatelets and corresponding application in photocatalysis. *Nanoscale* **8,** 15802-15812 (2016).

27 Rengaraj, S. *et al.* Cauliflower-like CdS microspheres composed of nanocrystals and their physicochemical properties. *Langmuir* **27,** 352-358 (2011).

28 Xiang, Q., Yu, J. & Jaroniec, M. Synergetic effect of MoS_2 and graphene as cocatalysts for enhanced photocatalytic H_2 production activity of TiO_2 nanoparticles. *J. Am. Chem. Soc.* **134,** 6575-6578 (2012).

29 Chang, K. *et al.* MoS_2/graphene cocatalyst for efficient photocatalytic H_2 evolution under visible light irradiation. *ACS Nano* **8,** 7078-7087 (2014).

30 Jaramillo, T. F. *et al.* Identification of active edge sites for electrochemical H_2 evolution from MoS_2 nanocatalysts. *Science* **317,** 100-102 (2007).

31 Jakob, M., Levanon, H. & Kamat, P. V. Charge distribution between UV-irradiated TiO_2 and gold nanoparticles: determination of shift in the Fermi level. *Nano Lett.* **3,** 353-358 (2003).

32 Osterloh, F. E. Inorganic nanostructures for photoelectrochemical and photocatalytic water splitting. *Chem. Soc. Rev.* **42,** 2294-2320 (2013).

33 Leung, D. Y. C. *et al.* Hydrogen production over titania-based photocatalysts. *ChemSusChem* **3,** 681-694 (2010).

34 Yan, H. *et al.* Visible-light-driven hydrogen production with extremely high quantum efficiency on Pt-PdS/CdS photocatalyst. *J. Catal.* **266,** 165-168 (2009).

35 Yang, J., Wang, D., Han, H. & Li, C. Roles of cocatalysts in photocatalysis and photoelectrocatalysis. *Acc. Chem. Res.* **46,** 1900-1909 (2013).

36 Peng, Q. *et al.* Unique lead adsorption behavior of activated hydroxyl group in two-dimensional titanium carbide. *J. Am. Chem. Soc.* **136,** 4113-4116 (2014).

37 Zhang, J., Qiao, S. Z., Qi, L. & Yu, J. Fabrication of NiS modified CdS nanorod p-n junction photocatalysts with enhanced visible-light photocatalytic H_2-production activity. *Phys. Chem. Chem. Phys.* **15,** 12088-12094 (2013).

38 Lang, D., Shen, T. & Xiang, Q. Roles of MoS_2 and graphene as cocatalysts in the enhanced visible-light photocatalytic H_2 production activity of multiarmed CdS nanorods. *ChemCatChem* **7,** 943-951 (2015).

39 Ran, J., Zhang, J., Yu, J. & Qiao, S. Z. Enhanced visible-light photocatalytic H_2 production by $Zn_xCd_{1-x}S$ modified with earth-abundant nickel-based cocatalysts. *ChemSusChem* **7,** 3426-3434 (2014).

40 Kresse, G. & Furthmüller, J. Efficient iterative schemes for *ab initio* total-energy calculations using a plane-wave basis set. *Phys. Rev. B* **54,** 11169-11186 (1996).

41 Kresse, G. & Furthmüller, J. Efficiency of ab-initio total energy calculations for metals and semiconductors using a plane-wave basis set. *Comp. Mater. Sci.* **6,** 15-50 (1996).

42 Perdew, J. P., Burke, K. & Ernzerhof, M. Generalized gradient approximation made simple. *Phys. Rev. Lett.* **77,** 3865-3868 (1996).

43 Paier, J. *et al.* Screened hybrid density functionals applied to solids. *J. Chem. Phys.* **124,** 154709 (2006).

44 Paier, J. *et al.* Erratum: "Screened hybrid density functionals applied to solids". *J. Chem. Phys.* **125,** 249901 (2006).

Acknowledgements

This work was supported financially by the Australian Research Council (ARC) through the Discovery Project program (DP160104866, DP140104062 and DP130104459).

Author contributions

J.R. and G.G. contributed equally to this work. S.-Z.Q., F.-T.L. and J.R. conceived and designed the research. J.R. synthesized photocatalysts, conducted all the experiments and wrote the paper. T.-Y.M. gave suggestions on the synthesis of photocatalysts. G.G. performed the DFT calculations, assisted by A.D. All authors discussed and analyzed the data.

Additional information

The authors declare no competing financial interests. Correspondence and requests for materials should be addressed to S.-Z.Q. (s.qiao@adelaide.edu.au)

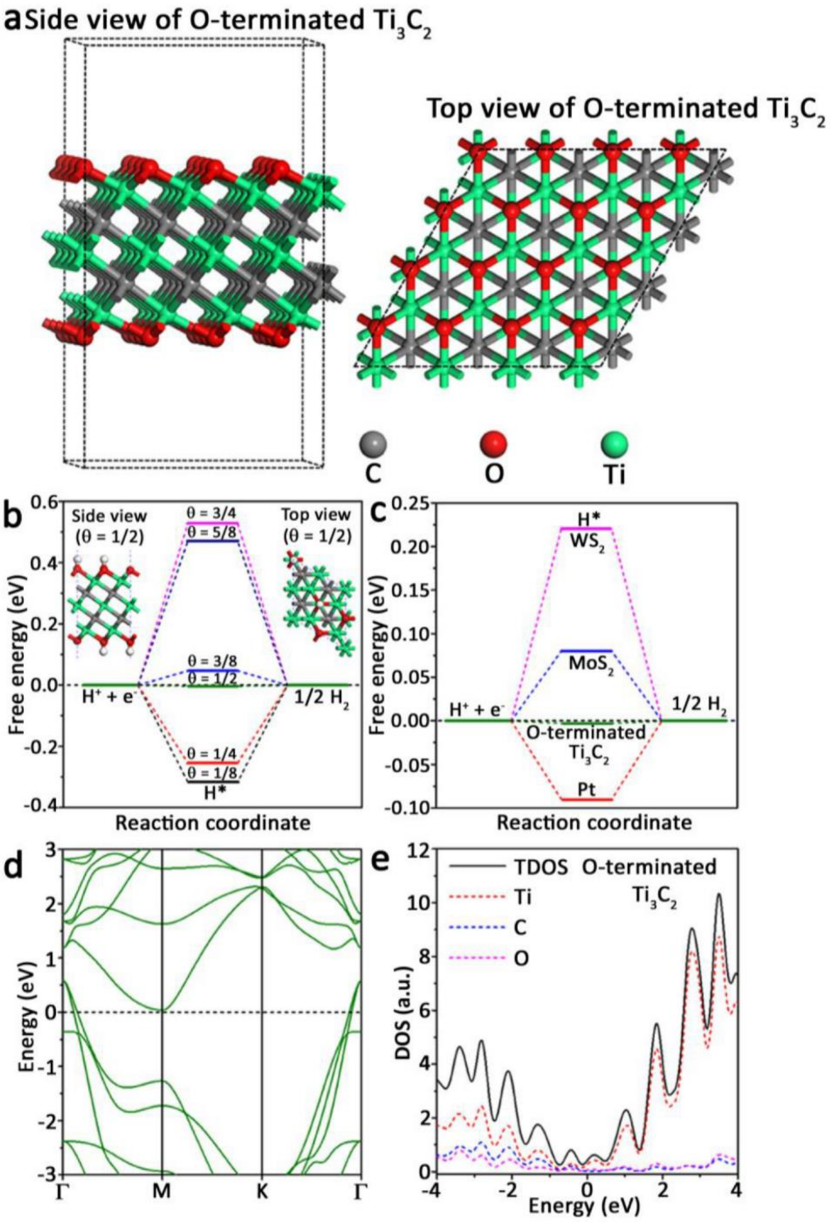

Figure 1 │ Density function theory calculation studies of O-terminated Ti$_3$C$_2$. (**a**) The side and top views of the structure model for a 4×4×1 O-terminated Ti$_3$C$_2$ supercell. Grey, red and cyan spheres denote C, O and Ti atoms, respectively. (**b**) The calculated free-energy diagram of hydrogen evolution reaction (HER) at the equilibrium potential (U = 0 V) on the surface of a 2×2×1 O-terminated Ti$_3$C$_2$ supercell at different H* coverage (1/8, 1/4, 3/8, 1/2, 5/8 and 3/4) conditions (the side and top views of a 2×2×1 O-terminated Ti$_3$C$_2$ supercell at 1/2 H* coverage are shown in the inset). (**c**) The calculated free-energy diagram of HER at the equilibrium potential (U = 0 V) on the surface of a 2×2×1 O-terminated Ti$_3$C$_2$ supercell at 1/2 H* coverage, and the referenced Pt[21,22] MoS$_2$[23], and WS$_2$[23]. (**d**) The calculated band gap of O-terminated Ti$_3$C$_2$. (**e**) The total density of states (TDOS) and partial density of states (PDOS) for O-terminated Ti$_3$C$_2$.

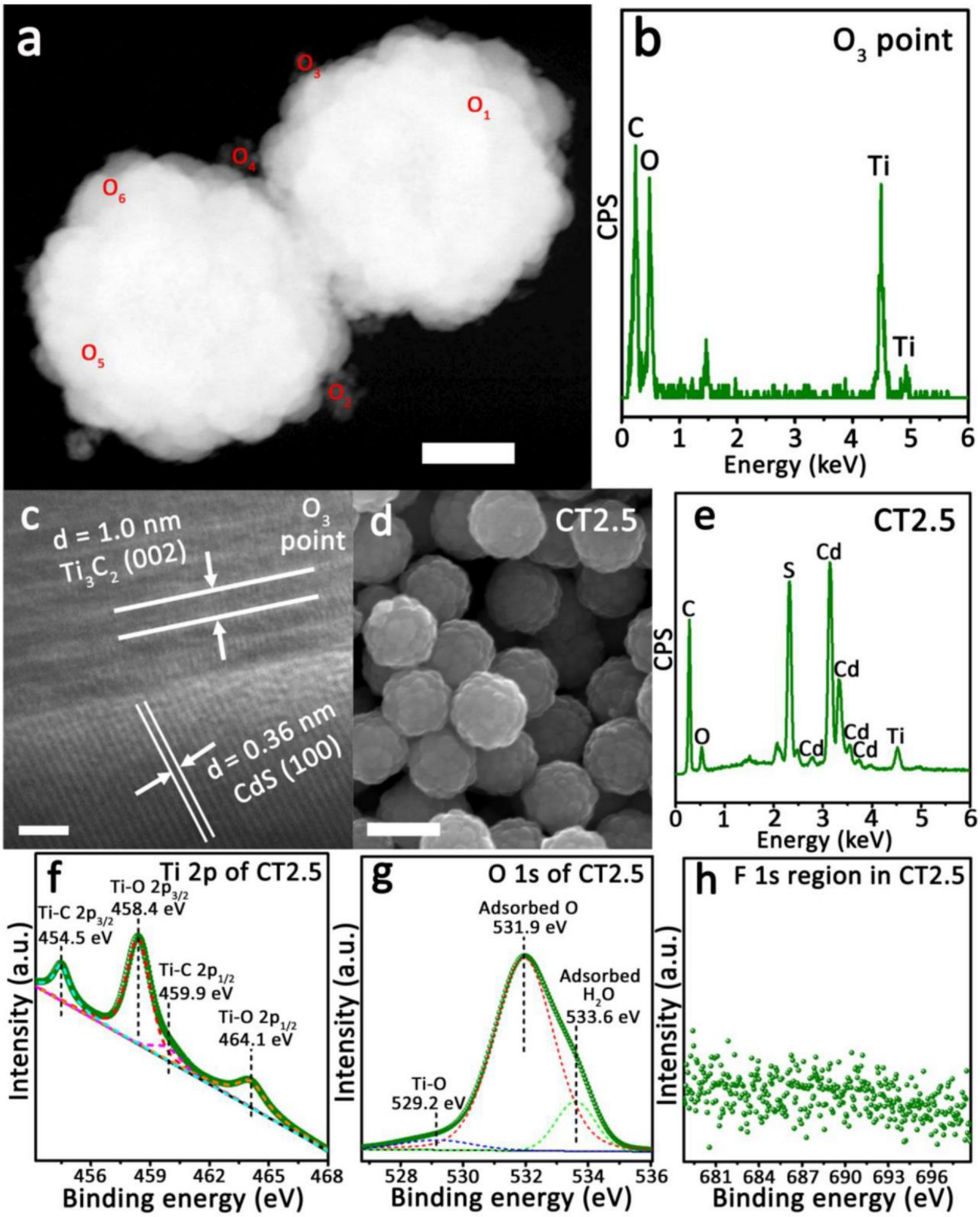

Figure 2 │ Morphology and chemical composition of CT2.5. (**a**) A typical high-angle annular dark field (HAADF) image of CT2.5 and the six different points (O_1, O_2, O_3, O_4, O_5 and O_6) for EDX analysis. (**b**) The EDX spectrum at O_3 point in Figure 2a. (**c**) The high-resolution TEM image at O_3 point in Figure 2a. (**d, e**) A typical SEM image of CT2.5 and its corresponding EDX spectrum. (**f-h**) The high-resolution XPS spectra of Ti 2p, O 1s and F 1s for CT2.5. Scale bars, 200 nm (**a**), 2 nm (**c**) and 500 nm (**d**).

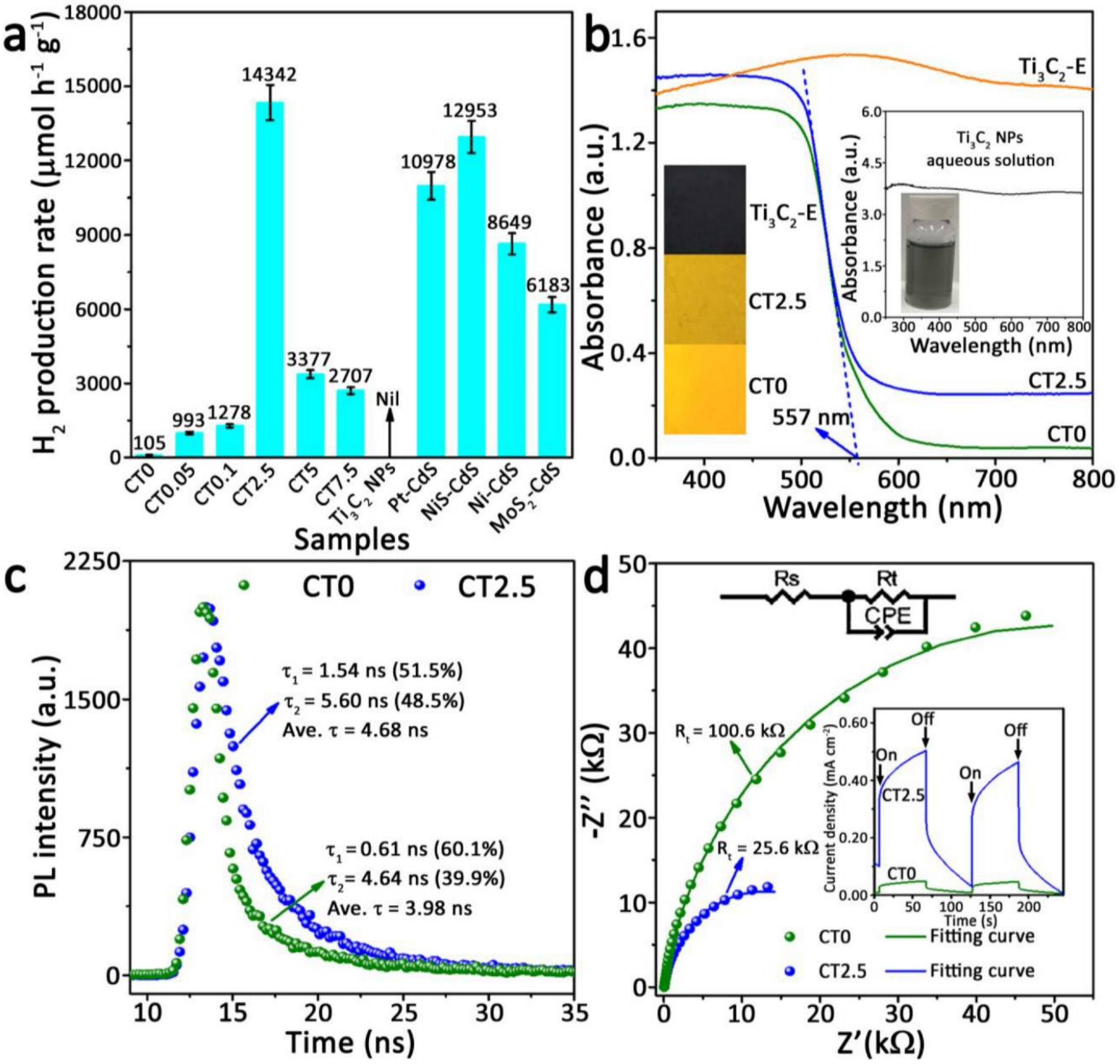

Figure 3│Photocatalytic performance and spectroscopy/(photo)electrochemical characterization. (**a**) A comparison of the photocatalytic H_2-production activities of CT0, CT0.05, CT0.1, CT2.5, CT5, CT7.5, Ti_3C_2 NPs, Pt-CdS, NiS-CdS, Ni-CdS and MoS_2-CdS. The error bars are defined as s. d. (**b**) Ultraviolet-visible (UV-Vis) diffuse reflectance spectra of CT0, CT2.5 and Ti_3C_2-E. The insets show the colors of all the samples as well as the UV-Vis absorbance spectrum and picture of the Ti_3C_2 NPs aqueous solution. (**c**) Time-resolved PL spectra of CT0 and CT2.5. (**d**) EIS Nyquist plots of CT0 and CT2.5 electrodes measured under the open-circle potential and visible-light irradiation in 0.5 M potassium phosphate buffer (pH = 7) solution. The inset shows the transient photocurrent responses of CT0 and CT2.5 electrodes in 0.2 M Na_2S + 0.04 M Na_2SO_3 mixed aqueous solution under visible-light irradiation.

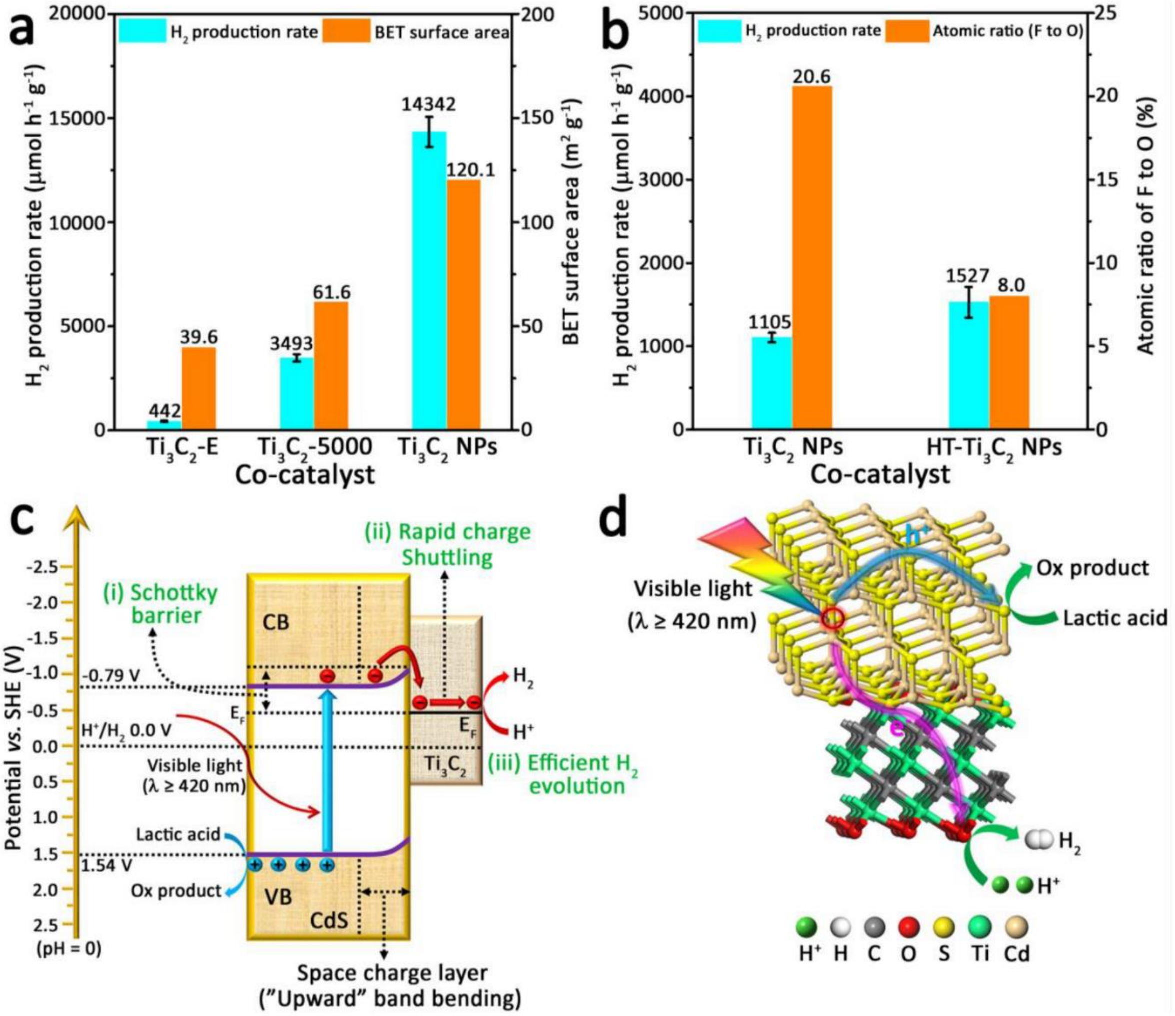

Figure 4 | Origin and mechanism of the enhanced photocatalytic performance in CdS/Ti_3C_2 system. (**a**) The influence of the co-catalyst's surface area on the photocatalytic activity. The error bars are defined as s. d. (**b**) The influence of the co-catalyst's surface F to O atomic ratio on the photocatalytic activity. The error bars are defined as s. d. (**c**) The charge separation and transfer in the CdS/Ti_3C_2 system under visible-light irradiation. (**d**) Proposed mechanism for photocatalytic H_2 production in the CdS/Ti_3C_2 system under visible-light illumination. Green sphere denotes H^+. White, grey, red, yellow, cyan and gold spheres denote H, C, O, S, Ti and Cd atoms, respectively.

Supplementary Figures

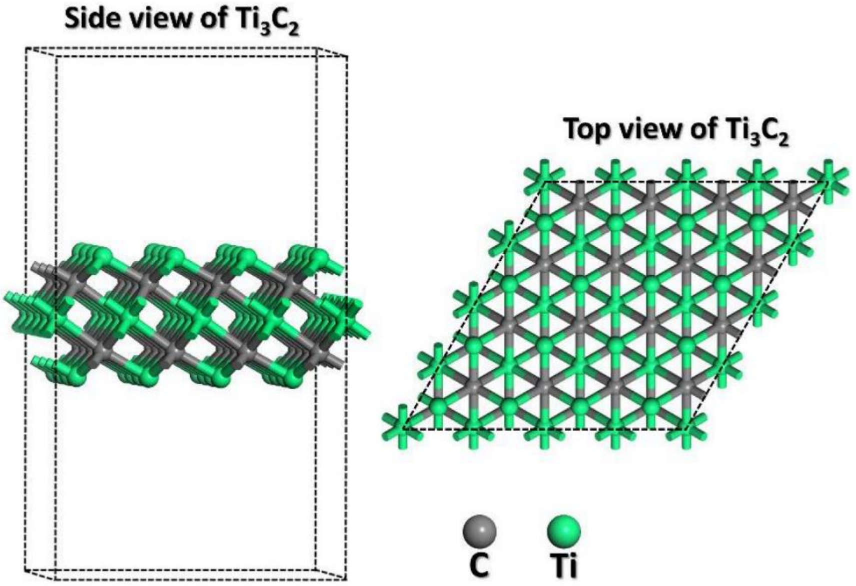

Supplementary Figure 1. The side and top views of structural model for a 4×4×1 Ti_3C_2 supercell.

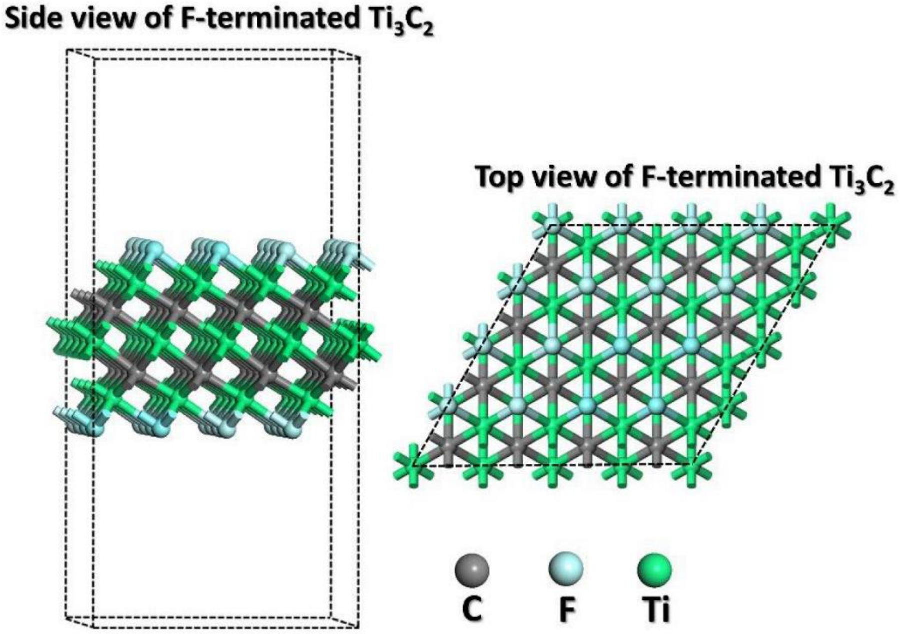

Supplementary Figure 2. The side and top views of structural model for a 4×4×1 F-terminated Ti_3C_2 supercell.

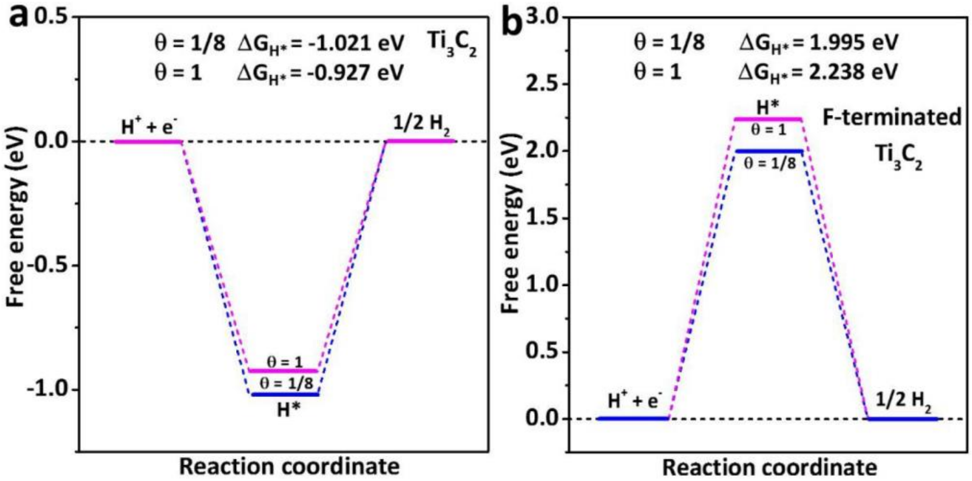

Supplementary Figure 3. (**a**) The calculated free-energy diagram of HER at the equilibrium potential (U = 0 V) on the surface of a 2×2×1 Ti_3C_2 supercell and (**b**) a 2×2×1 F-terminated Ti_3C_2 supercell under different H* coverage conditions (1/8 and 1). The insets in (**a**) and (**b**) show the calculated Gibbs free energies for H adsorption on the surface of a 2×2×1 Ti_3C_2 supercell and a 2×2×1 F-terminated Ti_3C_2 supercell with different H* coverages, respectively.

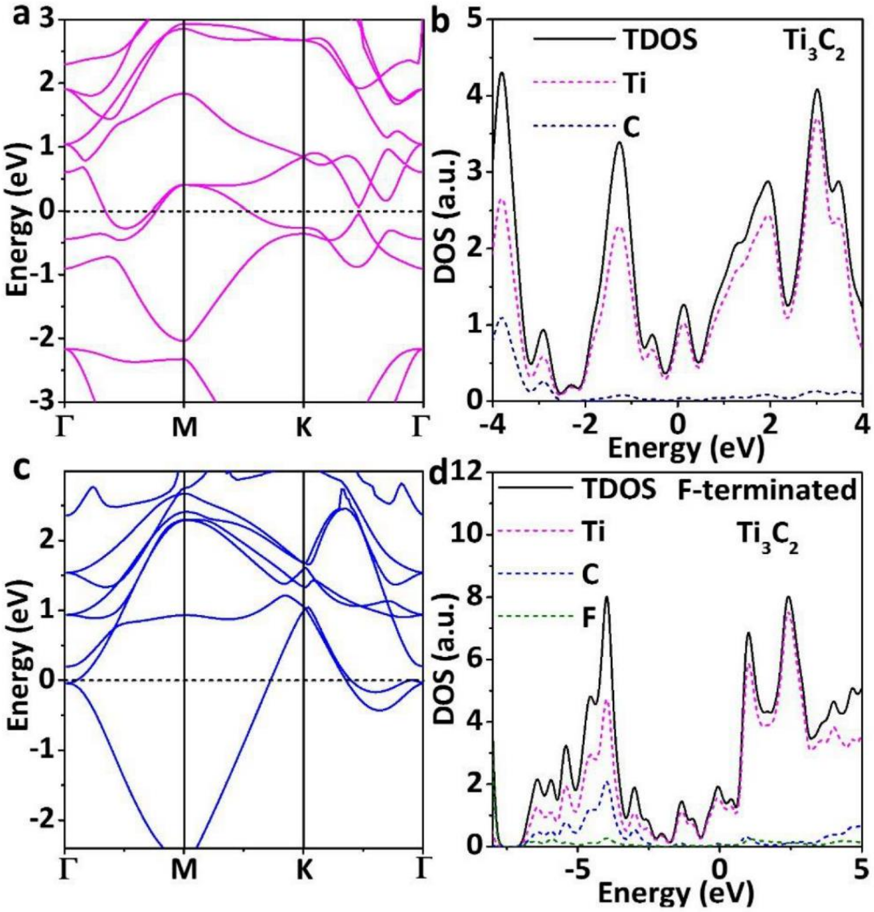

Supplementary Figure 4. (**a**) The electronic band structure and (**b**) the total density of states (TDOS) and partial density of states (PDOS) for pure Ti_3C_2. (**c**) The electronic band structure and (**d**) the TDOS and PDOS for F-terminated Ti_3C_2.

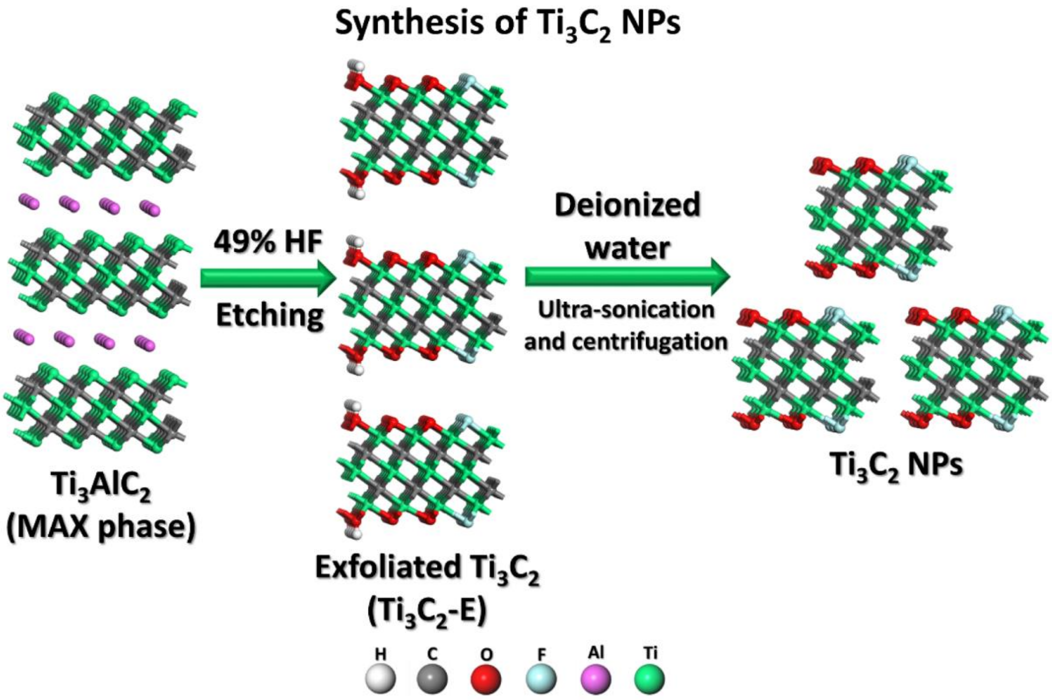

Supplementary Figure 5. Synthesis procedure of Ti_3C_2 NPs.

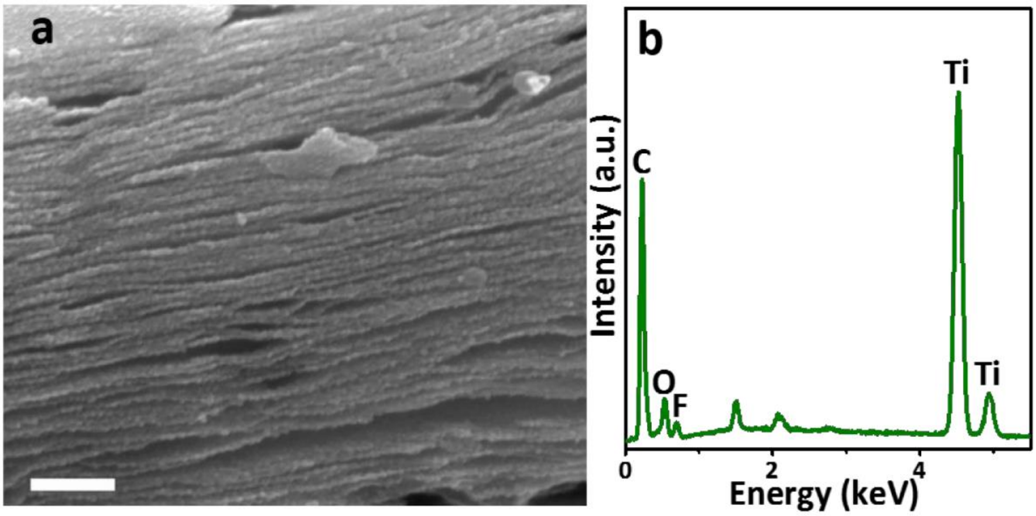

Supplementary Figure 6. (**a**) SEM image and (**b**) the corresponding EDX pattern of Ti_3C_2-E. Scale bar, 500 nm (**a**).

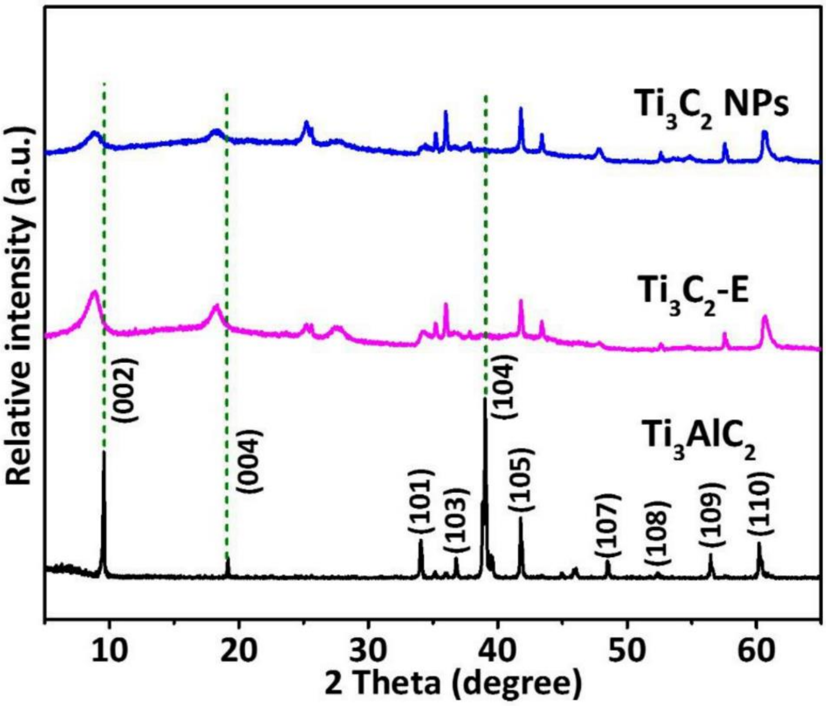

Supplementary Figure 7. XRD patterns of Ti_3AlC_2, Ti_3C_2-E and Ti_3C_2 NPs.

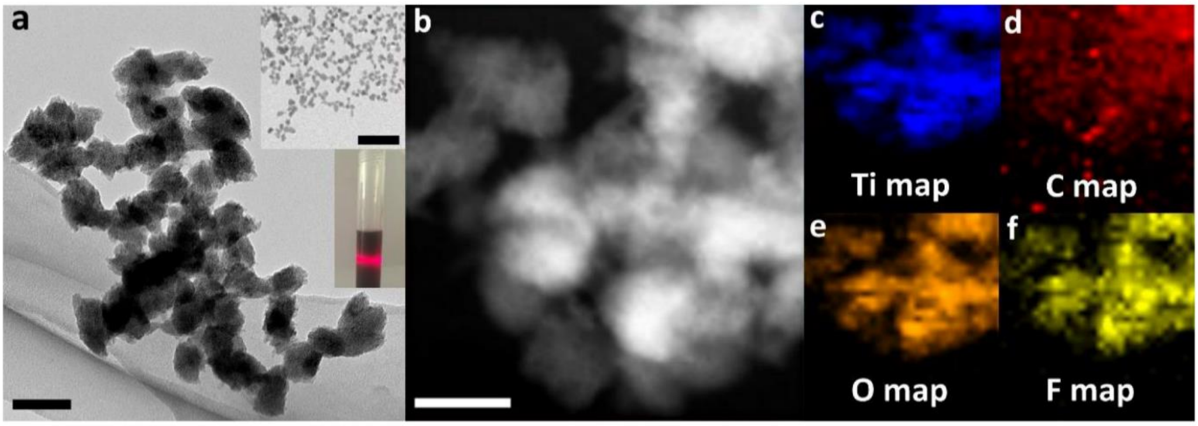

Supplementary Figure 8. (**a**) High-magnification TEM image of Ti_3C_2 NPs with inset showing the low-magnification TEM image of Ti_3C_2 NPs and the Tyndall effect of Ti_3C_2 dispersion. (**b**) HAADF image of Ti_3C_2 NPs and its corresponding EDX elemental mapping images of (**c**) Ti, (**d**) C, (**e**) O and (**f**) F. Scale bars, 100 nm (**a**), 500 nm inset in (**a**) and 50 nm (**b**).

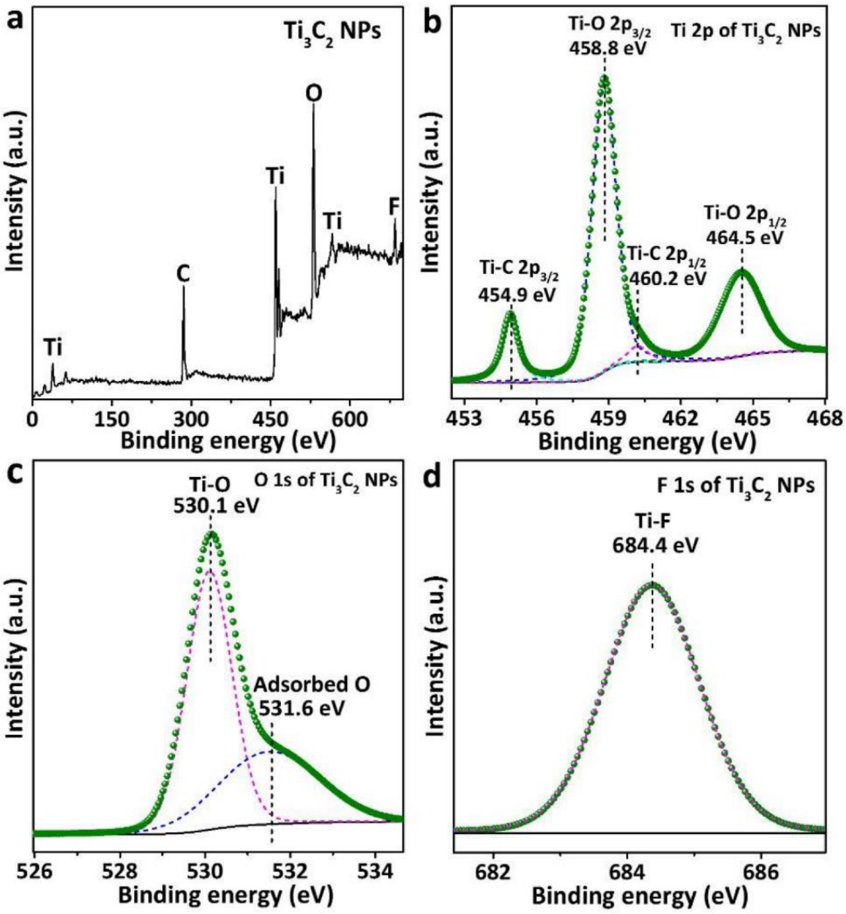

Supplementary Figure 9. (**a**) XPS survey spectrum of Ti_3C_2 NPs. High-resolution XPS spectra of (**b**) Ti 2p, (**c**) O 1s and (**d**) F 1s for Ti_3C_2 NPs.

Supplementary Figure 10. Synthesis procedure of CdS/Ti$_3$C$_2$ cauliflower-structured sub-microsphere (SMS).

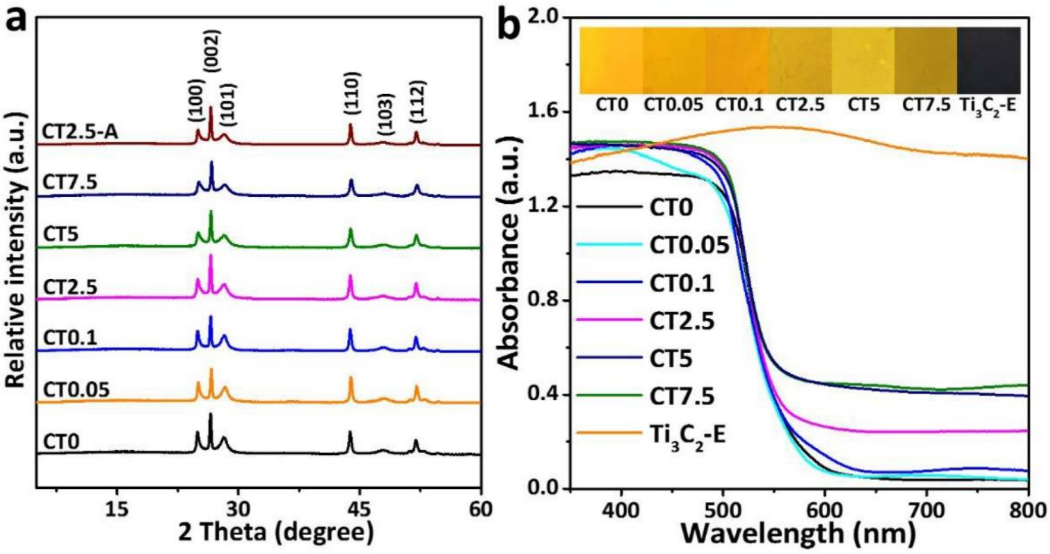

Supplementary Figure 11. (**a**) XRD patterns of CT0, CT0.05, CT0.1, CT2.5, CT5, CT7.5 and CT2.5-A. (**b**) UV-Vis diffuse reflectance spectra of CT0, CT0.05, CT0.1, CT2.5, CT5, CT7.5 and Ti$_3$C$_2$-E. The inset in (**b**) shows the colors of the above samples.

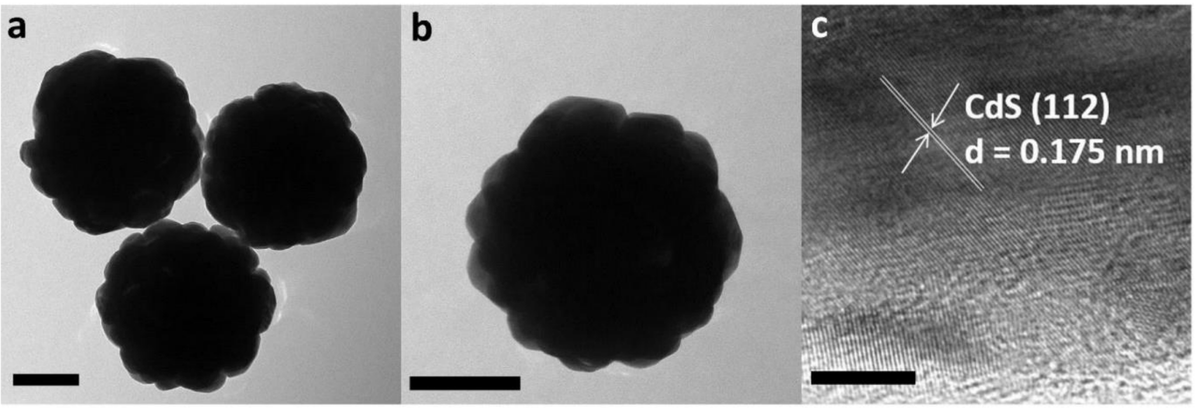

Supplementary Figure 12. (**a, b**) TEM images and (**c**) HRTEM image of CT0. Scale bars, 200 nm (**a, b**), 5 nm (**c**).

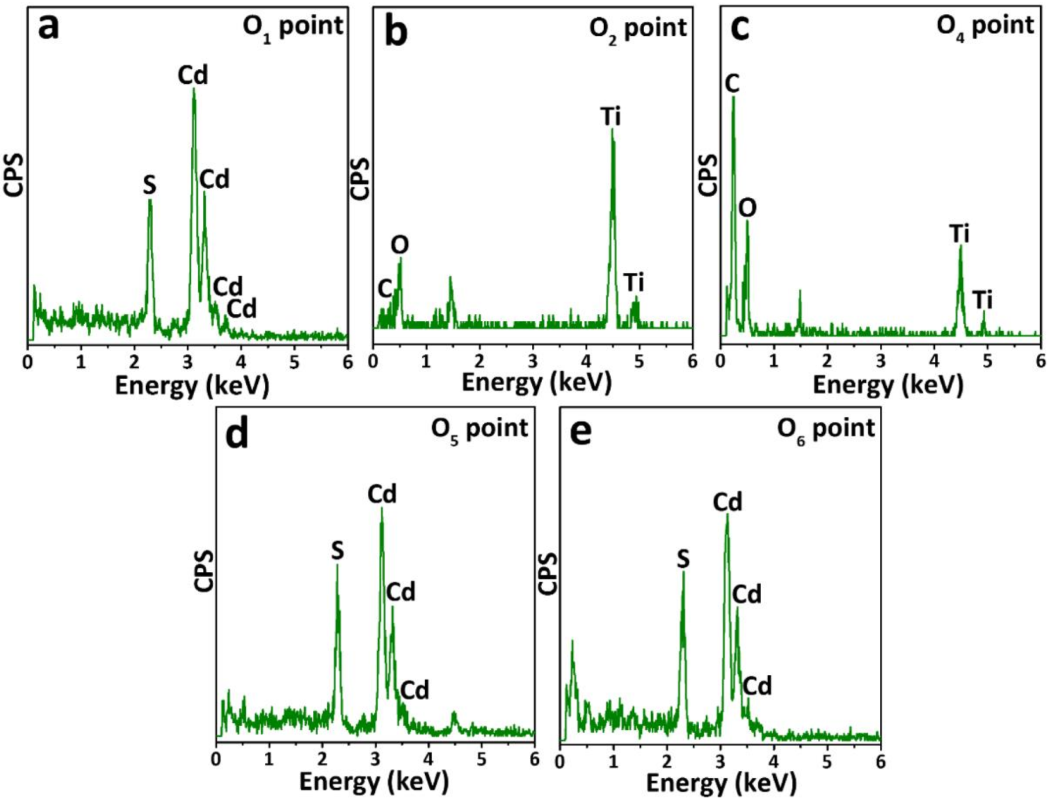

Supplementary Figure 13. The EDX spectra at (**a**) O_1, (**b**) O_2, (**c**) O_4, (**d**) O_5 and (**e**) O_6 points in Fig. 2a.

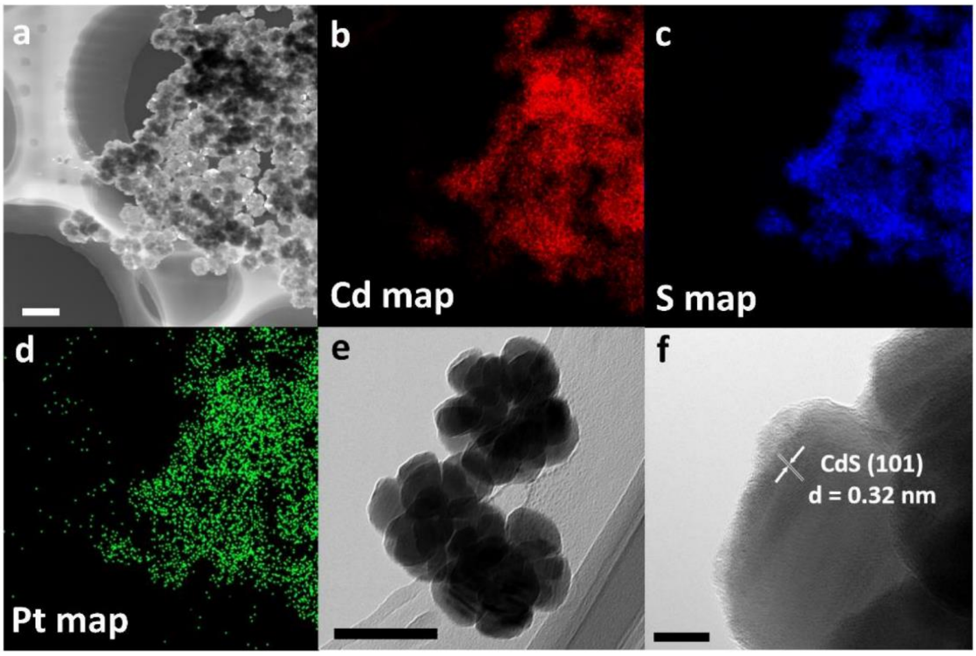

Supplementary Figure 14. (**a**) A typical HAADF image of Pt-CdS and its corresponding EDX elemental mapping images of (**b**) Cd, (**c**) S and (**d**) Pt. The typical (**e**) TEM and (**f**) HRTEM images of Pt-CdS. Scale bars, 200 nm (**a**), 100 nm (**e**) and 10 nm (**f**).

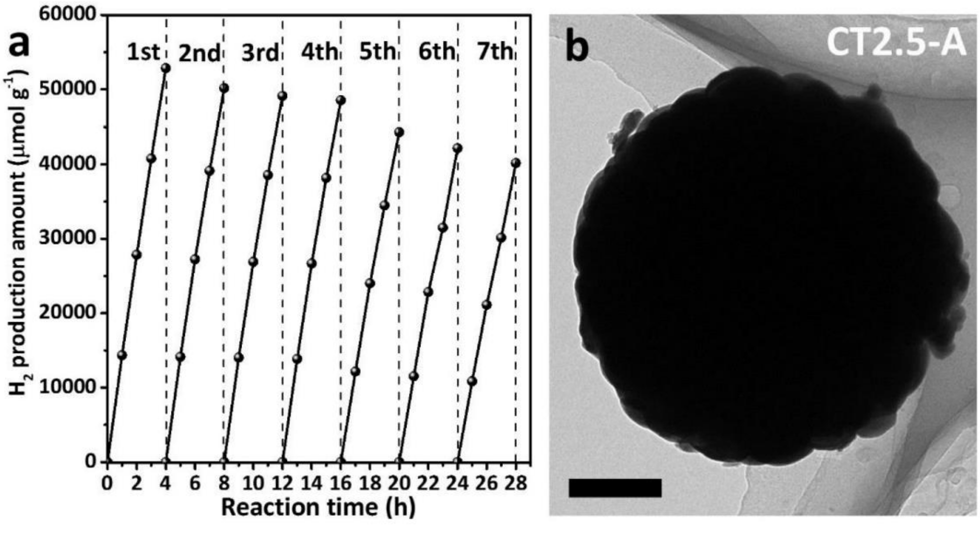

Supplementary Figure 15. (**a**) Time course of photocatalytic H_2 production over CT2.5; every 4 hours the reaction system was purged with Ar for 30 min to remove H_2. (**b**) A typical TEM image of CT2.5-A. Scale bar, 200 nm (**b**).

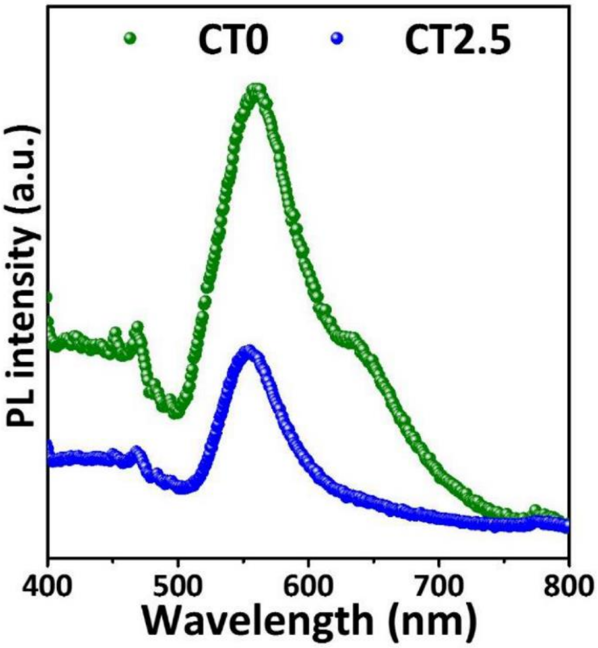

Supplementary Figure 16. PL spectra of CT0 and CT2.5.

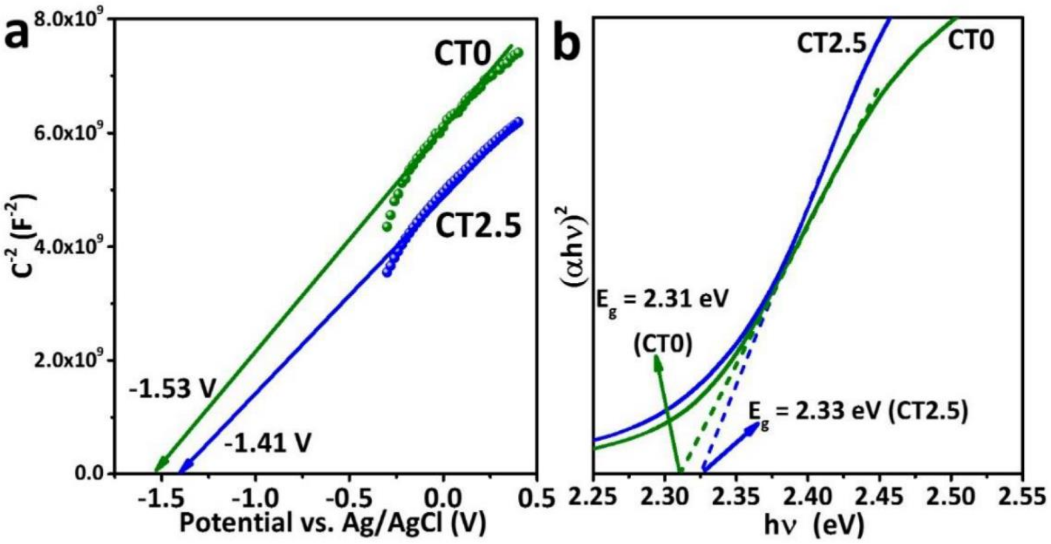

Supplementary Figure 17. (**a**) Mott-Schottky plots of CT0 and CT2.5 electrodes in 0.5 M Na_2SO_4 aqueous solution. (**b**) Tauc plots of CT0 and CT2.5.

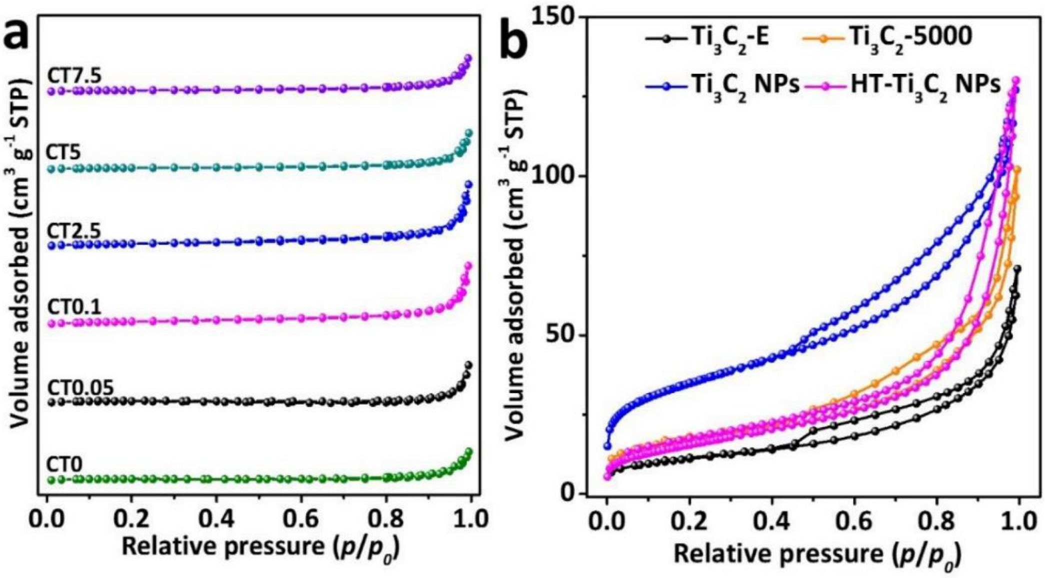

Supplementary Figure 18. (**a**) N_2 sorption isotherms of CT0, CT0.05, CT0.1, CT2.5, CT5 and CT7.5. (**b**) N_2 sorption isotherms of Ti_3C_2-E, Ti_3C_2-5000, Ti_3C_2 NPs and HT-Ti_3C_2 NPs.

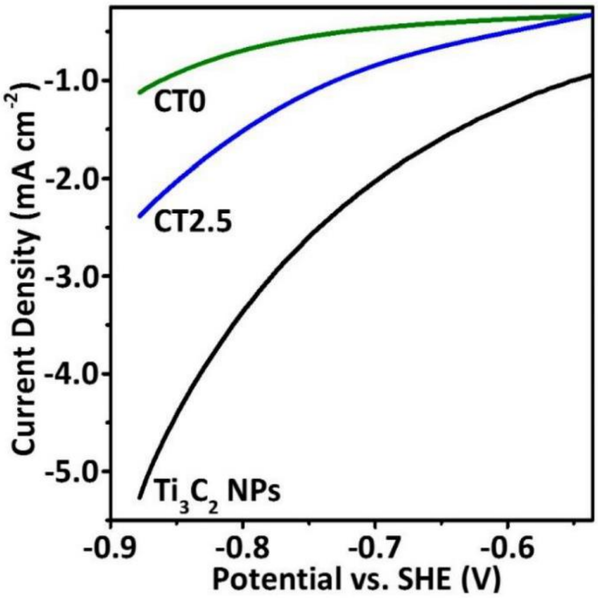

Supplementary Figure 19. Polarization curves of CT0, CT2.5 and Ti_3C_2 NPs electrodes in 0.5 M Na_2SO_4 aqueous solution.

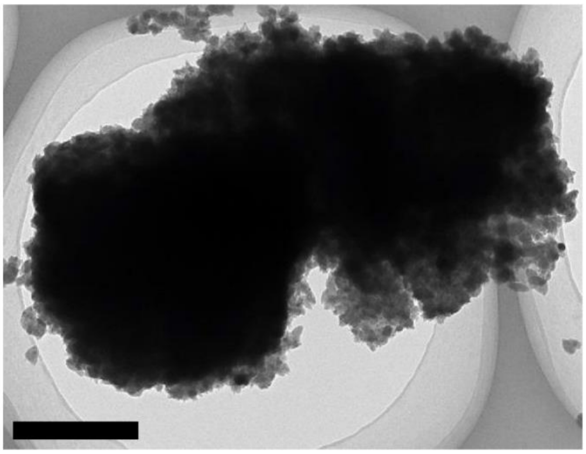

Supplementary Figure 20. TEM image of Ti_3C_2-5000. Scale bar, 500 nm.

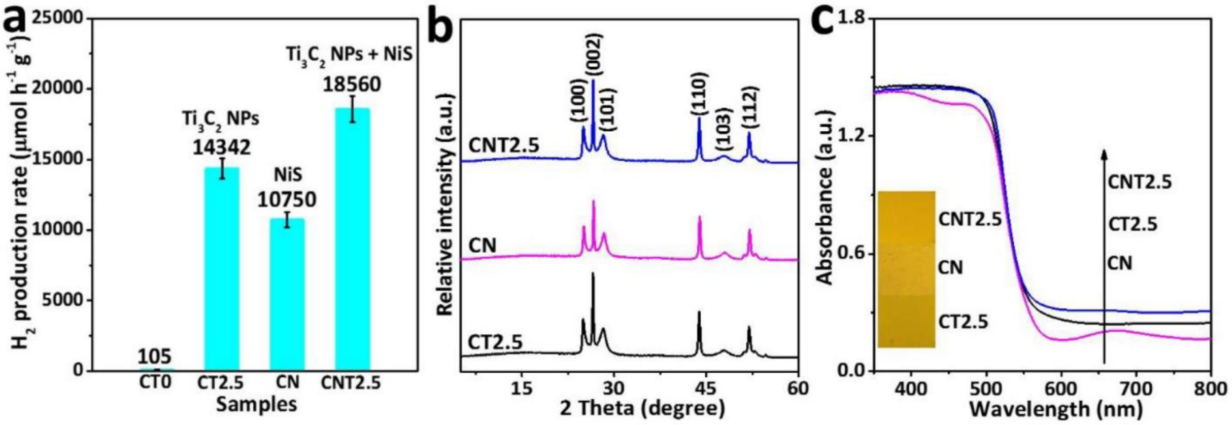

Supplementary Figure 21. (**a**) A comparison of the photocatalytic H_2-production activities of CT0, CT2.5, CN and CNT2.5, using 18 vol.% lactic acid aqueous solution as a sacrificial reagent under visible-light irradiation ($\lambda \geq 420$ nm, 300 W Xe lamp). The error bars are defined as s. d. (**b**) XRD patterns of CT2.5, CN and CNT2.5. (**c**) UV-Vis diffuse reflectance spectra of CT2.5, CN and CNT2.5. The inset shows the colors of the above samples.

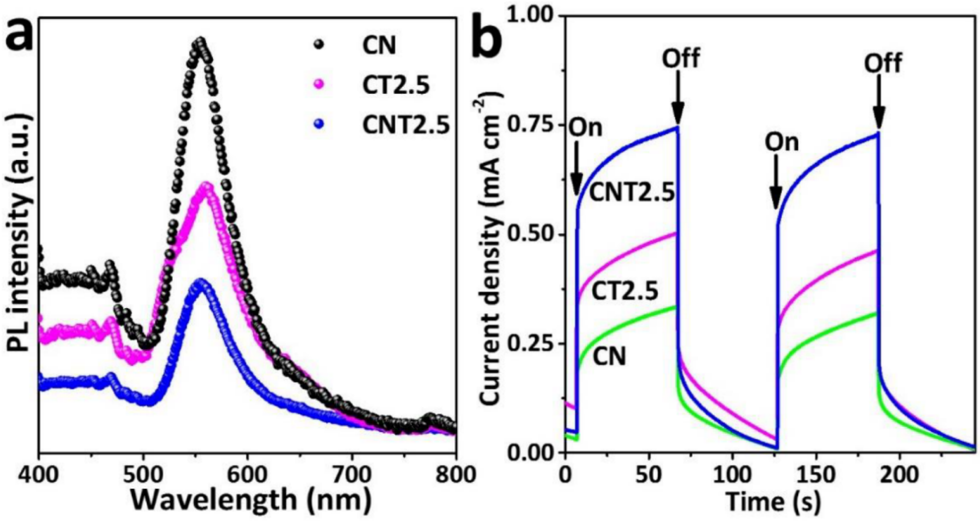

Supplementary Figure 22. (**a**) PL spectra of CT2.5, CN and CNT2.5. (**b**) TPC responses of CT2.5, CN, and CNT2.5 electrodes in 0.2 M Na_2S + 0.04 M Na_2SO_3 mixed aqueous solution under visible-light irradiation.

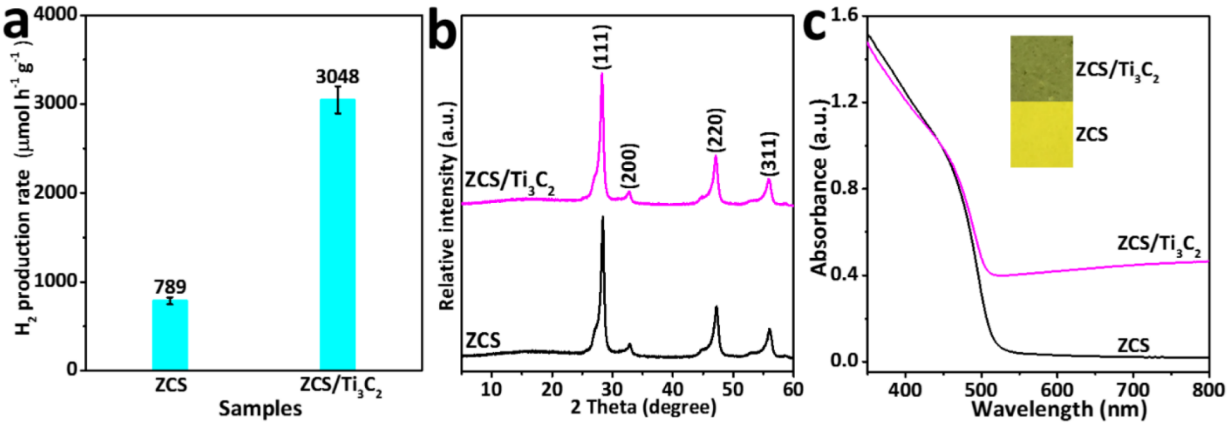

Supplementary Figure 23. (**a**) A comparison of the photocatalytic H_2-production activities of ZCS and ZCS/Ti_3C_2 using 18 vol.% lactic acid aqueous solution as a sacrificial reagent under visible-light irradiation (λ ≥ 420 nm, 300 W Xe lamp). The error bars are defined as s. d. (**b**) XRD patterns of ZCS and ZCS/Ti_3C_2. (**c**) UV-Vis diffuse reflectance spectra of ZCS and ZCS/Ti_3C_2. The inset shows the colors of the above samples.

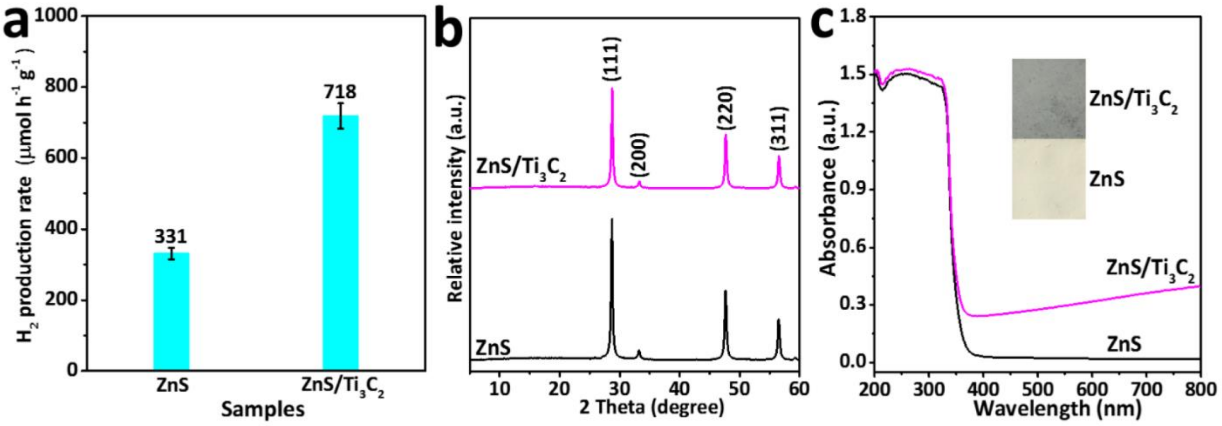

Supplementary Figure 24. (**a**) A comparison of the photocatalytic H_2-production activities of ZnS and ZnS/Ti_3C_2 using 18 vol.% lactic acid aqueous solution as a sacrificial reagent under light irradiation (300 W Xe lamp). The error bars are defined as s. d. (**b**) XRD patterns of ZnS and ZnS/Ti_3C_2. (**c**) UV-Vis diffuse reflectance spectra of ZnS and ZnS/Ti_3C_2. The inset shows the colors of the above samples.

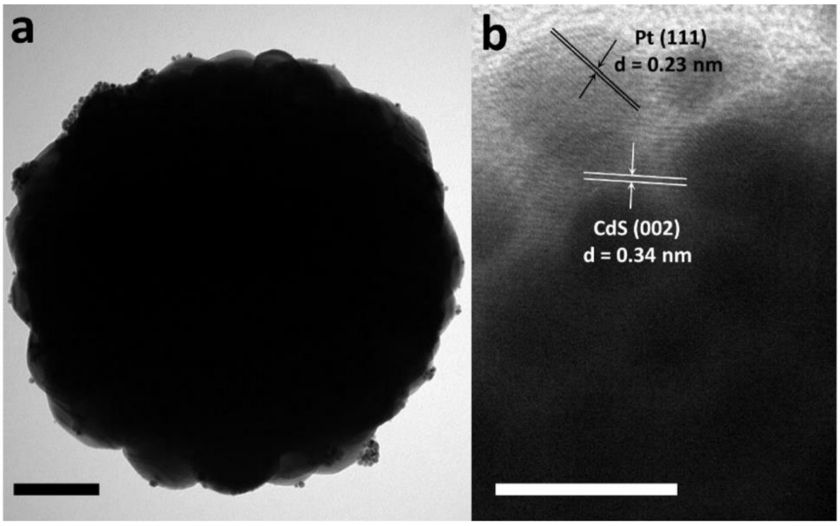

Supplementary Figure 25. The (**a**) TEM and (**b**) HRTEM images of Pt-CdS-1. Scale bars, 100 nm (**a**) and 10 nm (**b**).

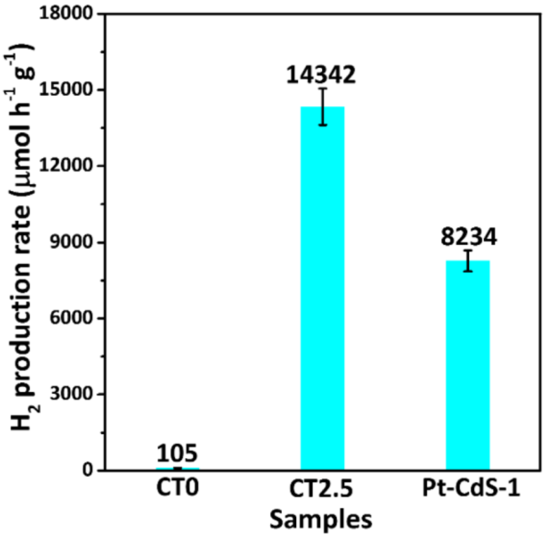

Supplementary Figure 26. A comparison of the photocatalytic H_2-production activities of CT0, CT2.5 and Pt-CdS-1 using 18 vol.% lactic acid aqueous solution as a sacrificial reagent under visible-light irradiation ($\lambda \geq 420$ nm, 300 W Xe lamp). The error bars are defined as s. d.

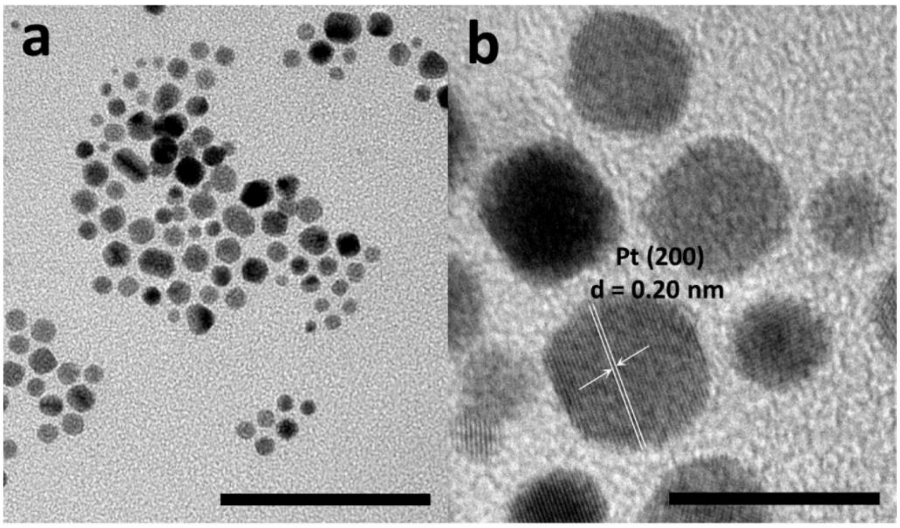

Supplementary Figure 27. The (**a**) TEM and (**b**) HRTEM images of Pt NPs synthesized by the chemical reduction method. Scale bars, 50 nm (**a**) and 10 nm (**b**).

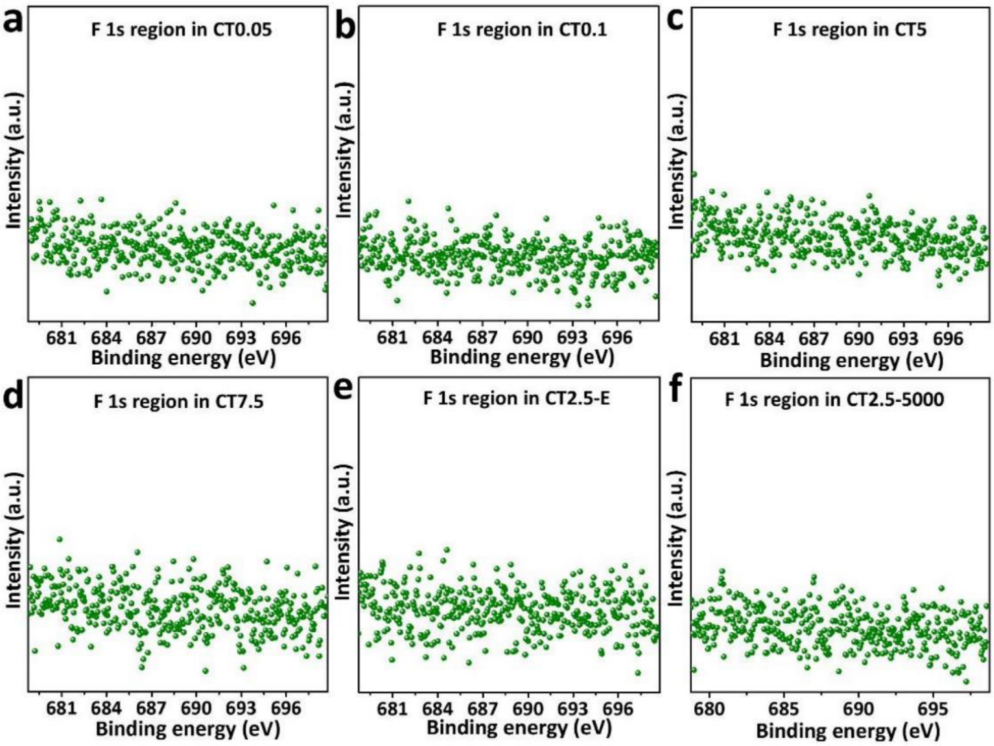

Supplementary Figure 28. The high-resolution XPS spectra of F1s for (**a**) CT0.05, (**b**) CT0.1, (**c**) CT5, (**d**) CT7.5, (**e**) CT2.5-E and (**f**) CT2.5-5000.

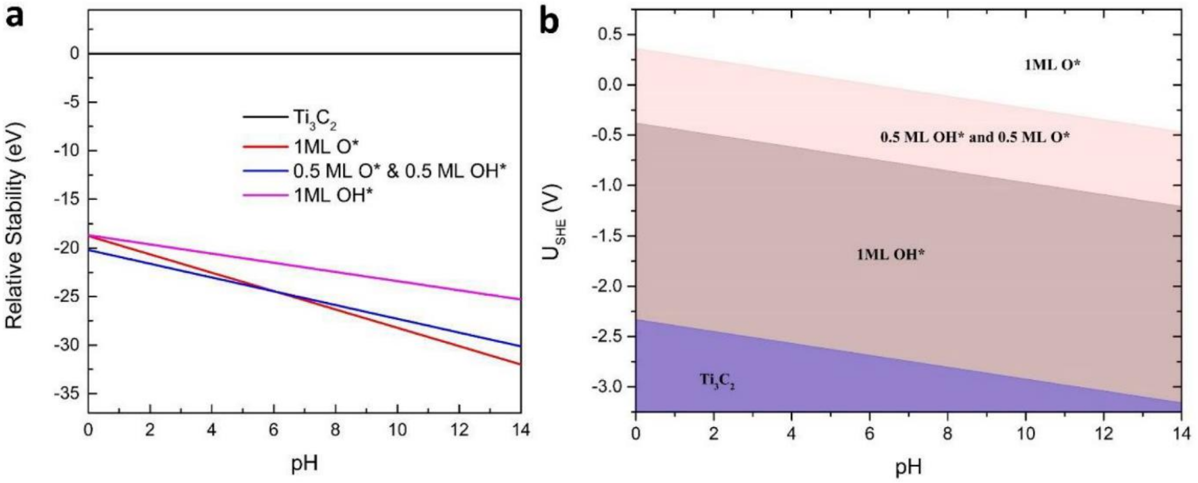

Supplementary Figure 29. (**a**) Stability of O* and OH* on Ti_3C_2 at $U_{SHE} = 0$ including alkaline and acidic dissolution. (**b**) Surface Pourbaix diagram for Ti_3C_2.

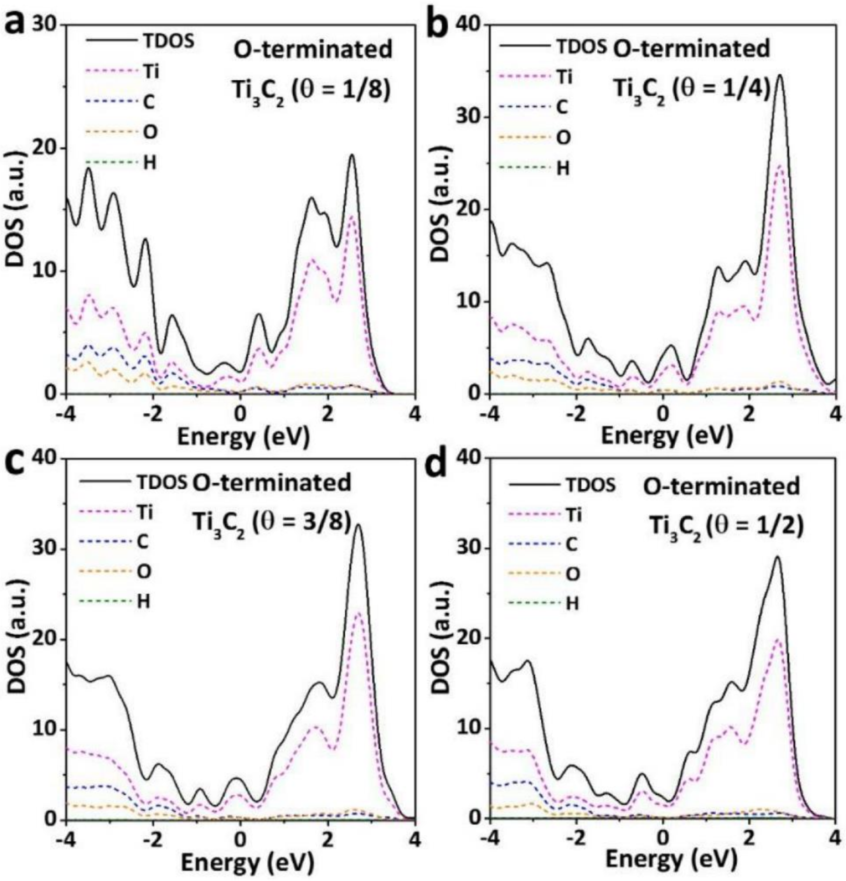

Supplementary Figure 30. The density of states for O-terminated Ti_3C_2 at H coverages (θ) of (**a**) 1/8 , (**b**) 1/4, (**c**) 3/8 and (**d**) 1/2.

Supplementary Tables

Supplementary Table 1. The H adsorption energy (ΔG_{H*}) on O-terminated Ti_3C_2 at different H* coverages.

H* coverage θ	H adsorption energy ΔG_{H*} (eV)
1/8	-0.316
1/4	-0.254
3/8	0.0468
1/2	-0.00283
5/8	0.470
3/4	0.527

Supplementary Table 2. Physicochemical Properties of CT0, CT0.05, CT0.1, CT2.5, CT5 and CT7.5.

Samples	Ti_3C_2 (wt.%) (ICP-AES)	S_{BET} (m^2 g^{-1})	PV[a] (cm^3 g^{-1})	ACS[b] (nm)	H_2 production rate (μmol h^{-1} g^{-1})
CT0	0	3.8	0.01	53	105
CT0.05	0.03	4.2	0.01	54	993
CT0.1	0.09	7.1	0.02	55	1278
CT2.5	1.89	7.2	0.02	52	14342
CT5	4.13	3.8	0.01	55	3377
CT7.5	6.79	3.7	0.01	49	2707

[a] PV: Pore volume, [b] ACS: Average crystallite size.

Supplementary Table 3. Comparison of the photocatalytic H_2-production activities for the representative binary CdS-based photocatalysts loaded with different non-noble metal co-catalysts.

Photocatalyst	*Amount of photocatalyst (mg)*	*Co-catalyst*	*Loading method*	*Optimum loading*	*Enhancement factor*	*Photocatalytic H_2-production activity (μmol h^{-1} g^{-1})*	*Apparent quantum efficiency*	*Reference*
CT2.5	20	Ti_3C_2 NPs	Hydrothermal	2.5 wt.%	136.6	14,342	40.1% at 420 nm	This work
Ni/CdS	100	Ni	Solution mixing	4 wt.%	N/A	25,848	26.8% at 420 nm	[1]
NiO_x/CdS	100	NiO_x	Photo-deposition	1 mol.%	117	5,908	N/A	[2]
$Ni(OH)_2$/CdS	50	$Ni(OH)_2$	Liquid precipitation	23 mol.%	145	5,084	28% at 420 nm	[3]
NiS/CdS	50	NiS	Hydrothermal	5 mol.%	20.6	1,131	N/A	[4]
Ni_2P/CdS	1	Ni_2P	Grinding	5 wt.%	N/A	143,600	14.3% at 420 nm	[5]
Co_3O_4/CdS	50	Co_3O_4	Hydrothermal	3 mol.%	33	236	N/A	[6]
CoP/CdS	1	CoP	Grinding	5 wt.%	N/A	254,000	25.1% at 420 nm	[5]
Graphene oxide/CdS	100	Graphene oxide	Electrostatic assembly	5 wt.%	1.3	3,140	4.8% at 420 nm	[7]
Carbon nanotube/CdS	100	Carbon nanotube	Hydrothermal	3 wt.%	3.7	520	N/A	[8]
MoS_2/CdS	50	MoS_2	Solvothermal	2.5 mol.%	N/A	11,026	31.8% at 420 nm	[9]
WS_2/CdS	10	WS_2	Hot-injection	11 mol.%	16.7	1,984	N/A	[10]

Supplementary Table 4. BET surface area and pore volume of Ti_3C_2-E, Ti_3C_2-5000, Ti_3C_2 NPs, and HT-Ti_3C_2 NPs.

Samples	BET surface area (m^2 g^{-1})	Pore volume (cm^3 g^{-1})
Ti_3C_2-E	39.6	0.08
Ti_3C_2-5000	61.6	0.11
Ti_3C_2 NPs	120.1	0.20
HT-Ti_3C_2 NPs	56.7	0.10

Supplementary Notes

Supplementary Note 1. Analysis of the XRD patterns of Ti_3AlC_2, Ti_3C_2-E and Ti_3C_2 NPs

As shown in Supplementary Fig. 7, the XRD patterns of Ti_3AlC_2, Ti_3C_2-E and Ti_3C_2 NPs are consistent with the literature[11,12]. After ultra-sonication treatment, Ti_3C_2 NPs show a decrease in the intensities of (002) and (004) peaks, in agreement with the dimension change from 3D Ti_3C_2-E to 0D Ti_3C_2 NPs.

Supplementary Note 2. Analysis of the morphology and chemical composition of Pt-CdS

The EDX elemental mapping images of Cd, S and Pt (Supplementary Fig. 14b-d) are consistent with the HAADF image of Pt-CdS (Supplementary Fig. 14a), indicating that Pt is homogeneously dispersed on the surface of CdS. However, no obvious Pt NPs are observed on the surface of CdS in both TEM and HRTEM images (Supplementary Fig. 14e and f), suggesting that Pt is decorated on CdS in the form of ultra-small clusters. Moreover, the petal-like assembly of CdS NPs (Supplementary Fig. 14e) is due to the disassembly of the CdS SMSs (Supplementary Fig. 12a and b). This disassembly is caused by the deposition of a Pt layer on the surface of the CdS NPs, which consequently weakens the combination between CdS NPs.

Supplementary Note 3. Explanation of the hydrogen adsorption energy (ΔG_{H^*}) change on Ti_3C_2

In general, the change in ΔG_{H^*} is continuous from one coverage to the next. In this work, O terminations on both the top and bottom sides of Ti_3C_2 can function as the active sites for HER. The ΔG_{H^*} at $\theta = 3/8$ refers to the free energy of the second H adsorbing on the top side of the 2×2×1 O-terminated Ti_3C_2 model. The ΔG_{H^*} at $\theta = 1/2$ refers to the free energy of the second H adsorbing on the bottom side of the 2×2×1 O-terminated Ti_3C_2 model. Both of them refer to the 1/2 H surface coverage. However, at $\theta = 1/2$ (two H on both the top and bottom sides, respectively), the adsorption system possesses higher symmetry, which decreases the H binding energy. Therefore, $|\Delta G_{H^*}|$ ($\theta = 1/2$) < $|\Delta G_{H^*}|$ ($\theta = 3/8$) as shown in Supplementary Table 1.

Supplementary Note 4. Confirmation of the electron transfer from CdS to Ti_3C_2 in CT2.5

The Mott-Schottky plot (Supplementary Fig. 17a) suggests that the flat band potential of CT0 (pure CdS) is -1.53 V *vs.* Ag/AgCl, which corresponds to -0.91 V *vs.* SHE. Thus, the Fermi level of pure CdS is near -0.91 V *vs.* SHE. On the other hand, the Fermi level of O-terminated Ti_3C_2 is calculated to be 1.88 V *vs.* SHE. Hence, the electrons should migrate from CdS to Ti_3C_2 upon their combination. This is evidenced by the more positive flat band potential of CT2.5 (-0.79 V *vs.* SHE) compared with that of CT0, suggesting the Fermi level of CdS in CT2.5 is lowered after its combination with Ti_3C_2. Thus, this result supports the electron transfer from CdS to Ti_3C_2 in CT2.5.

Supplementary Note 5. Discussion of the morphology and photocatalytic activity of Pt-CdS-1

The TEM image (Supplementary Fig. 27a) shows that the sizes of Pt NPs synthesized by the chemical-reduction method are in the range of 2-10 nm. Further observation on their HRTEM image (Supplementary Fig. 27b) indicates that Pt NPs exhibit the lattice spacings of 0.20 nm, corresponding to the (200) plane of face-centered cubic structured Pt (JCPDS No.04-0802). After loading 2.5 wt% Pt NPs on CdS SMSs, Pt-CdS-1 exhibits the similar morphology with that of CT2.5, except that Pt NPs instead of Ti_3C_2 NPs are loaded on the surface of CdS SMS (Supplementary Fig. 25a). The HRTEM image of Pt-CdS-1 (Supplementary Fig. 25b) shows the lattice spacings of 0.23 and 0.34 nm, in agreement with the (111) plane of face-centered cubic structured Pt and (002) plane of wurtzite-structured CdS, respectively. Hence, the contact between Pt and CdS is established in Pt-CdS-1, implying the possible charge transfer between Pt and CdS. Indeed, Pt-CdS-1 exhibits an obviously enhanced photocatalytic activity of 8234 μmol h^{-1} g^{-1} (Supplementary Fig. 26), compared to that of CT0 (105 μmol h^{-1} g^{-1}). This is attributed to the presence of ultra-small Pt NPs, which not only extract the photo-induced electrons from CdS, but also promote the H_2 evolution, as reported in many previous references.[13-15] Nevertheless, Pt-CdS-1 still exhibits lower photocatalytic activity than CT2.5 (14342 μmol h^{-1} g^{-1}). Given that these two samples show similar morphologies, the superior activity of CT2.5 should mainly arise from the stronger interaction between Ti_3C_2 NP and CdS SMS formed in the hydrothermal reaction, compared to that between Pt NP and CdS SMS. This encouraging result demonstrates the great potential of Ti_3C_2 NP as a highly-active and economical substitute for Pt.

Supplementary Note 6. Analysis of the phase structures and optical properties of CN and CNT2.5

CT2.5, CN and CNT2.5 show almost the same XRD patterns (Supplementary Fig. 21b), which are consistent with the hexagonal wurtzite-structured CdS phase (JCPDS No. 77-2306). Moreover, the absorption edges of CN and CNT2.5 exhibit no apparent shift as compared with CT2.5 (Supplementary Fig. 21c), suggesting that Ni^{2+} is not doped into crystal structure of CdS in CN and CNT2.5. In fact, NiS is only loaded on the surface of CdS in these two samples.

Supplementary Note 7. Analysis of the phase structures and optical properties of ZCS and ZCS/Ti_3C_2

The XRD peaks of both ZCS and ZCS/Ti_3C_2 (Supplementary Fig. 23b) are clearly shifted to the left in comparison to standard cubic sphalerite-structured ZnS (JCPDS No. 05-0566), arising from the formation of $Zn_xCd_{1-x}S$ solid solution. After mixing with 1 wt.% Ti_3C_2 NPs, ZCS/Ti_3C_2 exhibits no obvious change in the XRD pattern compared to that of ZCS, due to the very low loading content (1 wt.%) of Ti_3C_2 NPs. Nevertheless, the UV-Vis diffuse reflectance spectrum of ZCS/Ti_3C_2 (Supplementary Fig. 23c) displays a significant increase in the 510-800 nm region compared with that of ZCS, due to the presence of black Ti_3C_2 NPs. Besides, the color of ZCS/Ti_3C_2 is also changed to olive from the yellow color of ZCS. The results clearly indicate the successful deposition of Ti_3C_2 NPs on ZCS in ZCS/Ti_3C_2.

Supplementary Note 8. Analysis of the phase structures and optical properties of ZnS and ZnS/Ti_3C_2

The cubic sphalerite-structured ZnS (JCPDS No. 05-0566) is observed for both ZnS and ZnS/Ti_3C_2 as shown in the XRD patterns (Supplementary Fig. 24b). Moreover, ZnS/Ti_3C_2 shows almost the same XRD pattern as that of ZnS, since the mechanical mixing of 1 wt.% Ti_3C_2 NPs with ZnS does not change its crystal structure. However, an obvious enhanced absorption in the 370-800 nm region is observed for the UV-Vis diffuse reflectance spectrum of ZnS/Ti_3C_2, in comparison to that of ZnS (Supplementary Fig. 24c). Also, the color of ZnS/Ti_3C_2 turned grey due to the loading of black-colored Ti_3C_2 NPs on the surface of white ZnS.

Supplementary Note 9. Discussion of the effect of F/O atomic ratio on photocatalytic activity

The surface F signal in CT0.05, CT0.1, CT5, CT7.5, CT2.5-E or CT2.5-5000 is negligible as examined by the XPS technique (Supplementary Fig. 28), indicating most of the F terminations on Ti_3C_2 in these samples were replaced by O or OH terminations during the hydrothermal reaction. Hence, the F/O atomic ratio on Ti_3C_2 should be zero in these samples. This result indicates that the H_2 evolution capacity and Fermi level position of Ti_3C_2 are optimized in these samples to boost their photocatalytic activities. Furthermore, this result excludes the influence of F/O ratio variation on the activity differences among these samples and CT2.5.

Supplementary Note 10. Analysis of the surface Pourbaix diagram of Ti_3C_2

At U_{SHE} = 0 V, the most stable state of Ti_3C_2 is terminated by 1/2 ML OH* and 1/2 ML O* (Supplementary Fig. 29a). As the pH decreases, the O* is combined with H^+ to form OH*. Under visible-light irradiation, the photo-induced electrons are supposed to transfer from CdS to Ti_3C_2 and further to the -OH terminations, where the adsorbed H^+ is reduced to evolve H_2 gas, again forming -O terminations. Based on the Pourbaix diagram (Supplementary Fig. 29b), the most stable termination of Ti_3C_2 is a mix of OH* and O*, which proves that our model for free energy calculation is reasonable.

Supplementary Note 11. Confirmation of the excellent conductivity of O-terminated Ti_3C_2 at different H coverages

As displayed in Supplementary Fig. 30a-d, continuous electronic states cross the Fermi level at all four H coverages, indicating that the conductivity of O-terminated Ti_3C_2 is excellent at all four H coverages.

Supplementary Methods

Experimental Section

Synthesis of Ti_3AlC_2. Elemental Ti (Alfa Aesar, Ward Hill, USA, 99 wt.% purity, particle size < 40 μm), Al (Alfa Aesar, Ward Hill, USA, 99 wt.% purity, particle size < 40 μm), and graphite (Alfa Aesar, Ward Hill, USA, 99 wt.% purity, particle size < 48 μm) powders were mixed with a molar ratio of 3 : 1.5 : 2. The mixture was ball-milled for 48 hours and cold pressed into cylindrical discs (15 mm in diameter and 10 mm in height) under 1 GPa pressure. The discs were put into a tube furnace under flowing Ar gas and heated to 1673 K for 2 hours at a ramp rate of 20 K min^{-1}. After cooling to room temperature, the discs were ball-milled for 2 hours to acquire fine powders for further investigation.

Synthesis of Ti_3C_2-E. Ti_3C_2-E was prepared by immersing Ti_3AlC_2 in 49% HF (Aladdin Reagent, China) at 333 k for 20 hours. All Al species in Ti_3AlC_2 were selectively removed by HF etching, while OH^-, O^- and/or F^- replaced Al as the terminal groups. The as-prepared sample was washed repeatedly with de-ionized water, centrifugally separated and dried in vacuum at 343 K for 8 hours.

Synthesis of Ti_3C_2 NPs. 100 mg of Ti_3C_2-E was added into 100 ml of de-ionized water and subjected to ultra-sonication for 5 hours, followed by centrifugation at 10000 RPM. After removal of the precipitates, a homogeneous dispersion of Ti_3C_2 NPs in the supernatant was obtained. The concentration of the obtained Ti_3C_2 NPs in aqueous solution was determined to be 0.15 mg ml^{-1}.

Synthesis of CdS/Ti_3C_2 composites. 0.368 g of $Cd(Ac)_2$ was firstly dissolved in de-ionized water after stirring. Then, a certain amount of Ti_3C_2 NPs in aqueous solution was added into the above solution under vigorous stirring. After 1 hour stirring, 0.42 g of thiourea was added into the suspension and stirred for 2 hours. Then the above suspension was transferred into a 50 ml autoclave and kept at 180 °C for 12 h. The obtained samples were washed twice with deionized water and ethanol, respectively, and dried at 333 K for 10 hours. The mass ratios of Ti_3C_2 to CdS were 0, 0.05, 0.1, 2.5, 5 and 7.5 wt%, and the resulting samples were labeled as CT0, CT0.05, CT0.1, CT2.5, CT5, and CT7.5, respectively.

Synthesis of Pt NPs. 7.5 ml of 0.1 M CTAB aqueous solution was dissolved in warm water, followed by adding 2.5 ml of 1 mM H_2PtCl_6 aqueous solution and 0.6 ml of 10 mM $NaBH_4$ aqueous solution under vigorous stirring. Then the above solution was transfered to oil bath at 120 °C. After stirring for 15 min, the synthesized products were cooled down to room temperature, centrifuged to remove the redundant CTAB in the aqueous solution and stored in fridge. The concentration of the Pt NPs was determined by thermogravimetric analysis.

Synthesis of CNT2.5. 0.368 g of $Cd(Ac)_2$ and 0.003 g of $Ni(Ac)_2$ were firstly dissolved in deionized water after stirring. Subsequently, a certain amount of Ti_3C_2 NPs in aqueous solution was added into the above solution under vigorous stirring. After 1 hour of stirring, 0.42 g of thiourea was added into the suspension and stirred for 2 hours. Then the above suspension was transferred into a 50 ml autoclave and kept at 180 °C for 12 h. The as-prepared sample was washed twice by deionized water and ethanol, respectively, and then dried at 333 K for 10 hours.

Synthesis of ZnS. 0.633 g of $Zn(Ac)_2 \cdot 2H_2O$ was added into 31 ml of deionized water and 5 ml of 0.9 M Na_2S aqueous solution was then added dropwise into this suspension followed by stirring for 6 h at room temperature. The resulting suspension was then transferred into a 50 ml autoclave and maintained at 180 °C for 12 h. The acquired sample was washed twice with deionized water and ethanol, respectively, and then dried at 333 K for 10 hours.

Computation Section

Active sites and H adsorption properties. The differential Gibbs free energy of the adsorption of atomic H ($\Delta G^0_{H^*}$) is obtained by Eq (1):

$$\Delta G^0_{H^*} = \Delta E_H + \Delta E_{ZPE} - T\Delta S_H \tag{1}$$

where ΔE_{ZPE} and ΔS_H are the changes in the zero point energy and entropy between H adsorption and H_2 in the gas phase, respectively. The contributions from the catalysts to both ΔE_{ZPE} and ΔS_H are considered negligible. Therefore, ΔE_{ZPE} is obtained by Eq (2)[16]:

$$\Delta E_{ZPE} = E^{nH}_{ZPE} - E^{(n-1)H}_{ZPE} - {}^{1}\!/_{2}\, E^{H_2}_{ZPE} \tag{2}$$

where E^{nH}_{ZPE} is the zero point energy of n-adsorbed H atoms on the catalyst without the contribution of catalyst and $E^{H_2}_{ZPE}$ is the zero point energy of H_2 in gas phase. The vibration frequency of H adsorption on Ti_3C_2, O-terminated Ti_3C_2 or F-terminated Ti_3C_2 at 1/8 coverage is 3705.0 cm^{-1}, and not sensitive to the coverages. The calculated frequency of H_2 gas is 4289.4 cm^{-1}. ΔS_H is obtained by Eq (3):

$$\Delta S_H \cong -{}^{1}\!/_{2}\, S^0_{H_2} \tag{3}$$

where $S^0_{H_2}$ is the entropy of H_2 gas at standard conditions.

Therefore, Eq (1) can be rewritten as Eq (4):

$$\Delta G^0_{H^*} = \Delta E_H + 0.30\ \text{eV} \tag{4}$$

where ΔE_H is the differential H adsorption energy, which is defined by Eq (5):

$$\Delta E_H = E_{nH*} - E_{(n-1)H*} - {}^{1}\!/_{2}\, E_{H_2} \tag{5}$$

where * denotes the catalyst. E_{nH*}, $E_{(n-1)H*}$ and E_{H_2} represent the total energies of catalyst with n adsorbed H atoms, total energies of catalyst plus (n-1) adsorbed H atoms and H_2 gas, respectively.

Fermi level positions. The LVTOT in VASP is firstly applied to obtain the Fermi Level *vs.* vacuum level and the Fermi level *vs.* SHE is then calculated using the following Eq (6):

$$E_F(\textit{vs.}\ \text{SHE}) = -4.44\ \text{V} - E_F(\textit{vs.}\ \text{vaccum level}) \tag{6}$$

Surface Pourbaix Diagrams. The surface Pourbaix diagrams of Ti_3C_2 were constructed by plotting the most stable state of the surface under relevant U_{SHE} and pH. In our model, we assumed that the oxidation of water to OH* and O* on Ti_3C_2 through the following steps as suggested by reference[17]:

$$H_2O + * \rightarrow OH^* + H^+ + e^- \tag{7}$$

$$OH^* \rightarrow O^* + H^+ + e^- \tag{8}$$

Under standard conditions, the free energy of $H^+ + e^-$ is equal to ½ H_2. Therefore, Eq (7) and Eq (8) can be rewritten into Eq (9) and Eq (10):

$$H_2O + * \rightarrow OH^* + \frac{1}{2} H_2 \tag{9}$$

$$OH^* \rightarrow O^* + \frac{1}{2} H_2 \tag{10}$$

The Gibbs free-energies of Eq (9) ($\Delta G^0_{OH^*}$) and Eq (10) ($\Delta G^0_{O^*}$) are obtained by Eq (11):

$$\Delta G^0 = \Delta E + \Delta E_{ZPE} - T\Delta S \tag{11}$$

Where, ΔE is the energy difference of Eq (9) or Eq (10). The values for ΔE_{ZPE}-$T\Delta S$ are calculated from the value table I of reference[18].

Both Eq (7) and Eq (8) are dependent on the pH and potential U through the chemical potential of H^+ and e^-, respectively, while Eq (9) and Eq (10) are not. To include the effects of pH and potential U, the Eq(11) are rewritten into Eq (12) and Eq (13):

$$\Delta G_{OH^*} = \Delta G^0_{OH^*} - eU_{SHE} - k_b T \ln 10 \times pH \tag{12}$$

$$\Delta G_{O^*} = \Delta G^0_{O^*} - eU_{SHE} - k_b T \ln 10 \times pH \tag{13}$$

Based on Eq (12) and Eq (13), we can calculate the free energy of Ti_3C_2 with different coverages of OH* and O* terminations under different conditions. The free energy of Ti_3C_2 with mixture terminations ($Ti_3C_2(OH)_x(O)_y$, $x + y \leq 2$) are obtained by Eq (14):

$$\Delta G_{mix} = \Delta G^0_{mix} - (x + 2y)U_{SHE} - (x + 2y)k_b T \ln 10 \times pH \tag{14}$$

Therefore, we can obtain the free energy of Ti_3C_2 under different OH* and O* coverages. The most stable state of the surface under relevant conditions is used to construct the surface Pourbaix diagrams.

Supplementary References

1. Wang, H. *et al.* Nickel nanoparticles modified CdS - A potential photocatalyst for hydrogen production through water splitting under visible light irradiation. *Int. J. Hydrogen Energy* **40,** 340-345 (2015).
2. Chen, X. *et al.* In situ photodeposition of NiO_x on CdS for hydrogen production under visible light: Enhanced activity by controlling solution environment. *Appl. Catal. B-Environ.* **152-153,** 68-72 (2014).
3. Ran, J., Yu, J. & Jaroniec, M. $Ni(OH)_2$ modified CdS nanorods for highly efficient visible-light-driven photocatalytic H_2 generation. *Green Chem.* **13**, 2708-2713 (2011).
4. Zhang, J., Qiao, S. Z., Qi, L. & Yu, J. Fabrication of NiS modified CdS nanorod p-n junction photocatalysts with enhanced visible-light photocatalytic H_2-production activity. *Phys. Chem. Chem. Phys.* **15,** 12088-12094 (2013).
5. Cao, S. *et al.* Spectacular photocatalytic hydrogen evolution using metal-phosphide/CdS hybrid catalysts under sunlight irradiation. *Chem. Commun.* **51,** 8708-8711 (2015).
6. Yuan, J. *et al.* Amorphous Co_3O_4 modified CdS nanorods with enhanced visible-light photocatalytic H_2-production activity. *Dalton Trans.* **44,** 1680-1689 (2015).
7. Peng, T. *et al.* Enhanced photocatalytic hydrogen production over graphene oxide-cadmium sulfide nanocomposite under visible light irradiation. *J. Phys. Chem. C* **116,** 22720-22726 (2012).
8. Ye, A. *et al.* CdS-graphene and CdS-CNT nanocomposites as visible-light photocatalysts for hydrogen evolution and organic dye degradation. *Catal. Sci. Technol.* **2,** 969-978 (2012).
9. Lang, D., Shen, T. & Xiang, Q. Roles of MoS_2 and graphene as cocatalysts in the enhanced visible-light photocatalytic H_2 production activity of multiarmed CdS nanorods. *ChemCatChem* **7,** 943-951 (2015).
10. Chen, J. *et al.* One-pot synthesis of CdS nanocrystals hybridized with single-layer transition-metal dichalcogenide nanosheets for efficient photocatalytic hydrogen evolution. *Angew. Chem. Int. Ed.* **54,** 1210-1214 (2015).
11. Naguib, M. *et al.* Two-dimensional nanocrystals produced by exfoliation of Ti_3AlC_2. *Adv. Mater.* **23,** 4248-4253 (2011).
12. Yan, P. *et al.* Enhanced supercapacitive performance of delaminated two-dimensional titanium

carbide/carbon nanotube composites in alkaline electrolyte. *J. Power Sources* **284,** 38-43 (2015).

13. Bao, N., Shen, L., Takata, T. & Domen, K. Self-templated synthesis of nanoporous CdS nanostructures for highly efficient photocatalytic hydrogen production under visible light. *Chem. Mater.* **20,** 110-117 (2008).
14. Darwent, J. R. & Porter, G. Photochemical hydrogen production using cadmium sulphide suspensions in aerated water. *J. Chem. Soc., Chem. Commun.* 145-146 (1981).
15. Yan, H. *et al.* Visible-light-driven hydrogen production with extremely high quantum efficiency on Pt-PdS/CdS photocatalyst. *J. Catal.* **266**, 165-168 (2009).
16. Tsai, C., Abild-Pedersen, F. & Nørskov, J. K. Tuning the MoS_2 edge-site activity for hydrogen evolution via support interactions. *Nano Lett.* **14**, 1381-1387 (2014).
17. Hansen, H. A., Rossmeisl, J. & Norskov, J. K., Surface Pourbaix diagrams and oxygen reduction activity of Pt, Ag and Ni(111) surfaces studied by DFT. *Phys. Chem. Chem. Phys.* **10,** 3722-3730 (2008).
18. Valdés, Á. *et al.* Oxidation and photo-oxidation of water on TiO_2 surface. *J. Phys. Chem. C* **112,** 9872-9879 (2008).

Chapter 6: Superior Electron-Extracting Capacity of Ti_3C_2 MXene on $Zn_{0.5}Cd_{0.5}S$ towards Highly-Efficient Solar H_2 Production

6.1 Introduction and Significance

Hydrogen evolution from water splitting by photocatalysis, particularly under visible-light illumination, has been the focus of extensive research because of its potential applications in green and renewable energy. The insightful mechanism of the strong electronic coupling between photocatalyst and co-catalyst can instruct the further enhancement of the photocatalytic H_2-production performance. In this chapter, we have revealed the superior electron-extracting competence of Ti_3C_2 MXene on $Zn_{0.5}Cd_{0.5}S$ via state-of-art characterization techniques and theoretical computations, which plays a pivotal role in improving the photocatalytic H_2-production activity. The highlights of this work include:

- We for the first time fabricated a novel Ti_3C_2 MXene loaded $Zn_{0.5}Cd_{0.5}S$ sub-microsphere composite photocatalyst by a facile hydrothermal approach.
- The $Ti_3C_2/Zn_{0.5}Cd_{0.5}S$ composite exhibits the highest visible-light photocatalytic H_2-production activity of 7196 $\mu mol\ h^{-1}\ g^{-1}$ at the optimal loading of 4 wt.%, corresponding to a quantum efficiency of 25.4% at 420 nm.
- This extraordinary photocatalytic performance is attributed to the superior electron-accepting ability of Ti_3C_2 MXene, as evidenced by a series of advanced characterization methods and density function theory (DFT) calculations.

6.2 Superior Electron-Extracting Capacity of Ti_3C_2 MXene on $Zn_{0.5}Cd_{0.5}S$ towards Enhanced Visible-Light Photocatalytic H_2 Production

This chapter is included in this thesis as it appears as a research paper submitted by **Jingrun Ran** and Shi-Zhang Qiao, Superior Electron-Extracting Capacity of Ti_3C_2 MXene on $Zn_{0.5}Cd_{0.5}S$ towards Enhanced Visible-Light Photocatalytic H_2 Production, to ***Small***.

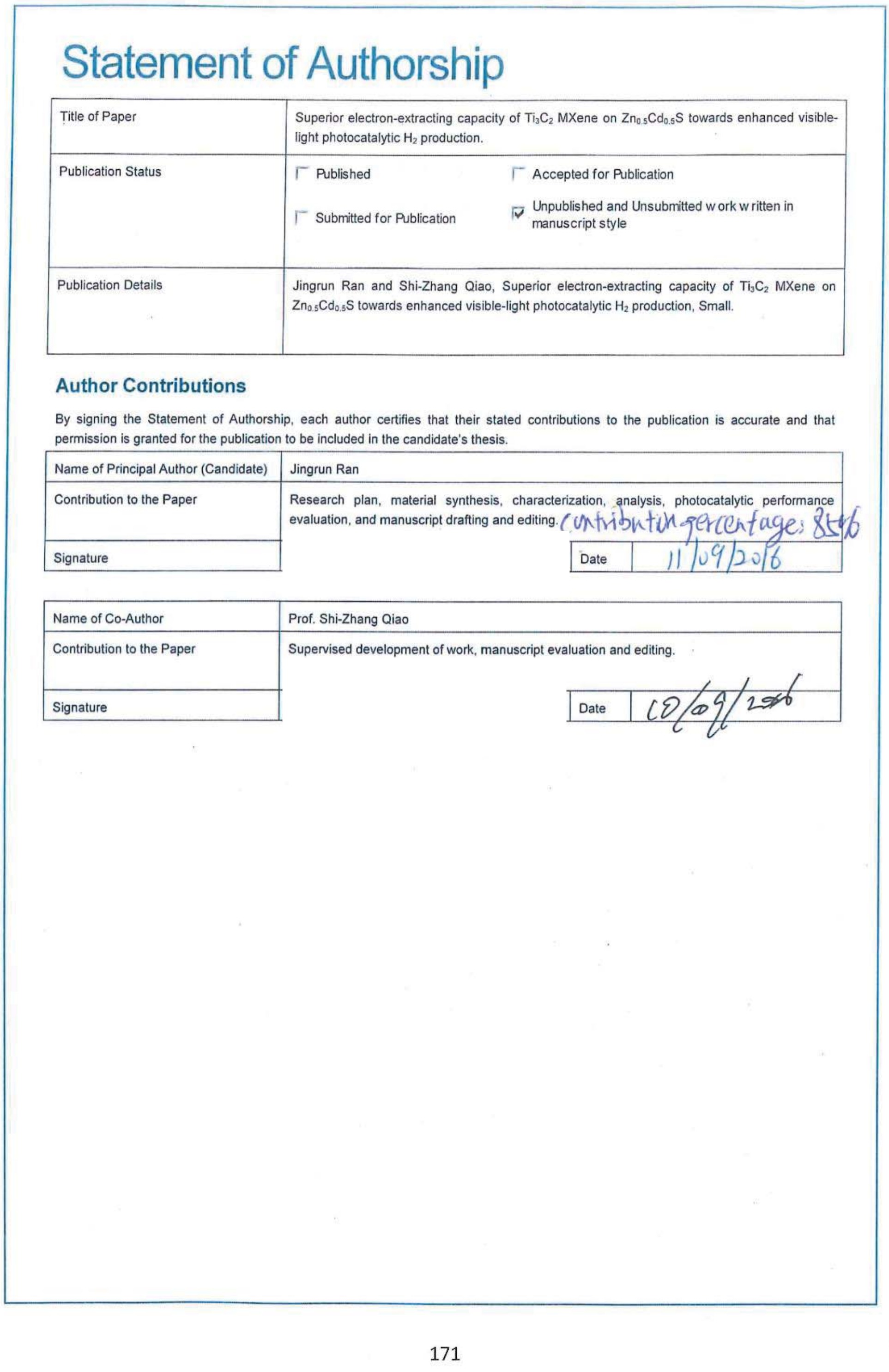

Statement of Authorship

Title of Paper	Superior electron-extracting capacity of Ti_3C_2 MXene on $Zn_{0.5}Cd_{0.5}S$ towards enhanced visible-light photocatalytic H_2 production.
Publication Status	☐ Published ☐ Accepted for Publication ☐ Submitted for Publication ☑ Unpublished and Unsubmitted work written in manuscript style
Publication Details	Jingrun Ran and Shi-Zhang Qiao, Superior electron-extracting capacity of Ti_3C_2 MXene on $Zn_{0.5}Cd_{0.5}S$ towards enhanced visible-light photocatalytic H_2 production, Small.

Author Contributions

By signing the Statement of Authorship, each author certifies that their stated contributions to the publication is accurate and that permission is granted for the publication to be included in the candidate's thesis.

Name of Principal Author (Candidate)	Jingrun Ran
Contribution to the Paper	Research plan, material synthesis, characterization, analysis, photocatalytic performance evaluation, and manuscript drafting and editing. contribution percentage: 85%
Signature	Date 11/09/2016

Name of Co-Author	Prof. Shi-Zhang Qiao
Contribution to the Paper	Supervised development of work, manuscript evaluation and editing.
Signature	Date 10/09/2016

DOI: 10.1002/((please add manuscript number))
Article type: Communication

Superior electron-extracting capacity of Ti_3C_2 MXene on $Zn_{0.5}Cd_{0.5}S$ towards highly-efficient visible-light photocatalytic H_2 production

*Jingrun Ran and Shi Zhang Qiao**

J. Ran, Prof. S. Z. Qiao
School of Chemical Engineering
The University of Adelaide, Adelaide, SA 5005, Australia
E-mail: s.qiao@adelaide.edu.au

Keywords: photocatalytic water splitting, co-catalyst, Ti_3C_2 MXene, $Zn_{0.5}Cd_{0.5}S$

Photocatalytic hydrogen (H_2) production from water splitting under visible-light illumination is regarded as an attractive route to resolve the aggravating worldwide energy problems. In this work, highly-efficient photocatalytic H_2 production is achieved by loading Ti_3C_2 nano-particles on $Zn_{0.5}Cd_{0.5}S$ sub-microspheres by a simple hydrothermal method. At the optimal loading of 4 wt.%, the $Ti_3C_2/Zn_{0.5}Cd_{0.5}S$ composite exhibits the highest photocatalytic H_2-production activity of 7196 μmol h^{-1} g^{-1}, exceeding that of bare $Zn_{0.5}Cd_{0.5}S$ by 85.7 times, corresponding to a quantum efficiency of 25.4% at 420 nm. This high photocatalytic H_2-production performance is attributed to the strong electron-extracting competence of Ti_3C_2 MXene, as evidenced by both experimental technique and theoretical computations. This study not only demonstrates the huge potential of Ti_3C_2 MXene as a replacement of noble-metal co-catalyst, but, more importantly, revealing the mechanistic insight of the interfacial charge transfer in Ti_3C_2-incorporated photocatalyst systems.

Hydrogen production via photocatalytic water splitting is a promising technique for the direct conversion of solar energy into storable chemical energy.[1,2] The chemical energy can then be utilized by, *e.g.* fuel cell with high efficiency, producing water as the sole product. Such a cycle lays a foundation for the energy paradigm known as the "hydrogen economy", a sustainable and environmental-friendly substitute to the current practice based on fossil fuel combustion.[2] Ever since the pioneering report by Fujishima and Honda on photo-electrochemical water splitting on a titania electrode,[3] numerous photocatalysts, *e.g.* oxides, (oxy)nitrides, and (oxy)sulfides, have been developed for solar hydrogen production.[2,4] Nevertheless, none of these materials meet the demands for commercial application, mainly due to their high cost, low activity and poor stability. One powerful and universal strategy is to load co-catalysts on the surface of photocatalysts to greatly enhance their performance, via promoting the separation and transfer of photo-induced electron-hole pairs and accommodating catalytic active sites.[1,5-8]

To realize the outstanding enhancement of photocatalytic activity by loading co-catalyst, the formation of strong electronic coupling between co-catalyst and photocatalyst is of great significance. However, the insightful understanding of the electronic coupling between co-catalyst and photocatalyst at the atomic level is still missing.[1] On the other hand, the most active co-catalyst, Pt, which can tremendously promote the photocatalytic H_2 production, suffers from high price and low abundance.[1,2,4,5] Furthermore, the other co-catalysts comprising earth-abundant elements still exhibit insufficient activity and stability.[1] Hence, it is of great significance to develop a highly-active, low-cost and robust co-catalyst for photocatalytic H_2 production. MXene, an emerging family of over 60 two-dimensional (2D) metal carbides, nitrides or carbonitrides, exhibits many unique properties, *e.g.* high electric conductivity, large surface area, abundant hydrophilic functionalities, and potential catalytic activity.[9-11] These exceptional abilities of MXene render it an excellent co-catalyst candidate.

In this work, we for the first time report the excellent electron-extracting capability of Ti_3C_2 MXene on $Zn_{0.5}Cd_{0.5}S$ (ZCS). By combining experimental and theoretical techniques, the intimate electronic coupling between ZCS and Ti_3C_2 was revealed, which leads to an obvious increase of photocatalytic H_2-production activity by a factor of 85.7, reaching 7196 μmol h^{-1} g^{-}

[1]. This study highlights the pivotal role of the exceptional electron extracting capacity of Ti_3C_2 MXene on boosting the photocatalytic H_2-production performance of ZCS.

Our previous studies indicated that ZCS solid solution with x = 0.5 shows the best photocatalytic H_2-roduction activity under visible-light irradiation. Hence, we chose this composition in the current work. The Ti_3C_2/ZCS composites were synthesized by an easy and green one-pot hydrothermal method. Firstly, $Zn(Ac)_2$ and $Cd(Ac)_2$ were dissolved into de-ionized water after stirring. Subsequently, Ti_3C_2 nano-particles (NPs) dispersion was added into the above solution under vigorous stirring. Then thiourea was added into the above suspension followed by constant stirring. After hydrothermal treatment at 160 °C for 12 h, the Ti_3C_2/ZCS composites were finally fabricated. The mass ratios of Ti_3C_2 to ZCS were 0, 1, 2, 4 and 10 wt%, and the resulting samples were labeled as T0, T1, T2, T4 and T10, respectively.

As shown in Figure 1, pure ZCS (T0) exhibits a very low photocatalytic activity of 84 μmol h^{-1} g^{-1}, due to the fast recombination of photo-induced electron-hole pairs and lack of catalytic active sites.[12,13] The integration of Ti_3C_2 NPs with ZCS leads to apparently enhanced photocatalytic activity. The optimal loading of Ti_3C_2 NPs was 4 wt.%, which results in the highest photocatalytic activity of 7196 μmol h^{-1} g^{-1}, exceeding that of T0 by 85.7 times. This value is even higher than that of 4 wt.% Pt loaded ZCS (Pt-T0), suggesting that Ti_3C_2 NP is a high-performance and low-priced substitute for rare and expensive Pt. Meanwhile, a high apparent quantum efficiency (QE) of 25.4% at 420 nm was also observed on T4. To compare Ti_3C_2 NPs with other earth-abundant co-catalysts, 4 wt.% Ni, NiS or MoS_2 loaded ZCS were prepared, which present inferior photocatalytic H_2-production activities of 3380, 4708 and 3020 μmol h^{-1} g^{-1}, respectively. These results indicate that Ti_3C_2 NPs rank among one of the most efficient noble-metal-free co-catalysts. Furthermore, T4 doesn't show any obvious decrease of activity after photocatalytic reaction for 9 h (Figure S1), confirming its excellent stability.

To disclose the origin of the enormous increase in photocatalytic activity of T4, both experimental techniques and theoretical computations were employed. As displayed in Figure S2, the XRD patterns of all the samples are clearly shifted to the right compared with standard hexagonal wurtzite-structured phase CdS (JCPDS No. 77-2306) due to the formation of ZCS solid solution. Compared with pristine ZCS (T0), no apparent changes of intensties and width of the XRD peaks are observed on T4, indicating that no obvious alteration of phase structures and crystallites is found on T4. Besides, no obvious shift of peak positions is found in T4, implying that neither Ti or C from Ti_3C_2 is doped into the crystal structure of ZCS during the hydrothermal treatment. Furthermore, no diffraction peaks of Ti_3C_2 are found for T4 due to the low loading of Ti_3C_2 in the composite. The similar XRD patterns of T0 and T4 indicate that the great difference in activity is not aroused by any crystal structure change in ZCS.

To investigate the morphology and composition of the optimized T4 sample, transmission electron microscopy (TEM), high-resolution TEM (HRTEM) and energy dispersive X-ray spectra (EDX) and X-ray photoelectron spectroscopy (XPS) techniques are employed. As shown in Figure 2a, a typical TEM image of T4 suggests the sphere-like morphology of T4 with size of *c.a.* 300-400 nm. The HRTEM image in Figure 2b further confirms that the lattice spacing is 0.19 nm, corresponding to the (103) plane of ZCS. Figure 2a shows that Ti_3C_2 NP with size of *ca.* 50 nm is deposited on the surface of the ZCS sub-microsphere (SMS). The EDX spectrum in Figure 2c suggests that T4 contains Zn, Cd, S and Ti elements, confirming the formation of ZCS/Ti_3C_2 composite. The presence of Ti_3C_2 NPs in T4 is further corroborated by the high-resolution XPS spectra of Ti 2p, which are deconvoluted to Ti-C and Ti-O bonding (Figure 2d).[14] Besides, the obviously enhanced light absorption in the range of ~550 to 800 nm also supports the presence of Ti_3C_2 NPs in T4 (see Figure 2f). Moreover, the absence of F signal in Figure 2e indicates that most of the -F terminations are substitued by -OH and/or -O terminations.

It is widely-accepted that the charge seperation and transfer process plays a pivotal role in determining the final efficiency of the photocatalytic process.[15,16] Hence, a series of characterization techniques, such as transient photocurrent (TPC) density measurement, electrochemical impedance spectra (EIS), and surface photovoltage (SPV) spectra were conducted. Figure 3a inset exhibits that ZCS SMS deposited with the optimal amount of Ti_3C_2 NPs (T4) shows much higher TPC density than that of pure ZCS SMS (T0), indicating the importance of Ti_3C_2 NPs in facilitating the charge transfer. Besides, the EIS analysis shows that T4 displays a much smaller semicircle in the middle-frequency region (see Figure 3a), suggesting its much faster interfacial charge transfer, thanks to the presence of Ti_3C_2 NPs. Furthermore, as shown in Figure 3b, the intensity of the SPV response of T4 in the ~400-600 nm region is much stronger than that of T0, also confirming the much higher charge seperation and transport efficiency in T4.

The efficient interfacial charge separation efficiency is further corroborated by the valence-band (VB) XPS spectra. As observed in Figure 3c, T0 and T4 show the edges of the maximum energies at 0.85 and 1.3 eV, respectively, suggesting that Ti_3C_2 loaded on ZCS leads to the positive shift of the valence band maximum energy of ZCS. Considering the similar band gap energy of T0 and T4 (Figure 2f inset), a 0.47 V downward shift of the conduction band (CB) of ZCS is achieved in this twinary composite. Although the downward shift of the CB of ZCS will decrease the reductive capacity of photo-induced electrons, the positive shift of the VB of ZCS will increase the oxidative capacity of photo-induced holes. Besides, the obvious change in the band edge positions also indicates the strong and intimate electronic coupling between ZCS and Ti_3C_2, leading to the extraction of electrons from ZCS to Ti_3C_2. To further reveal the strong electron-extracting capability of Ti_3C_2 NPs, the flat-band potentials of T0 and T4 were measured by Mott-Schottky plots, respectively. As displayed in Figure 3d, the decoration of Ti_3C_2 NPs onto ZCS results in apparent anodic shift from -1.58 V to -1.35 V (*vs.* Ag/AgCl) in the flat-band potential of T4, suggesting that the electron migrate from ZCS to Ti_3C_2 NPs, consistent with the VB XPS spectra results.

The intimate interactions between Ti_3C_2 and ZCS in T4 was further supported by the XPS results. In comparison to T0, the XPS peaks of Zn 2p, Cd 3d and S 2p show a shift to the high binding-energy direction (Figure 4a-c), suggesting the electron diffusion from ZCS to Ti_3C_2 in T4. On the other hand, the Ti 2p peaks in CT2.5 exhibit lower binding energies than those of pure Ti_3C_2 NPs, also indicating the acceptance of electron from ZCS. The above results show the superior electron-extracting ability of Ti_3C_2 NPs upon their loading on the surface of ZCS. DFT calculations were further conducted to elicit the strong electronic coupling between ZCS and Ti_3C_2, The model shown in Figures 4d and 4f mimics the structural environment of ZCS loaded with Ti_3C_2. The differential charge density of the combined relaxed system was calculated. The yellow and green iso-surfaces in Figures 4e and 4g depict the regions of net electron accumulation or deficit on intercalation. Evidently, the surface of Ti_3C_2 attracts electron density from the adjacent CdS.[17]

Apart from the charge separation and tranfer efficiency, the light absorption capacity and surface area are also the two main factors infuencing the final photocatalytic performance.[18] As shown in Figure 2f, the obviously improved absorption in the region of ~550 nm to 800 nm is observed for T4. However, no H_2 gas is detected on T4 when applying a 550 nm light filter to cut off any incident light with a wavelength shorter than 550 nm. This result indicates that the increased photo-absorption from the Ti_3C_2 NPs does not contribute to the enhancement of the photocatalytic performance.

The larger specific surface areas and bigger pore volumes can promote the photocatalytic performance of photocatalysts, since more surface active sites facilitates the adsorption of reactants, and migration of reactants/products through the interconnected porous networks.[19,20] To testify the surface areas and pore volumes of T4 and T0, their N_2 sorption isotherms were investigated. As shown in Figure S8, both T0 and T4 exhibit a type IV N_2 sorption isotherm. Particularly, T4 exhibits an obvious hysterisis loop in the relative pressure range of 0.4-0.8, indicating the presence of many mesopores, arising from the Ti_3C_2 NPs. A much larger surface area (17.0 m^2 g^{-1}) and pore volume (0.003 cm^3 g^{-1}) are observed on T4, resulting from the dispersion of Ti_3C_2 NPs on the surface of ZCS SMS. In contrast, no obvious hysteresis loop is observed for T0 with a much smaller surface area (1.0 m^2 g^{-1}) and pore volume (0.022 cm^3 g^{-1}), due to the large size and non-porous structure of ZCS SMS.

According to the above experimental results, the photocatalytic H_2-production mechanism is proposed for T4. As shown in Figure 4h, under visible-light irradiation ($\lambda > 420$ nm), the electrons in the VB of T4 are excited to its CB, producing photo-induced electrons on the CB of T4 while leaving photo-induced holes on the CB of T4. Then, the photo-induced electrons are extracted from the CB of ZCS to Ti_3C_2 NPs; whilst the photo-induced holes in the VB diffuse to the surface of ZCS. Afterwards, the photo-induced electrons are accumulated in Ti_3C_2 NPs, where the protons are reduced by the electrons to evolve hydrogen gas. Meanwhile, the lactic acid molecules are oxidized by the photo-induced holes. The superior electron-extracting ability of Ti_3C_2 NPs tremendously boost the interfacial charge transfer between CdS and Ti_3C_2, finally leading to the apparently enhanced photocatalytic efficiency.

In conclusion, we for the first time fabricated a Ti_3C_2 modified $Zn_{0.5}Cd_{0.5}S$ composite photocatalyst by a facile hydrothermal approach. The as-synthesized Ti_3C_2 modified $Zn_{0.5}Cd_{0.5}S$ composite exhibts the highest photocatalytic H_2-production activity of 7196 μmol h^{-1} g^{-1} at the optimal loading (4 wt%) of Ti_3C_2. The enhanced photocatalytic H_2-production activity is mainly attributed to the excellent electron-accepting ability of Ti_3C_2 NPs loaded on $Zn_{0.5}Cd_{0.5}S$. Our work not only demonstrates the possibility of using Ti_3C_2 to replace expensive noble-metal co-catalysts in solar H_2 production, but also provides a new insight into the interfacial charge transfer in the Ti_3C_2 modified photocatalyst systems.

Experimental Section

Sample preparation: All the reagents were of analytical grade and were used without further purification. Deionized water was utilized in all experiments. Ti_3AlC_2 (MAX phase: $M_{n+1}AX_n$, in which M denotes early transition metal, A indicates III A or IV A group element, and X stands for C or N) was fabricated using the method by Peng *et al.*[21] Exfoliated Ti_3C_2 (MXene phase) was synthesized by immersing Ti_3AlC_2 in 49% HF (Aladdin Reagent, China) at 60 °C for 20 h. All Al species in Ti_3AlC_2 were selectively etched by HF, whilst OH^-, O^- and/or F^- substituted Al as the terminal groups. The as-synthesized sample was washed repeatedly with de-ionized water, separated by centrifugation and dried in vaccum at 70 °C for 8 h. Ti_3C_2 NPs were prepared by ultra-sonicating exfoliated Ti_3C_2 in de-ionized water. In detail, 100 mg exfoliated Ti_3C_2 was added into 100 ml de-ionized water and ultra-sonicated for 5 hours, followed by centrifuging at 10000 RPM. After abandoning the precipitates, homogeneous Ti_3C_2 NPs dispersion was acquired in the supernatant. The concentration of acquired Ti_3C_2 NPs aqueous solution was found to be 0.15 mg/ml. A facile one-pot hydrothermal approach was employed to prepare the $Ti_3C_2/Zn_{0.5}Cd_{0.5}S$. In a typical synthesis, 0.220 g $Zn(Ac)_2$ and 0.267 g $Cd(Ac)_2$ was firstly dissolved into de-ionized water after stirring. Subsequently, a certain amount of Ti_3C_2 NPs aqueous solution was added into the above solution under vigorous stirring. After 1 h stirring, 0.300 g thiourea was added into the suspension and stirred for 2 h. Then the above suspension was transferred into a 50 ml autoclave and maintained at 160 °C for 12 h. The resultant samples were washed twice by deionized water and ethanol, respectively, and dried at 60 °C for 10 h. The mass ratios of Ti_3C_2 to $Zn_{0.5}Cd_{0.5}S$ were 0, 1, 2, 4 and 10 wt%, and the resulting samples were labeled as T0, T1, T2, T4 and T10, respectively. Pt-T0 was synthesized by *in-situ* photo-deposition of 4 wt.% Pt onto the surface of T0 using H_2PtCl_6 under Xe arc lamp (300 W) irradiation for 40 min. Ni-T0 was synthesized by *in-situ* photo-deposition of 4 wt.% Ni onto the surface of T0 using $Ni(NO_3)_2$ under Xe arc lamp (300 W) irradiation for

40 min. NiS-T0 was prepared by a reported hydrothermal method[22] using T0 as the substrate. MoS_2-T0 was prepared by a reported hydrothermal method[23] using T0 as the substrate.

Characterization: XRD patterns were recorded on an X-ray diffractometer (Miniflex, Rigaku) using Cu Kα radiation at 40 kV and 15 mA. TEM analyses were performed by a JEM-2010F electron microscope (JEOL, Japan) at an acceleration voltage of 200 kV. UV-Vis diffuse reflectance spectra of the samples were acquried for the dry-pressed disk samples on a UV-Vis spectrophotometer (UV2600, Shimadzu, Japan) with $BaSO_4$ as a reflectance standard. The Brunauer-Emmett-Teller (BET) specific surface area (S_{BET}) of the powders was analyzed by nitrogen adsorption using a Tristar II Micromeritics adsorption analyzer (USA). The XPS spectra were acquired by using an Axis Ultra (Kratos Analytical, UK) XPS spectrometer equipped with an Al Kα source (1486.6 eV). Photoluminescence (PL) spectra were measured at room temperature on a RF-5301PC spectrofluorophotometer (Shimadzu, Japan) under the excitation of 350 nm.

Theoretical calculations: The DFT calculations were carried out by using the Vienna *ab initio* simulation package (VASP).[24,25] The exchange-correlation interaction is described by generalized gradient approximation (GGA) with the Perdew-Burke-Ernzerhof (PBE) functional.[26] The van der Waals interactions were described by zero damping DFT-D_3 method of Grimme[27] in all calculations. The energy cut-off is set to 500 eV. The vacuum space in b and c axis were 15 Å, which was sufficient to avoid the interaction between periodical images. The Brillouin zone is sampled by a Monkhorst-Pack 2×3×1 K-point grid. The different charge density is obtained by

$$\Delta\rho = \rho^{Ti_3C_2O_2+Zn_{0.5}Cd_{0.5}S} - \rho^{Ti_3C_2O_2} - \rho^{Zn_{0.5}Cd_{0.5}S} \quad (1)$$

Photocatalytic hydrogen production: The photocatalytic hydrogen production experiments were carried out in a Pyrex flask at room temperature and atmospheric pressure. The openings of the flask are sealed with silicone rubber septum. A Xenon arc lamp (300 W) with a UV-cutoff filter (> 420 nm) was utilized as a light source to trigger the photocatalytic reaction. In a typical photocatalytic experiment, 20 mg of photocatalyst was suspended upon constant stirring in a mixed aqueous solution of lactic acid and water (lactic acid, 18 vol%, as a sacrificial reagent). Before irradiation, the system was purged with argon for 0.5 h to remove the air inside and to ensure that the reaction system is under anaerobic conditions. A 0.2 mL of gas was intermittently sampled through the septum, and hydrogen was analyzed by gas chromatograph (Clarus 480, PerkinElmer, USA, TCD with Ar as a carrier gas and TDX-01 column). All glassware was carefully rinsed with deionized water prior to use.

The apparent quantum efficiency (QE) was acquired under the identical photocatalytic reaction condition. Four low-power 420 nm-LED (3 W) (Shenzhen LAMPLIC Science Co. Ltd. China), which were put 1 cm away from the reactor in four different directions, were used as light sources to trigger the photocatalytic reaction. The focused intensity for each 420 nm-LED was about 6.0 mW/cm^2. The QE was calculated according to Equation (1):

$$\begin{aligned} \mathrm{QE}\,[\%] &= \frac{\text{number of reacted electrons}}{\text{number of incident photons}} \times 100 \\ &= \frac{\text{number of evolved H}_2\text{ molecules} \times 2}{\text{number of incident photons}} \times 100 \end{aligned} \tag{2}$$

Photoelectrochemical and electrochemical measurements: The working electrodes were synthesized as follows: 20 mg photocatalyst was grinded with 30 mg polyethylene glycol (PEG, molecular weight: 20000) and 0.5 mL ethanol to make a slurry. The slurry was then coated onto a 2 cm×1.5 cm F-doped SnO_2-coated glass (FTO glass) electrode by the doctor blade approach. Then the resulting electrodes were dried in an oven and calcined at 350 °C for 30 min in a N_2 gas flow. All electrodes investigated had a similar film thickness of 10~11 μm. Transient photocurrent densities were measured by an electrochemical analyzer (CHI 650D Instruments) with a standard three-electrode system using the prepared samples as the working electrodes with an active area of *ca.* 1.35 cm^2, a Pt wire as the counter electrode, and Ag/AgCl (saturated KCl) as a reference electrode. The light was generated by a Xenon arc lamp (300 W) with a

UV-cutoff filter (> 420 nm). 0.2 M Na_2S and 0.04 M Na_2SO_3 mixed aqueous solution was used as the electrolyte. EIS measurements were also performed in the above-mentioned three-electrode system and recorded over a frequency range of 1-2×10^5 Hz with an alternating current (AC) amplitude of 20 mV. The polarization curves were measured in the same three-electrode system, and the bias sweep range was from -1.5 to -0.8 V *vs.* Ag/AgCl with a step size of 5 mV. The Mott-Schottky plots were also measured in the above mentioned three-electrode system and recorded over an AC frequency of 1200 Hz. All the electrochemical measurement was conducted in 0.5 M Na_2SO_4 aqueous solution.

Supporting Information

Supporting Information is available from the Wiley Online Library or from the author.

Acknowledgements

This work is financially supported by the Australian Research Council (ARC) through the Discovery Project programs (grant numbers DP140104062 and DP130104459).

Received: ((will be filled in by the editorial staff))
Revised: ((will be filled in by the editorial staff))
Published online: ((will be filled in by the editorial staff))

[1] J. Ran, J. Zhang, J. Yu, M. Jaroniec, S. Z. Qiao, *Chem. Soc. Rev.* **2014**, *43*, 7787.

[2] X. Chen, S. Shen, L. Guo, S. S. Mao, *Chem. Rev.* **2010**, *110*, 6503.

[3] A. Fujishima, K. Honda, *Nature* **1972**, *238*, 37.

[4] A. Kudo, Y. Misekia, *Chem. Soc. Rev.* **2009**, *38*, 253.

[5] J. Ran, J. Zhang, J. Yu, S. Z. Qiao, *ChemSusChem* **2014**, *7*, 3426.

[6] J. Xiao, Q. Shang, Y. Xiong, Q. Zhang, Y. Luo, S. Yu, H. Jiang, *Angew. Chem. Int. Ed.* **2016**, *55*, 9389.

[7] X. Li, W Bi, L. Zhang, S. Tao , W. Chu, Q. Zhang, Y. Luo, C. Wu, Y. Xie, *Adv. Mater.* **2016**, *28*, 2427.

[8] H. He, J. Lin, W. Fu, X. Wang, H. Wang, Q. Zeng, Q. Gu, Y. Li, C. Yan, B. K. Tay, C. Xue, X. Hu, S. T. Pantelides, W. Zhou, Z. Liu, *Adv. Energy Mater.* **2016**, *6*, 1600464.

[9] M. Naguib, J. Halim, J. Lu, K. M. Cook, L. Hultman, Y. Gogotsi, M. W. Barsoum, *J. Am. Chem. Soc.* **2013**, *135*, 15966.

[10] M. Naguib, V. N. Mochalin, M. W. Barsoum, Y. Gogotsi, *Adv. Mater.* **2014**, *26*, 992.

[11] M. Ghidiu, M. R. Lukatskaya, M. Zhao, Y. Gogotsi, M. W. Barsoum, *Nature* 2014, *516*, 78.

[12] J. Yu, J. Ran, *Energy Environ. Sci.* **2011**, *4*, 1364.

[13] J. Ran, J. Yu, M. Jaroniec, *Green Chem.* **2011**, *13*, 2708.

[14] T. Y. Ma, J. L. Cao, M. Jaroniec, S. Z. Qiao, *Angew. Chem. Int. Ed.* **2016**, *55*, 1138.

[15] Y. Ide, N. Inami, H. Hattori, K. Saito, M. Sohmiya, N. Tsunoji, K. Komaguchi, T. Sano, Y. Bando, D. Golberg, Y. Sugahara, *Angew. Chem. Int. Ed.* **2016**, *55*, 3600.

[16] Q. Han, B. Wang, J. Gao, L. Qu, *Angew. Chem. Int. Ed.* **2016**, *55*, 10849.

[17] X.-L. Zheng, J.-P. Song, T. Lin, Z. P. Hu, P.-F. Yin, K. Davey, X.-W. Du, S.-Z. Qiao, *Adv. Mater.* **2016**, *28*, 4935.

[18] H. Zhou, Y. Qu, T. Zeida, X. Duan, *Energy Environ. Sci.* **2012**, *5*, 6732.

[19] J. Hong, X. Xia, Y. Wang, R. Xu, *J. Mater. Chem.* **2012**, *22*, 15006.

[20] W. Zhou, W. Li, J.-Q. Wang, Y. Qu, Y. Yang, Y. Xie, K. Zhang, L. Wang, H. Fu, D. Zhao, *J. Am. Chem. Soc.* **2014**, *136*, 9280.

[21] Q. Peng, J. Guo, Q. Zhang, J. Xiang, B. Liu, A. Zhou, R. Liu, Y. Tian, *J. Am. Chem. Soc.* **2014**, *136*, 4113.

[22] W. Zhang, Y. Wang, Z. Wang, Z. Zhong, R. Xu, *Chem. Commun.* **2010**, *46*, 7631.

[23] Q. Xiang, J. Yu, M. Jaroniec, *J. Am. Chem. Soc.* **2012**, *134*, 6575.

[24] G. Kresse and J. Furthmüller, *Phys. Rev. B* **1996**, *54*, 11169.

[25] G. Kresse and J. Furthmüller, *Comp. Mater. Sci.* **1996**, *6,* 15.

[26] J. Perdew, K. Burke, M. Ernzerhof, *Phys. Rev. Lett.* **1996**, *77*, 3865.

[27] S. Grimme, J. Antony, S. Ehrlich, H. Krieg, *J. Chem. Phys.* **2010**, *132*, 154104.

The loading of a novel Ti_3C_2 MXene co-catalyst onto $Zn_{0.5}Cd_{0.5}S$ leads to the great enhancement of its visible-light photocatalytic H_2-production activity. Such a high activity arises from the outstanding electron extracting ability of Ti_3C_2 MXene, as revealed by both experimental and density function theory (DFT) calculation results.

photocatalytic water splitting, co-catalyst, Ti_3C_2 MXene, $Zn_{0.5}Cd_{0.5}S$

J. Ran, S. Z. Qiao*

Superior electron-extracting capacity of Ti_3C_2 MXene on $Zn_{0.5}Cd_{0.5}S$ towards highly-efficient visible-light photocatalytic H_2 production

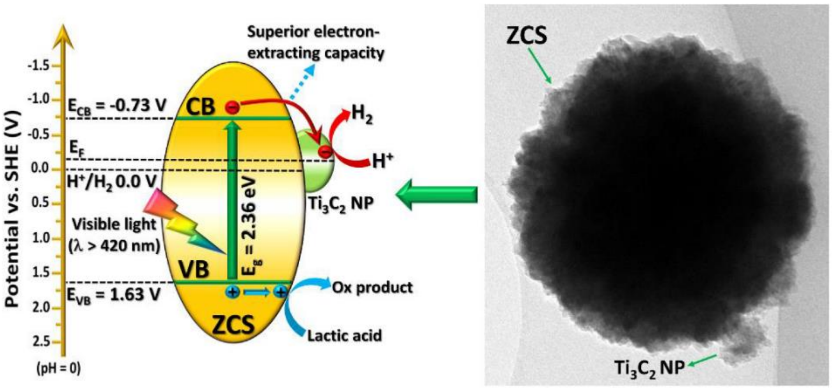

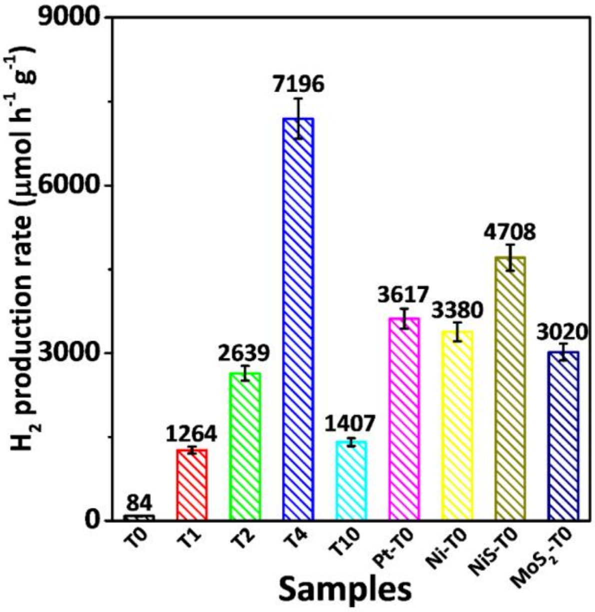

Figure 1. A comparison of the photocatalytic activities of T0, T1, T2, T4, T10, Pt-T0, Ni-T0, NiS-T0 and MoS_2-T0 for photocatalytic H_2 production from 18 vol.% lactic acid aqueous solution under visible-light illumination (λ ≥ 420 nm, 300 W Xe lamp).

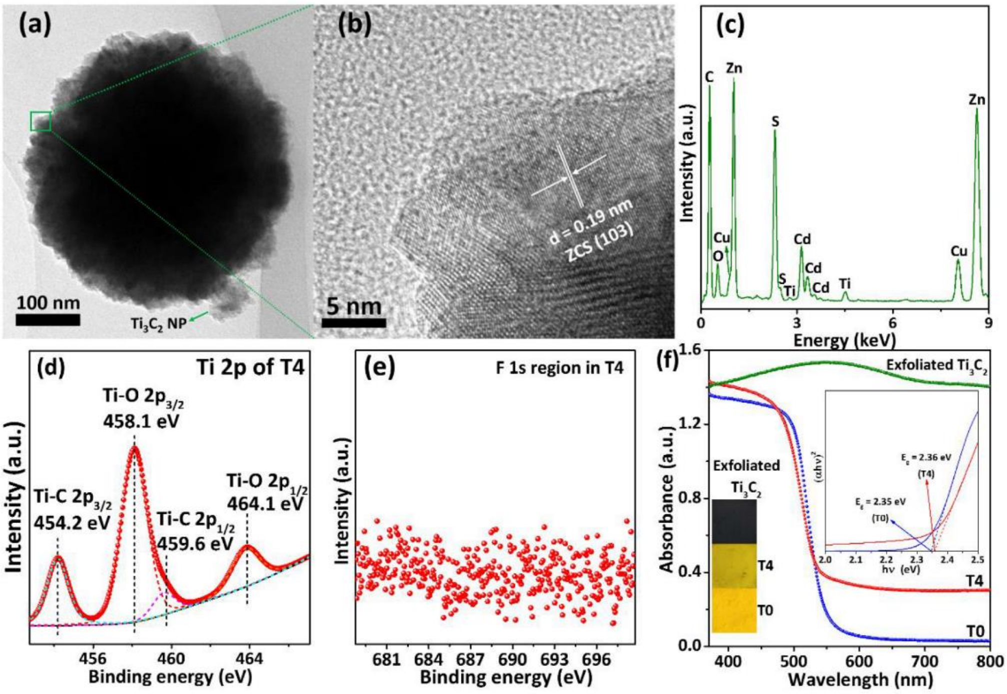

Figure 2. (a) TEM image, (b) high-resolution TEM image and (c) EDX spectrum of T4; high-resolution XPS spectra of (d) Ti 2p and (e) F 1s for T4; (f) UV-Vis diffuse reflectance spectra of T0, T4 and exfoliated Ti_3C_2. Figure 2f inset shows the colors of T0, T4 and exfoliated Ti_3C_2, and Tauc plots of T0 and T4.

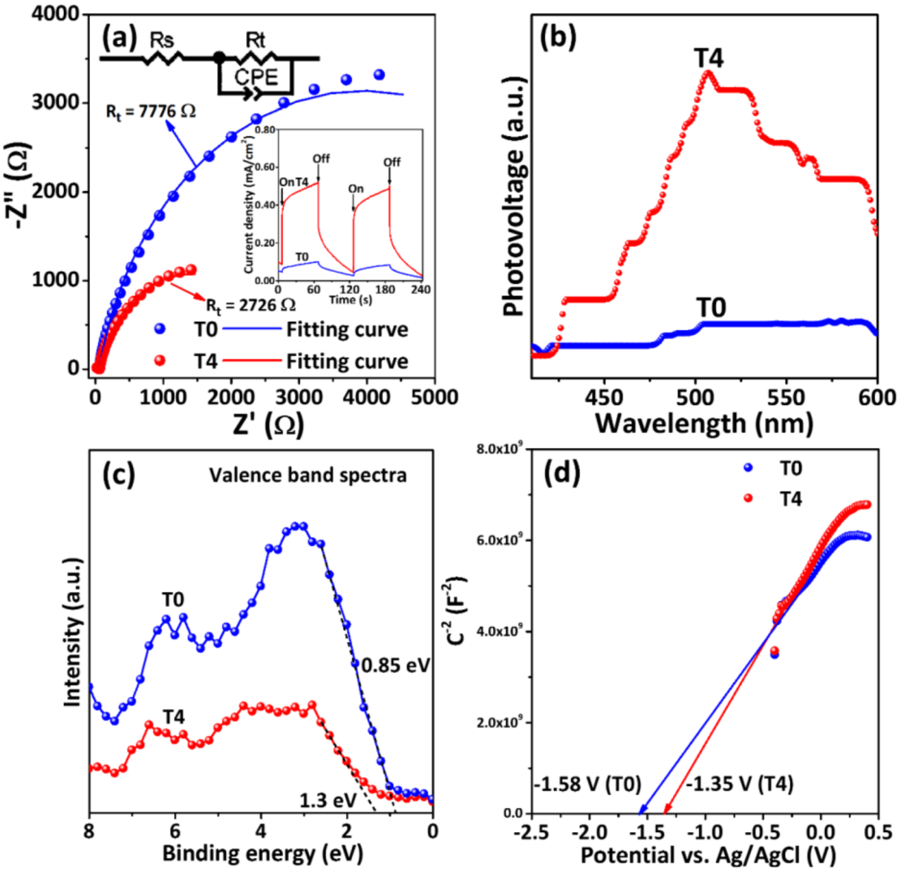

Figure 3. (a) EIS Nyquist plots of T0 and T4 electrodes measured under the open-circle potential and visible-light irradiation in 0.5 M KPi buffer solution (pH = 7). Figure 3a inset shows the transient photocurrent responses of T0 and T4 electrodes in 0.2 M Na_2S + 0.04 M Na_2SO_3 mixed aqueous solution under visible-light irradiation; (b) surface photovoltage (SPV) spectra of T0 and T4; (c) valence band XPS spectra of T0 and T4; (d) Mott-Schottky plots of T0 and T4 electrodes in 0.5 M Na_2SO_4 aqueous solution.

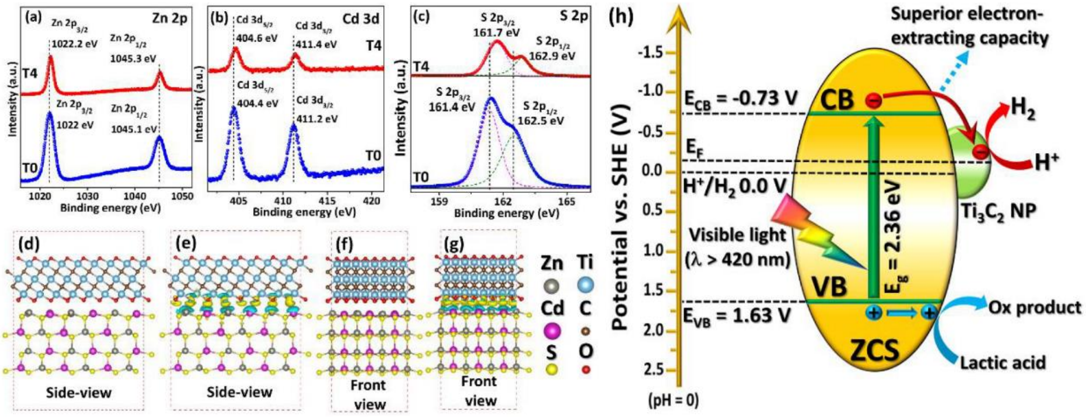

Figure 4. The high-resolution XPS spectra of (a) Zn 2p, (b) Cd 3d and (c) S 2p for T0 and T4; (d) side-view atomic model of hexagonal $Zn_{0.5}Cd_{0.5}S$ and $Ti_3C_2O_2$ monolayer; (e) side-view differential charge density map of hexagonal $Zn_{0.5}Cd_{0.5}S$ and $Ti_3C_2O_2$ monolayer; (f) front-view atomic model of hexagonal $Zn_{0.5}Cd_{0.5}S$ and $Ti_3C_2O_2$ monolayer; (g) Front-view differential charge density map of hexagonal $Zn_{0.5}Cd_{0.5}S$ and $Ti_3C_2O_2$ monolayer. Yellow and green isosurfaces in Figure 4e and g depict regions of net electron accumulation and deficit upon combination, respectively; (h) Schematic illustration for the charge transfer and separation in the ZCS/Ti_3C_2 system under visible-light irradiation.

Copyright WILEY-VCH Verlag GmbH & Co. KGaA, 69469 Weinheim, Germany, 2016.

Supporting Information

Superior electron-extracting capacity of Ti_3C_2 NPs on $Zn_{0.5}Cd_{0.5}S$ towards enhanced visible-light photocatalytic H_2 production

*Jingrun Ran and Shi Zhang Qiao**

J. Ran, Prof. S. Z. Qiao
School of Chemical Engineering
The University of Adelaide, Adelaide, SA 5005, Australia
E-mail: s.qiao@adelaide.edu.au

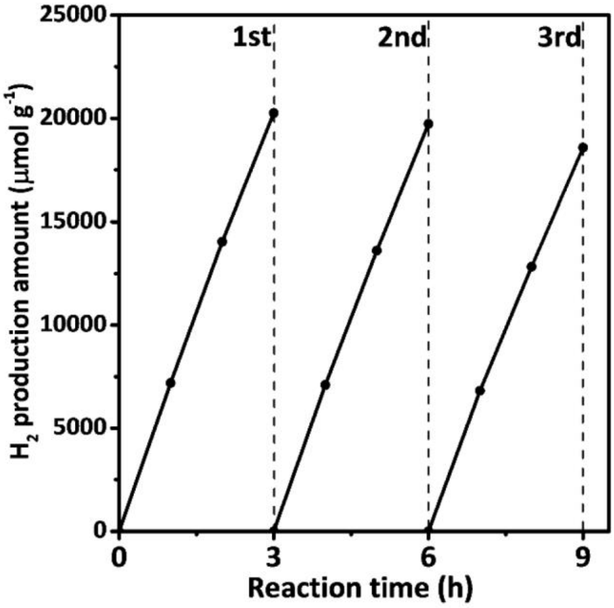

Figure S1. Time course of photocatalytic H_2 production over sample T4. The reaction system was purged with Ar every three hours for 30 min to remove the H_2 inside.

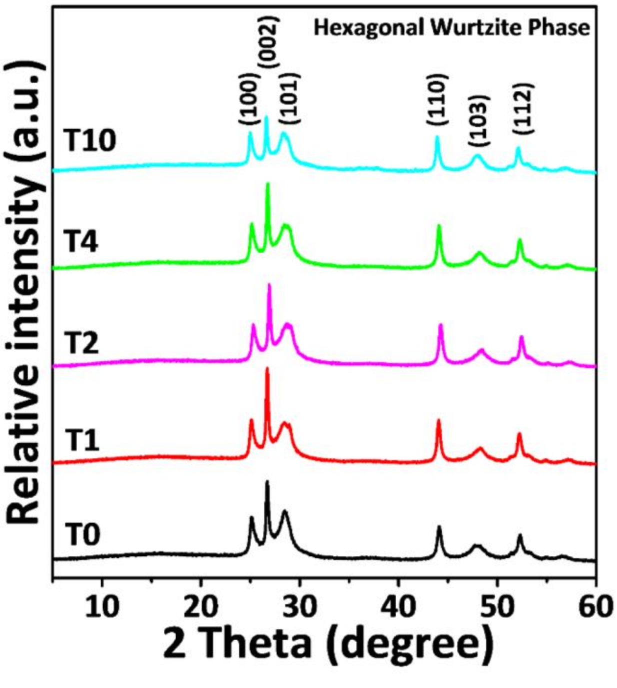

Figure S2. XRD patterns of T0, T1, T2, T4 and T10.

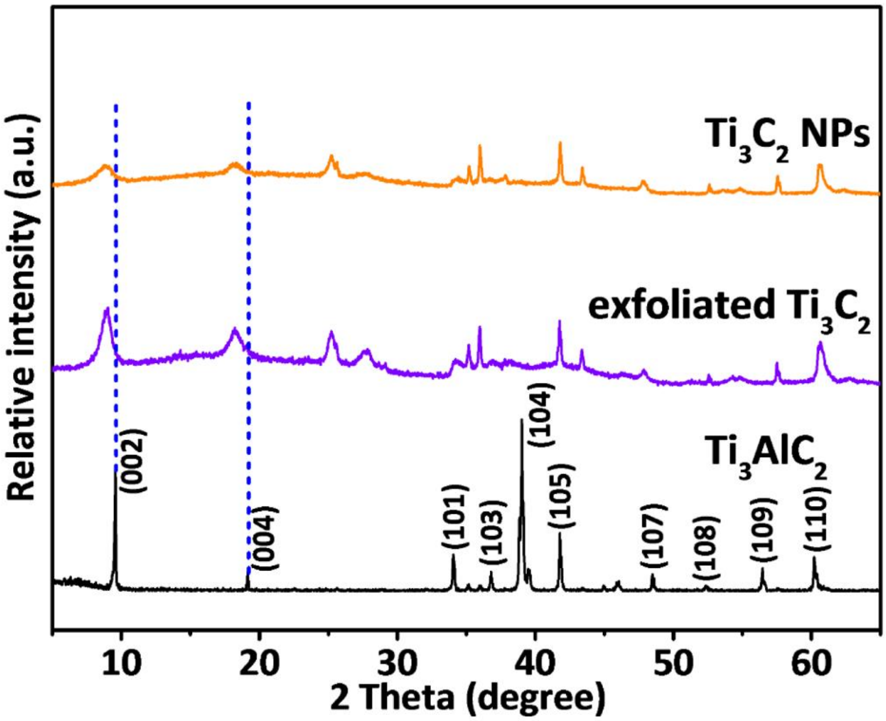

Figure S3. XRD patterns of Ti_3AlC_2, exfoliated Ti_3C_2 and Ti_3C_2 NPs.

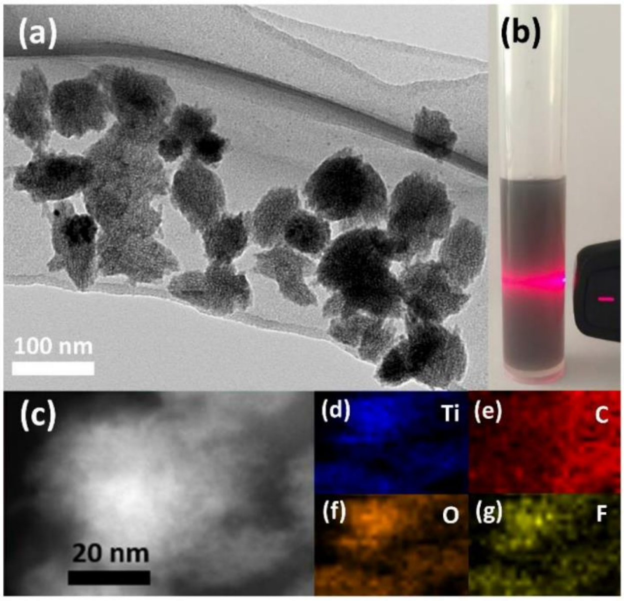

Figure S4. (a) TEM image of Ti_3C_2 NPs; (b) the Tyndall effect of Ti_3C_2 dispersion; (c) HAADF image of Ti_3C_2 NPs and its corresponding EDX elemental mapping images of (d) Ti, (e) C, (f) O and (g) F.

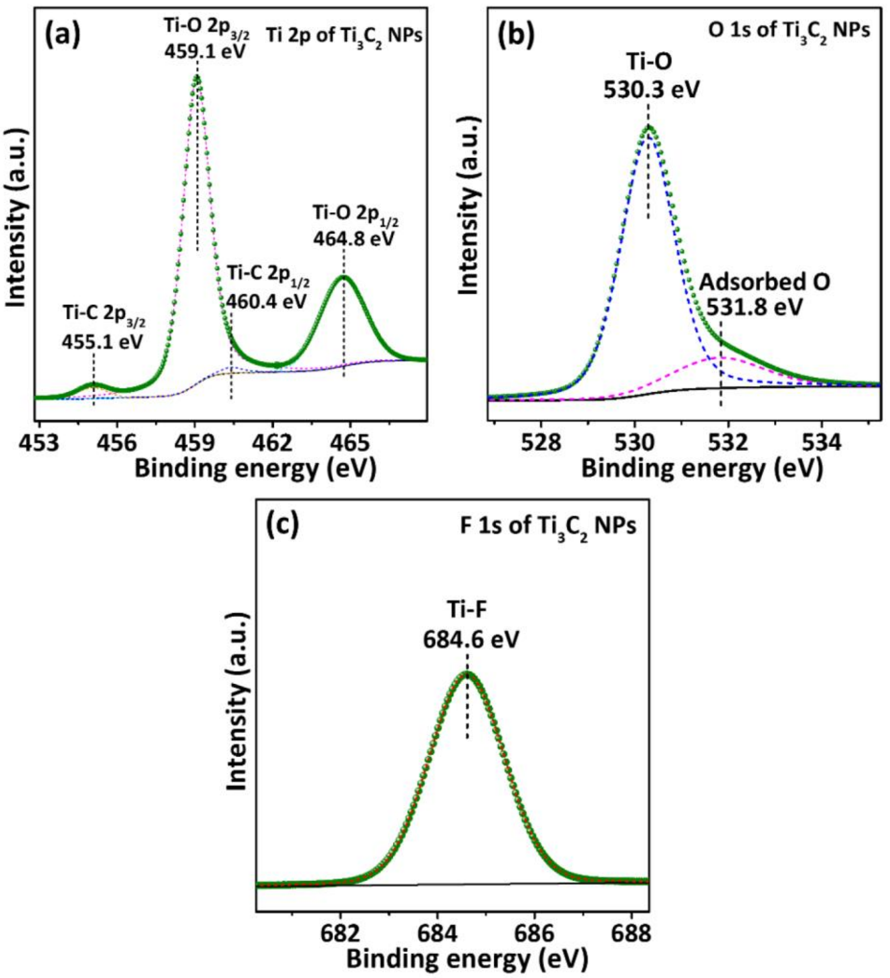

Figure S5. High-resolution XPS spectra of (a) Ti 2p, (b) O 1s and (c) F 1s for Ti_3C_2 NPs.

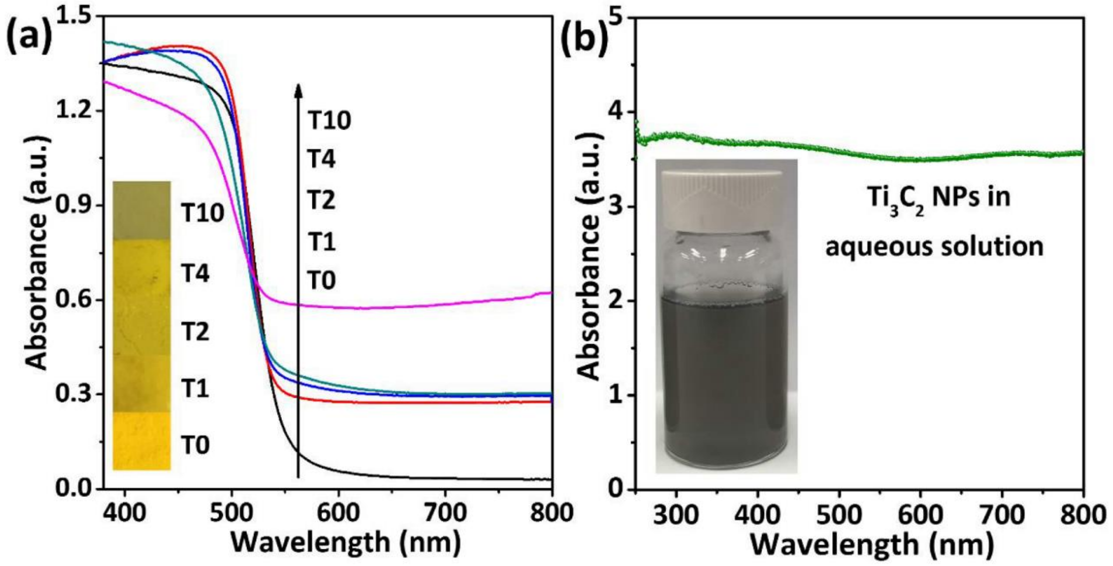

Figure S6. (a) UV-Vis diffuse reflectance spectra of T0, T1, T2, T4 and T10. The inset shows the colors of all the samples; (b) UV-Vis absorbance spectrum and picture of the Ti_3C_2 NPs in aqueous solution.

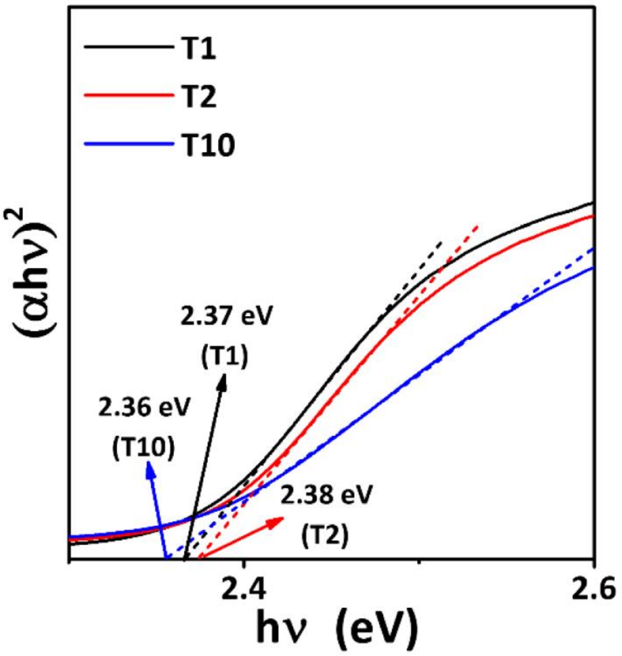

Figure S7. Tauc plots of T1, T2 and T10.

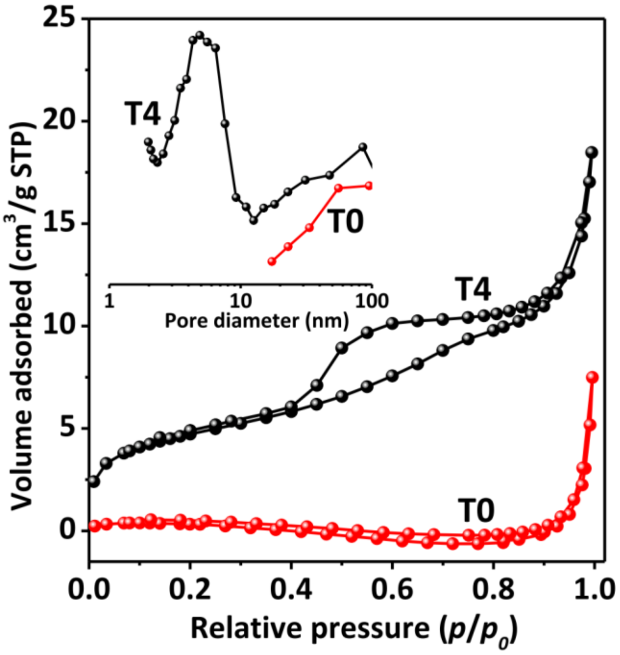

Figure S8. (a) N_2 sorption isotherms and (b) the corresponding pore-size distribution curves (inset) of T0 and T4.

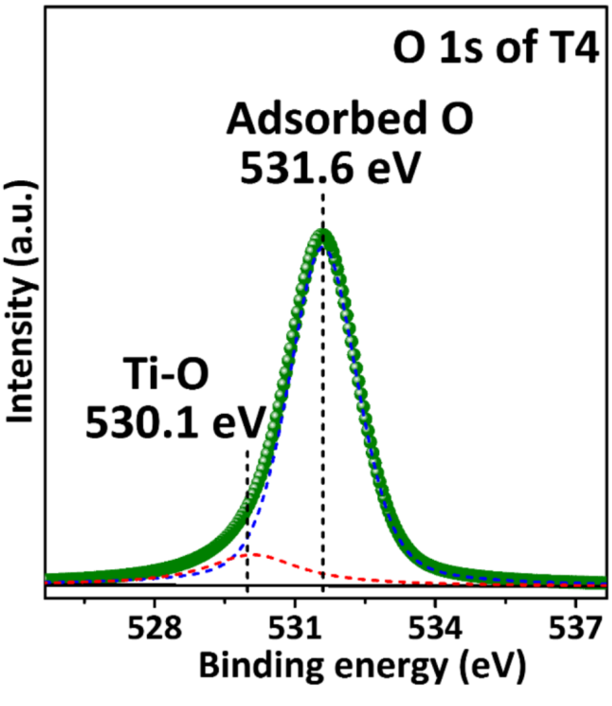

Figure S9. High-resolution XPS spectra of O 1s for T4.

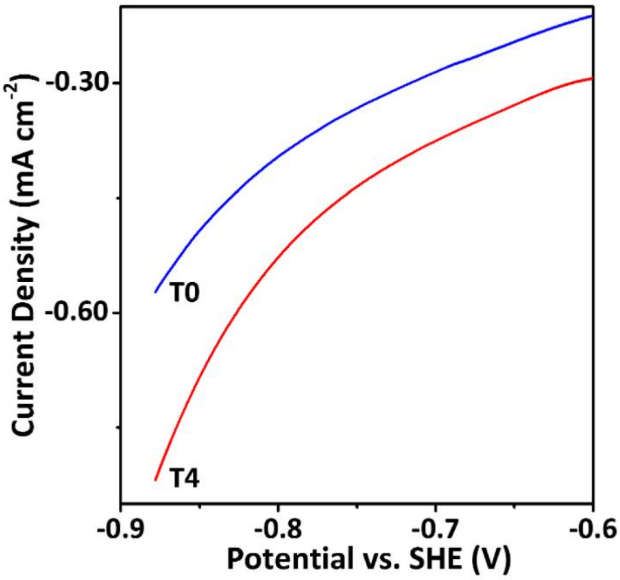

Figure S10. Polarization curves of T0 and T4 electrodes in 0.5 M Na_2SO_4 aqueous solution.

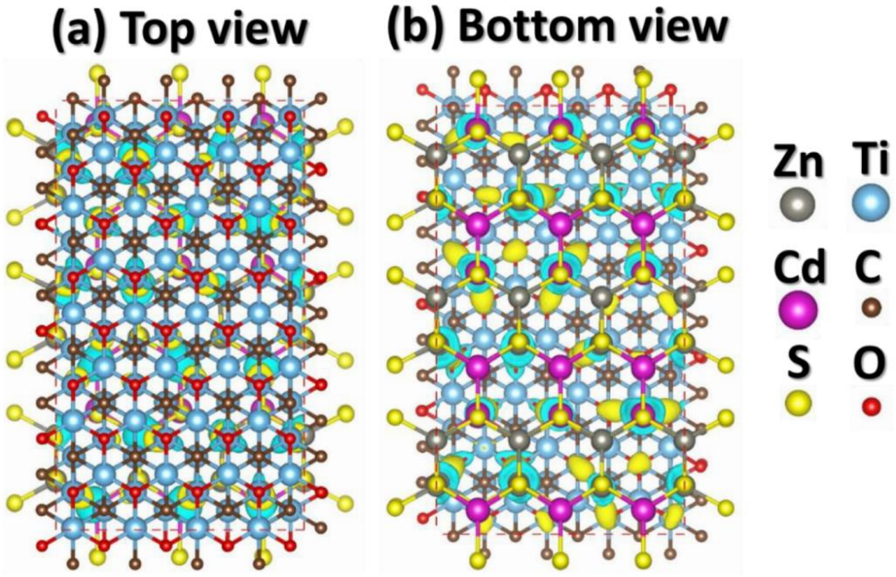

Figure S11. (a) Top-view and (b) bottom-view of differential charge density map for hexagonal $Zn_{0.5}Cd_{0.5}S$ and $Ti_3C_2O_2$ monolayer.

Table S1. The corresponding physicochemical properties of T0, T1, T2, T4 and T10.

Samples	Ti_3C_2 (wt.%) (ICP-AES)	S_{BET} ($m^2\ g^{-1}$)	PV [a] ($cm^3\ g^{-1}$)	APS [b] (nm)	Eg [c] (eV)	Activity ($\mu mol\ h^{-1}\ g^{-1}$)
T0	0	1.0	0.003	14.0	2.34	84
T1	0.239	6.1	0.013	8.4	2.37	1264
T2	0.532	5.7	0.015	10.7	2.38	2639
T4	1.065	17.0	0.022	5.2	2.35	7196
T10	1.68	18.7	0.026	5.6	2.36	1407

[a] PV: Pore volume, [b] APS: Average pore size, [c] Eg: Band gap.

Chapter 7: Conclusion and Perspectives

7.1 Conclusions

This thesis is devoted to develop inexpensive, efficient and robust photocatalysts/co-catalysts and gain insights into the mechanism and kinetics of photocatalytic H_2 production. Based on the research in this thesis, the following conclusions can be drawn:

(1) The photocatalytic H_2-production activity of metal-free g-C_3N_4 can be tremendously enhanced via a brand-new strategy combining P doping and thermal exfoliation. P doping not only extends the light-responsive region by creating mid-gap states (-0.16 V *vs.* NHE) in the band gap of g-C_3N_4, but also greatly increase the charge density in the P-doped conjugated system to enhance charge mobility. Meanwhile, thermal exfoliation not only obviously shorten the charge transfer distance from bulk to surface, but also dramatically improve the surface area of g-C_3N_4 for the adsorption/desorption of protons/triethanolamine and the subsequent photocatalytic reactions. Hence, through simultaneously tuning and optimizing the electronic, crystallographic, surface and textural structures, the photocatalytic activity of g-C_3N_4 is synergistically improved.

(2) The photocatalytic H_2-production performance of the $Zn_{0.8}Cd_{0.2}S$ (ZCS) system was optimized for the first time by choosing a suitable Ni-based co-catalyst from various Ni species, *i.e.* NiS, Ni, and $Ni(OH)_2$. The results show that NiS-ZCS and Ni-ZCS exhibit substantially enhanced photocatalytic activity over ZCS because NiS/Ni could facilitate the charge separation and transfer at the interface of heterojunctions constructed between NiS/Ni and ZCS, and promote the hydrogen evolution reaction on the ZCS surface. Surprisingly, compared with NiS-ZCS and Ni-ZCS, $Ni(OH)_2$-ZCS exhibits a much higher photocatalytic H_2-production rate of 7160 $\mu molh^{-1}g^{-1}$ with a quantum efficiency of 29.5% at 420 nm, which exceeds that of ZCS by a factor of 25.5. Such a great enhancement of activity is induced by the synergetic effect between $Ni(OH)_2$ and Ni formed in situ during the photocatalytic reaction. This work shows for the first time that $Ni(OH)_2$ is the most suitable Ni-based co-catalyst applied to the ZCS system to achieve the highest photocatalytic activity because of its unique synergetic effect and provides a deep insight into the relationship between the intrinsic properties of a co-catalyst (*e.g.*, electronic structure and catalytic function) and the photocatalytic performance of its applied photocatalyst system.

(3) Our work demonstrates the great advantage of using a novel MXene material, Ti_3C_2 NPs, as a highly-active co-catalyst. On the basis of theoretical predictions, we rationally employed the hydrothermal treatment to replace the -F terminations on Ti_3C_2 by -O/-OH terminations, and coupled the pretreated Ti_3C_2 with CdS to prepare a highly-fused CdS/Ti_3C_2 composite

photocatalyst. Remarkably, this composite photocatalyst exhibited both super high visible-light photocatalytic activity (14342 μmolh^{-1}g^{-1}) 10 and apparent quantum efficiency (40.1% at 420 nm), render it as one of the best metal-sulfides photocatalysts without the addition of noble metals. We found that this unusual activity can be attributed to the synergetic effect of the highly-efficient charge separation and migration from CdS to Ti_3C_2 NPs and the rapid hydrogen evolution on numerous -O terminations present on Ti_3C_2 NPs. Successful application of Ti_3C_2 NPs as an efficient co-catalyst on ZnS or $Zn_xCd_{1-x}S$ excitingly confirms the versatile nature of this newly-developed co-catalyst. Our work not only demonstrates the power of combining DFT calculations and experimental techniques to effectively engineer novel MXene family materials at the atomic level towards desired photocatalytic reactions, but also opens a new area of utilizing this new generation of co-catalytic materials to achieve highly efficient, steady and cost-effective solar water splitting based on semiconductor photocatalysts/photoelectrodes.

(4) Our work for the first time reported the fabrication of a Ti_3C_2 modified $Zn_{0.5}Cd_{0.5}S$ composite photocatalyst by a facile hydrothermal approach. The as-synthesized Ti_3C_2 modified $Zn_{0.5}Cd_{0.5}S$ composite exhibits the highest photocatalytic H_2-production activity of 7196 μmol h^{-1} g^{-1} at the optimal loading (4 wt%) of Ti_3C_2. The enhanced photocatalytic H_2-production activity is mainly attributed to the excellent electron-accepting ability of Ti_3C_2 NPs loaded on $Zn_{0.5}Cd_{0.5}S$. The stability of Ti_3C_2 NPs loaded $Zn_{0.5}Cd_{0.5}S$ has been confirmed by conducting the photocatalytic test for 9 hours. Our work not only demonstrates the possibility of using Ti_3C_2 to replace expensive noble-metal co-catalysts in solar H_2 production, but also provide a new insight into the interfacial charge transfer in the Ti_3C_2 modified photocatalyst systems.

7.2 Perspectives

Although significant progress for photocatalytic H_2 production has been achieved in this thesis, there are some challenges in this future research:

(1) Although significant progress has been achieved in metal-free g-C_3N_4 based photocatalysts, their efficiency and stability are far from satisfactory for commercial application. Therefore, the further enhancement of their performance should rely on investigation, design and fabrication of g-C_3N_4 based photocatalysts at the atomic level through utilizing the advanced characterization techniques, such as X-ray absorption spectroscopy and aberration-corrected transmission electron microscopy. Besides, single-atom co-catalyst, *e.g.* Pt and Ni, can be loaded on the surface of g-C_3N_4 nanosheet to further improve its photocatalytic H_2-production activity.

(2) Moreover, despite that many high-efficiency and low-cost co-catalysts based on earth-abundant transitional metals, *e.g.* Ni and Ti, have been synthesized and proven to be more effective than noble-metal Pt, the development of metal-free co-catalysts with comparable activity to Pt is still at infancy. Hence, some new two-dimensional (2D) metal-free materials, *e.g.* phosphorene, silicene and germanene, can be tried as metal-free co-catalysts, due to their good conductivity and large surface area.

(3) Furthermore, the investigation of the controllable loading of co-catalyst at the desired position, *e.g.* specific crystal facets and edge of nanosheets, on the nano-structured photocatalysts is still missing. Hence, more efforts should be put into this area to maximize the effect of loading co-catalyst on the photocatalytic performance.

(4) Lastly, the reaction mechanisms are still inconclusive in many photocatalytic systems due to the continuous developments of novel photocatalysts/co-catalysts. Therefore, more investigation combining theoretical and experimental explorations is essential to overcome this fundamental and significant problem. Moreover, *in-situ* techniques can be applied to provide insightful investigation on the photocatalytic mechanism, and then guide the design and synthesis of high-performance photocatalysts.

Appendix: Publications during Ph.D study

Refereed journal articles:

[1] **Jingrun Ran**, Tian Yi Ma, Guoping Gao, Xi-Wen Du and Shi Zhang Qiao, Porous P-doped Graphitic Carbon Nitride Nanosheets for Synergistically Enhanced Visible-Light Photocatalytic H_2 Production, ***Energy and Environmental Science***, 2015, 8, 3708-3717.
[IF = 25.427; cites 38]

[2] **Jingrun Ran**, Jun Zhang, Jiaguo Yu and Shi Zhang Qiao, Enhanced Visible-Light Photocatalytic H_2 Production by $Zn_xCd_{1-x}S$ Modified with Earth-Abundant Nickel-Based Cocatalysts, ***ChemSusChem***, 2014, 7, 3426-3434.
[IF = 7.116; cites 37]

[3] **Jingrun Ran**, Jun Zhang, Jiaguo Yu, Mietek Jaroniec and Shi Zhang Qiao, Earth-Abundant Cocatalysts for Semiconductor-Based Photocatalytic Water Splitting, ***Chemical Society Reviews***, 2014, 43, 7787-7812.
[IF = 34.09; cites 359]

[4] **Jingrun Ran**, Guoping Gao, Fa-Tang Li, Tian-Yi Ma, Aijun Du and Shi-Zhang Qiao, Ti_3C_2 MXene Co-catalyst on Metal Sulfide Photo-Absorbers for Enhanced Visible-Light Photocatalytic Hydrogen Production, ***Nature Communications***, accepted on 11 November 2016.
[IF = 11.329]

[5] **Jingrun Ran** and Shi-Zhang Qiao, Superior Electron-Extracting Capacity of Ti_3C_2 MXene on $Zn_{0.5}Cd_{0.5}S$ towards Enhanced Visible-Light Photocatalytic H_2 Production, ***Small***, in preparation.

[6] Tian Yi Ma, **Jingrun Ran**, Sheng Dai, Mietek Jaroniec and Shi Zhang Qiao, Phosphorus-Doped Graphitic Carbon Nitrides in Situ Grown on Carbon Fiber Paper: Flexible and Reversible Oxygen Electrodes, ***Angewandte Chemie-International Edition***, 2015, 54, 4646-4650.
[IF = 11.709; cites 138]

[7] Fa-Tang Li, **Jingrun Ran**, Mietek Jaroniec and Shi Zhang Qiao, Solution Combustion Synthesis of Metal Oxide Nanomaterials for Energy Storage and Conversion, ***Nanoscale***, 2015, 7, 17590-17610.
[IF = 7.76; cites 21]

[8] Mohammad Ziaur Rahman, **Jingrun Ran**, Youhong Tang, Mietek Jaroniec and Shi Zhang Qiao, Surface Activated Carbon Nitride Nanosheets with Optimized Electro- Optical Properties for Highly Efficient Photocatalytic Hydrogen Production, ***Journal of Materials Chemistry A***, 2016, 4, 2445-2452.

[IF = 8.262; cites 5]

[9] Pan-Yong Kuang, **Jingrun Ran**, Zhao-Qing Liu, Hong-Juan Wang, Nan Li, Yu-Zhi Su, Yong-Gang Jin and Shi-Zhang Qiao, Enhanced Photoelectrocatalytic Activity of BiOI Nanoplate-Zinc Oxide Nanorod p-n Heterojunction, ***Chemistry-A European Journal***, 2015, 21, 15360-15368.

[IF = 5.771; cites 10]

[10] Sheng Chen, Jingjing Duan, **Jingrun Ran**, Mietek Jaroniec and Shi Zhang Qiao, N-doped Graphene Film-Confined Nickel Nanoparticles as a Highly Efficient Three-Dimensional Oxygen Evolution Electrocatalyst, ***Energy and Environmental Science***, 2013, 6, 3693-3699.

[IF = 25.427; cites 108]

[11] Jun Zhang, Lifang Qi, **Jingrun Ran**, Jiaguo Yu and Shi Zhang Qiao, Ternary NiS/$Zn_xCd_{1-x}S$/Reduced Graphene Oxide Nanocomposites for Enhanced Solar Photocatalytic H_2-Production Activity, ***Advanced Energy Materials***, 2014, 4, 1301925.

[IF = 15.23; cites 68]

[12] Sheng Chen, Jingjing Duan, **Jingrun Ran** and Shi-Zhang Qiao, Paper-Based N-Doped Carbon Films for Enhanced Oxygen Evolution Electrocatalysis, ***Advanced Science***, 2015, 2, 1400015.

[IF = 6.000 cites 11]

[13] Fa-tang Li, Qing Wang, **Jingrun Ran**, Ying-juan Hao, Xiao-jing Wang, Dishun Zhao and Shi Zhang Qiao, Ionic Liquid Self-Combustion Synthesis of $BiOBr/Bi_{24}O_{31}Br_{10}$ Heterojunctions with Exceptional Visible-light Photocatalytic Performances, ***Nanoscale***, 2015, 7, 1116-1126.

[IF = 7.76; cites 30]

Conference Papers:

[14] **Jingrun Ran** and Shi Zhang Qiao, Porous P-doped g-C_3N_4 nanosheets for high performance visible-light photocatalytic H_2 production, Poster Presentation, Nanotechnology Entrepreneurship Workshop for Early Career Researchers, Gold Coast, 10-11 June, 2015.

[15] **Jingrun Ran** and Shi Zhang Qiao, Enhanced Photocatalytic H_2-Production Activity of CdS Nanorod/Reduced Graphene Oxide Nanoseet Composite, Poster Presentation, CHEMECA, Perth, October, 2014.

[16] **Jingrun Ran**, Jun Zhang, Jiaguo Yu and Shi Zhang Qiao, Enhanced Visible-Light Photocatalytic H_2 Production by $Zn_xCd_{1-x}S$ Modified with Earth-Abundant Nickel-Based Cocatalysts, Australian Nanotechnology Network Early Career Researchers Meeting, Poster Presentation, Sydney, 10-11 July, 2014.